ISTITUTO ITALIANO DI TECNOLOGIA
SMART MATERIALS

UNIVERSITÀ DEGLI STUDI
DI GENOVA

Improving tribomechanical properties of polymeric nanocomposite coatings

by

Muhammad Tamoor Masood

MSc, Chalmers University of Technology (2010)

Submitted to the Department of Nanophysics

in fulfilment of the requirement for the degree of

Doctor of Philosophy

at the

ISTITUTO ITALIANO DI TECNOLOGIA

February, 2018

Signature redacted

Author…………………………………………………………………Department of
Nanophysics IIT, DIBRIS UNIGE

Signature redacted

Certified by……………………………………………..………………Athanassia Athanassiou

Tenured Senior Researcher

Coordinator of Smart Materials Group

Thesis Supervisor

Improving tribomechanical properties of polymeric nanocomposite coatings

by

Muhammad Tamoor Masood

Submitted to the Department of Nanophysics

in fulfilment of the requirement for the degree of

Doctor of Philosophy

Abstract

Low friction, high wear resistance and strong adhesion in polymeric coatings—employed in a variety of industrial and domestic processes such as in ball bearings, water repellent surfaces, antiadhesive coatings, and anticorrosion systems—are of significant interest for energy saving and durability purposes. Even small increases in friction can have implications on energy efficiency, life time expectancy and performance of such coatings. Nanofillers and surface chemical treatments are two routes known to enhance the tribological performance of solid lubricants. This thesis presents the development and characterization of polymeric coatings with improved tribological and mechanical characteristics, with insight details and experiments from macro to nano scale. First, a mechanism is developed to enhance the wear resistance of superhydrophobic surfaces by an annealing process and by introducing a primer layer; following the tribology of these surfaces is explained. Next, the importance of rubber domains in a polymer matrix for dissipating mechanical energy of the system is explained. Then, the tribology of engineered plastics is improved by adding 2D and 3D fillers and a mechanism of transfer film on counterparts is proposed and proved. In continuity to the framework presented, the role of 2D fillers in enhancing the adhesive properties of composite coatings with different substrates is explained. From there, a novel route is adopted where surface modifications of water-based perfluorinated acrylic copolymer is achieved by changing its pH content. The enhancement in tribology of such short-chain polymers is explained and their adhesive/antiadhesive properties are studied. At the end, a study is conducted on fabrication of ultra-transparent cyanoacrylate films by controlling the polymerization process and their adhesion mechanism is explained after introducing the plasticizer effect. Finally, novel applications for fog harvesting and improvement of tribology on steel are discussed.

Thesis Supervisor: Athanassia Athanassiou

Title: Tenured Senior Researcher, Coordinator of Smart Materials Group

Acknowledgments

I would like to acknowledge my advisor, Dr. Athanassia Athanassiou, whom I am exceptionally fortunate to have had the opportunity to work under. She provided an extremely supportive and collaborative environment to work in while taking care of my freedom to pursue my own research interests. I would also like to acknowledge Dr. Ilker Bayer, who motivated and encouraged me throughout my PhD journey along with helpful feedback at many points.

I would like to pay my gratitude to Dr. Luca Ceseracciu who guided me at every step and has been always supportive and kind, much of my investigation into tribology would not have been possible without him. In addition, many of my laboratory colleagues have been incredibly helpful over the years. In particular, I would like to acknowledge Dr. Jose Heredia-Guerrero, Dr. Paraskevi Papadopoulou, Lara Marini, Giorgio Mancini, Dr. Alexander Devis, and Dr. Gabriele Nanni who have contributed to my research endeavors. I also had fortune to have colleague friends Muhammad Zahid, Umair Gulzar, Guilherme Almeida, Lin Chen, Jawad Shamsi, Nikhil, Duc Anh, Layla and Amira el Merhie for supporting me and accompanying.

I am immensely grateful for my friends and family who have been continuously provided me support, encouraged me to pursue my goals and motivated me in bad times. Most of all, they have kept me modest and grounded.

Finally, I would like to gratitude my Mom and Dad, my sister Binish, my brothers Sikandar and Fahad, and my fiancé Daniya; who prayed for me and supported me at every stage of life.

CONTENTS

LIST OF FIGURES

LIST OF TABLES

1. Introduction

Evolution of materials started from around 5,000 years ago when humans turned copper and tin ore into metallic bronze. Next progression was observed after two thousand years when iron oxide was turned into iron and steel. One of the major development of synthesizing new materials started in 1907 when Leo H. Baekeland invented the first synthetic plastic, Bakelite[1]. Since then there has been a substantial advancement in the development of synthetic polymers. Synthetic polymers, large molecules composed of repeated subunits, are synthesized in many forms, including plastics, rubbers, fibres, oil, paints, to name a few and have vital significance in almost every field of life: from biomedical, food and water applications to energy harvesting and transportation. Synthetic polymers are classified into two major types, namely thermoplastics and thermoset. Thermoplastics are highly recyclable, capable of remolding, chemically resistant and require environment friendly manufacturing, whereas thermosets are more resistant to high temperatures but present issues such as poor surface finish, non-recyclability and are unable to reshape[2].

Further, thermoplastic polymers are classified into two main classes namely amorphous and crystalline and are characterized by their characteristic transition temperature. Over 70% of the total production of thermoplastic polymers are accounted for by the large volume, low cost commodity resins such as polyethylene (PE), polypropylene (PP), polystyrene (PS), etc. Next in performing and cost efficient thermoplastics are acrylics, high impact polystyrene (HIPS), acrylonitrile-butadiene-styrene (ABS). Engineering plastics such as polyamides, polycarbonates, polyesters are manufactured for high performance applications and are preferred for their distinct mechanical properties. Specialty polymers are designed to operate under high temperature environment, some of the examples are polyimides, fluoropolymers, liquid-crystal polymers and polysulfones[3]. Each branched polymer has distinguished thermomechanical characteristics. Depending on their unique structures, each type of polymer is used in suitable applications. Although there has been a tremendous revolution since the discovery of synthetic polymers, certain issues can still be improved, such as mechanical stability and biocompatibility etc. These concerns are addressed since last decade trying to exploit the exceptional properties of nanoparticles, with excellent results, but the constant evolution of the field of nanotechnology suggests that still there is plenty of room for improvement.

1.1 Motivation

1.1.1 Brief history of nanocomposite polymers

Synthetic thermoplastic polymers are a valid alternative to metals in specific applications, for their distinct properties, such as light weightiness, ease to manufacture, environmentally friendliness, low cost and easily scalability. One major drawback of synthetic polymers is their poor mechanical strength, that can be addressed specifically by engineering thermoplastics with reinforcing functional fillers, as they can provide higher stiffness, strength and impact performance for metal replacement. Polymer composites are mixtures of inorganic and organic additives with certain geometry (fibers, flakes, sphere and particulates). Additives for thermoplastic polymers are usually functional fillers that mostly refers to short, flakes, platelets or particulates. In general, the parameters affecting the properties of thermoplastics are size and shape of the fillers, their composition, interaction of components at the phase boundaries and the method of fabrication. In developing reinforcing fillers, the aim is to increase the aspect ratio of the particles and to improve their interfacial adhesion with the chemically dissimilar polymer matrix. Further these reinforced fillers can be chosen to improve, electrical, thermal properties and flame retardancy of polymers.

Polymer nanocomposites exist in the market since decades, as carbon black, diatomite and pyrogenic silica were used as additives in polymers but their effect of properties induced by nanometric scale fillers was not fully understood. The very first investigation of nano-fillers incorporated in polymer matrix started in 1993 when Kojima et al.[4] studied the properties of polyamide-6 by adding nanoclays, they named it hybrid material. Since then numerous research has been conducted for improving the properties of thermoplastic polymers. Nowadays, the development of polymer nanocomposites is one of the most active area for development of nanomaterials. Some of the nanofillers used in nanocomposites are nanoclays, nano-oxides, carbon nanotubes, graphene nanoplatelets (GNPs), metallic nanoparticles etc. Nanoscale dimensions can significantly increase physical interactions, physio-chemical and chemical interactions in materials and as a consequence the morphologies obtained for the nanocomposites and the ability to modify the interfaces are essential for improvements[5].

1.1.2 Improving mechanical and tribological performance

In modern applications, nanocomposites has found immense utility in improving energy efficiency, health sector, food packaging etc. The incorporation of nanomaterials can improve a polymer's properties such as its Young's modulus, tensile strength, impact and scratch resistance, electrical and

thermal conductivity, tribology improvement etc. Recent advancements could usher in new applications where mechanical fragility is the concern for polymers. The growing interest in polymers will continue to emphasize the importance of attaining optimal performance by incorporating nano-fillers.

Insufficiencies in impact and scratch resistance of polymers and their poor adhesion primarily manifest themselves as a drawback, because these embody the low surface energy and short chains, hindering for replacement of high performance materials. Specifically when dealing with scratch resistance, intrinsic strength of materials along with better adhesion with the substrates play a very critical role.

1.2 Background

1.2.1 Nature inspired non-wettable surfaces

Superhydrophobic non-wetting surfaces have got significant interest due to their numerous applications in water repellency, self-cleaning mechanism, antifouling phenomenon, flow enhancement and anti-corrosive properties to name a few. Usually superhydrophobicity is defined by two criteria; first the apparent contact angle (APCA) that should be greater than 150° and secondly, water must not stick to the surface, i.e. the rolling angle (RA) should be lesser than 10° [6]. The second condition directly links the contact angle hysteresis $\Delta\Theta$ which is the difference between advancing contact angle $\Theta(adv)$ and receding contact angle $\Theta(rec)$. To understand the concept of superhydrophobicity, it is necessary to discuss about nature inspired surfaces such as the wings of butterflies, lotus leaf, shark skin, rose petals etc. Depending on their surface morphology, they are classified into two categories namely non-adhesive superhydophobic surfaces and adhesive superhydrophobic surfaces.

In 1997, Barthlott and Neinhuis discovered the self-cleaning properties of the lotus leaf that lead the inspiration of an intensive work on bio-based artificial non-wettable surfaces[7]. Lotus leaf has the distinct property of non-adhesive water-repellency that can be explained by looking at the micro and nano-structures (Figure 1.1). Electron microscopy studies revealed that the presence of protrusions on the surface, named papillae, with average size of tens of microns (Figure 1.1b) covered by epicular waxes of few hundred nanometers (Figure 1.1c) are responsible for creating superhydophobicity. When water droplet hits the surface of lotus leaf surface, they rest on the hydrophobic wax crystals on top of the papillae, resulting in minimizing the leaf/droplet contact area. Empirically water bridges

between adjacent papillae, leaving air pockets in between them leading to contact angle of more than 150° and extremely low sliding angle.

Lotus Leaf   **Papillae**   **Wax Crystals**

Rose Petal   **Micro-papillae**
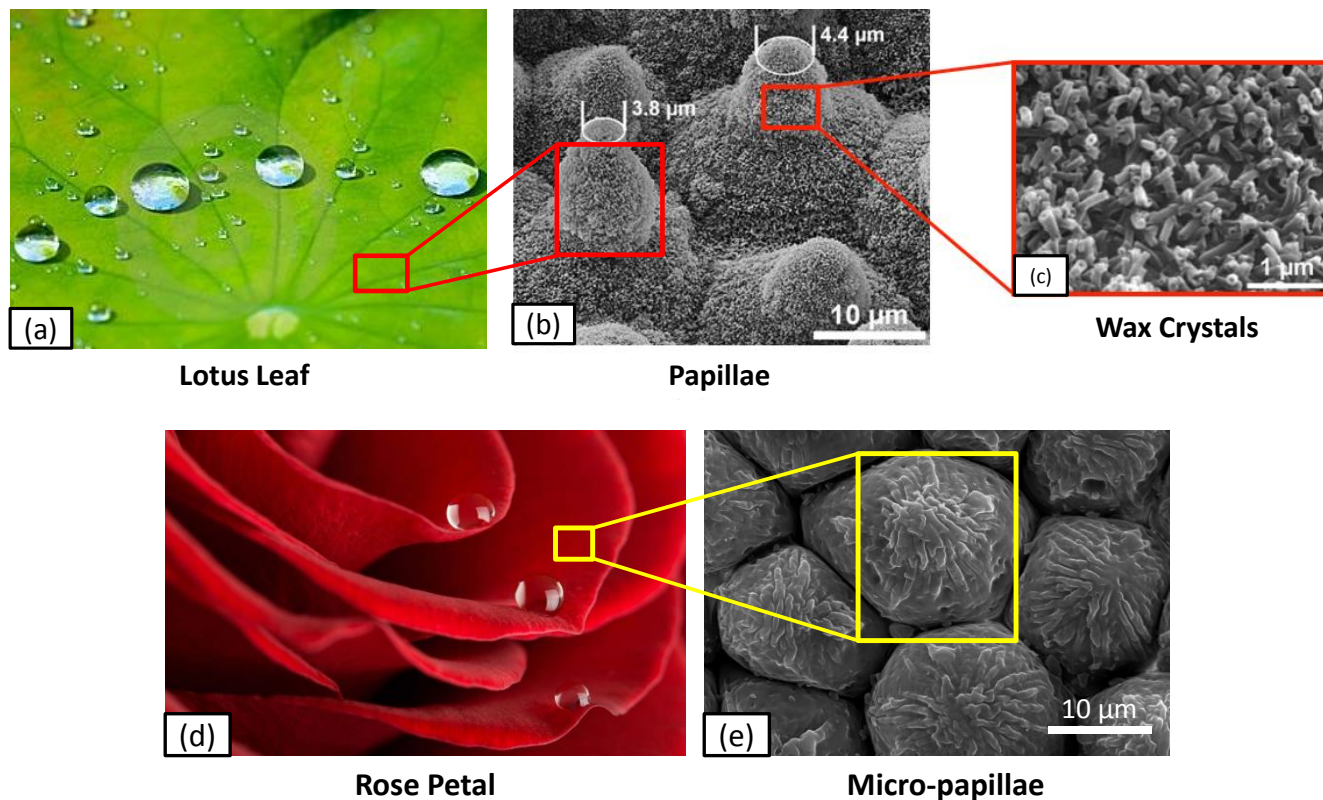
Figure 1.1. Nature inspired macro, micro and nanostructures of lotus leaf and rose petal[8].

Conversely, rose petals are the best example of adhesive superhydrophobic surfaces found in nature. This behavior can be explained by looking into the microscopic structure of rose-petal surface (Figure 1.1e). Although a microstructures can be observed however unlikely with lotus leaves, air pockets between the adjacent surfaces are not observed. Therefore a water droplet made in contact with the rose petal surface sinks inside the surface features with the consequent increase in water adhesion. The wetting behavior of the these natural systems is highly interesting in understanding the mechanism that superhydrophobicity is not only the consequence of surface chemistry but also it depends on the surface topography and surface roughness. These bioinspired superhydrophobic materials left the inspiration for researchers to work on it as Cassie and Baxter were the first two scientists who proposed the phenomenon in 1944 that hierarchical structure can trap a layer of air between water and the surface thus reducing the adhesion while ensuring good mobility of water droplets, shown by equation

$$\cos \Theta_{APCA} = f \cos \Theta_Y - 1 + f$$

Where Θ_{APCA} is the apparent contact angle, Θ_Y demonstrates the intrinsic contact angle of the surface and f represents the wet area fraction. The hydrophobicity of such surfaces patterned with topography can be degraded either by loss of roughness or by introduction of hydrophilic contaminants that results in transition from Cassie Baxter state to Wenzel state.

Concluding the discussed phenomenon, the unusual wetting characteristic of superhydrophobic surfaces is governed by both the chemical composition and the geometric structure. In general, smooth hydrophobic surfaces can have an intrinsic contact angle up to 120° but for attaining the superhydrophobicity, roughening of the hydrophobic surfaces with micro and/or nano-scale features is essential.

1.2.2 Abrasion induced superhydrophobic surfaces

The non-wettability of a superhydrophobic surface can be degraded by environmental mechanisms (chemical reactions with solvents and gases, UV exposure, bacterial contamination) and mechanical wear. In mechanical wear, major milestone is the control over mechanical fragility that damages the structure and results in loss of liquid repellency and increase in contact angle hysteresis. There are multiple factors that can affect the performance of superhydrophobic coatings including substrate adhesion, tangential abrasion, dynamic impact, liquid bath. A proper adhesion with the substrate has paramount importance as lack of strong adhesion to the substrate will cause the detachment of the coating in case of minor/major applied mechanical force. Similarly rubbing between two solid surfaces is a common phenomenon that can occur anywhere in daily life named as tangential abrasion where a solid abradant moves tangentially to the tested surface (exemplified in Figure 1.2). Another factor that can influence the surface stability is the dynamic impact of collisions when a solid, liquid or gaseous phase hits the sample from a controlled/uncontrolled height.

There are numerous methods defined to identify the durability of superhydrophobic surfaces including linear abrasion, circular abrasion, sand abrasion, tape pealing, blade scratching, ball on disk sliding and water jet testing. Among all these tests, most significant test is linear abrasion test that can give precise reproducible results on large surface area and can produce a uniformly abraded surface. A linear abrasion test involves rubbing of a solid flat abrader against the surface under normal load, as shown in Figure 1.2. Different abrading materials are usually used to measure the wear abrasion of sample surfaces including textile, rubber, and sandpapers under different applied loads.
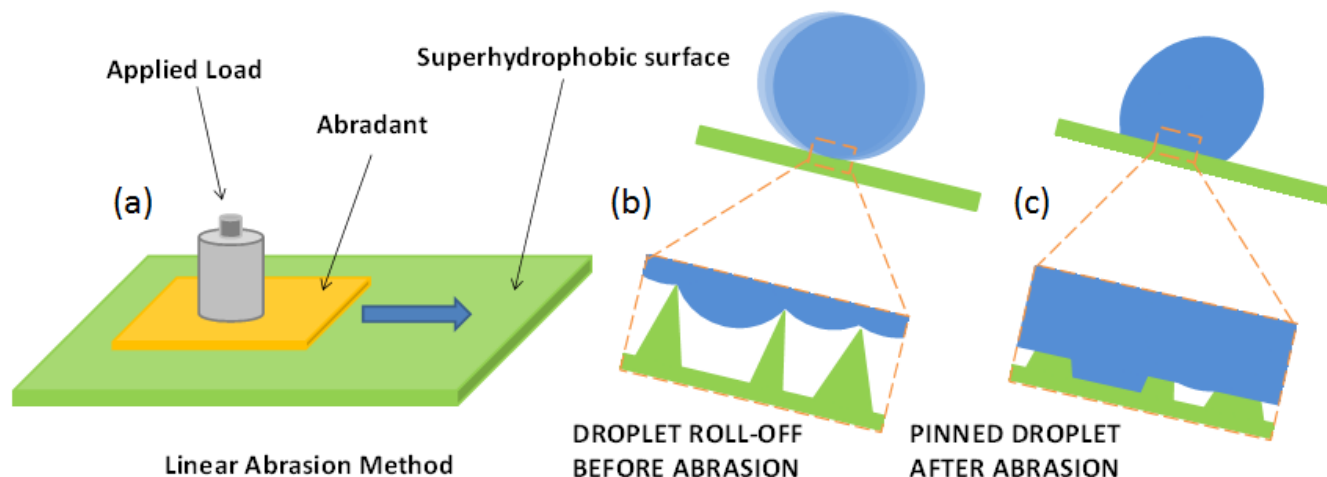
Figure 1.2. (a) Schematic of linear abrasion test on superhydrophobic surface. (b) Mechanism of trapping of air between rough asperities. (c) Damaging of surface roughness after abrasion and droplet pinning[9].

Many recent studies has demonstrated the usage of roughness at two length scales (micro and nano-level) helps to ensure the stability of Cassie state after the surface is exposed to any mechanical damage. However still it is very challenging to develop superhydrophobic coatings with improved mechanical properties that can withstand severe wear abrasion.

1.2.3 Tribology of nanocomposite materials

Tribology is the study of different aspects of surface engineering, friction, wear rate and lubrication between interacting surfaces in relative motion. The fundamental objective is to minimize the material loss or damage when a counter material is brought into contact and to reduce the energy dissipation during the surface interactions. The tribological properties of polymers are generally improved with the addition of lubricating and/or reinforcing fillers. Lubricating fillers include polytetrafluoroethylene (PTFE), graphene and molybdenum disulfide (MoS_2) whereas reinforcing fillers are glass fibers, carbon fibers, etc. Reinforcing fillers help to increase the mechanical strength of polymeric material but on the contrary increases the abrasiveness of the counterpart, leading to increase in the friction coefficient and third body wear of the composites, which is undesirable. Lubricating fillers are more beneficial for tribology processes as they create a transfer film on counter-surfaces and reduce the friction which prevents the material damage. Nanofillers are preferred to incorporate in matrix polymer chains as it improves the interfacial interaction and enhances the nucleation capability.

Furthermore nanofillers also helps to restrict the mobility of polymer chains in their vicinity and influence the rigidity. In particular, from the tribology point of view, the small size of nanoparticles with homogenous dispersion in the polymer matrix can conjure the performance.

Wear damage in polymer nanocomposites is caused due to two categorized wear mechanisms namely cohesive and interfacial wear processes. Cohesive wear processes are mainly caused by the mechanical induction of the interacting bodies such as abrasive, fatigue, delamination and fretting wear. In contrast, the interfacial wear process involves dissipation of the frictional work and increases the local temperature as polymers have low melting temperature and thermal conductivity than metals that can lead to softening, melting, oxidation on the polymeric surface. On the other hand, interfacial processes include transfer wear and chemical or corrosive wear[10].

Although polymer nanocomposites are replacing metals for owing adequate strength, lightness, versatility and ease of processing but due to their viscoelastic properties, analysis of tribology on such surfaces is complicated. Especially in case of nanocomposites, detailed knowledge of nanofillers during the tribology processes, and their relationship between structures, substrates and processing is required. Tribology response of polymer nanocomposites, specifically on wear, scratch damage, mechanism of transfer film on counterparts and role of adhesion with different substrates in solid lubricants is relatively unexplored.

1.2.4 Adhesive/antiadhesive surfaces

Adhesion is a phenomenon where interatomic and intermolecular interactions occur at the interface of two surfaces. There are three primary mechanisms for adhesion namely mechanical coupling, thermodynamic adhesion and molecular bonding. Mechanical coupling involves mechanical interlocking based on the principle of hook and eye, keying into the surface of the substrate. Thermodynamic adhesion involves minimization of the surface free energy by orienting the surface into non-polar region of the adhering material and is based on the equilibrium processes at the interface. Molecular bonding mechanism is based on entailing intermolecular forces between adhesive and the substrate such as Van der Waals forces, dipole-dipole interaction, ionic, covalent and metallic bonding. A proper understanding of adhesion technology has significant impact as of its applications in aerospace, engineering, automotive and biomedical where strong adhesion or non-stick conditions are required. One of the best examples in nature for adhesion mechanism is geckos that seems to defy gravity as they can run along vertical smooth surfaces[11]. The secret of geckos adhesive capabilities lies

in their feet toe pads that consists of series of lamellae (Figure 1.3a), each one covered with uniform arrays of similarly oriented hair like bristles called setae (Figure 1.3b) and further single gecko seta consists of nanoscale array of hundreds of spatulae tips (Figure 1.3c). Different hypothesis were explained for understanding the geckos adhesion elusive mechanism that proposed that it's due to micro-interlocking or due to the friction caused by the small nanoscale foot-pad setae that resists against the climbing surfaces and it is proved that strength of the adhesion of geckos depends largely on the geometry of the foot-pad setae[12]. This phenomenon of adhesion in case of geckos is well connected with nanoparticles that at micro and nanoscale high aspect ratio is the key for contributing towards exceptional properties, one of them is adhesion.
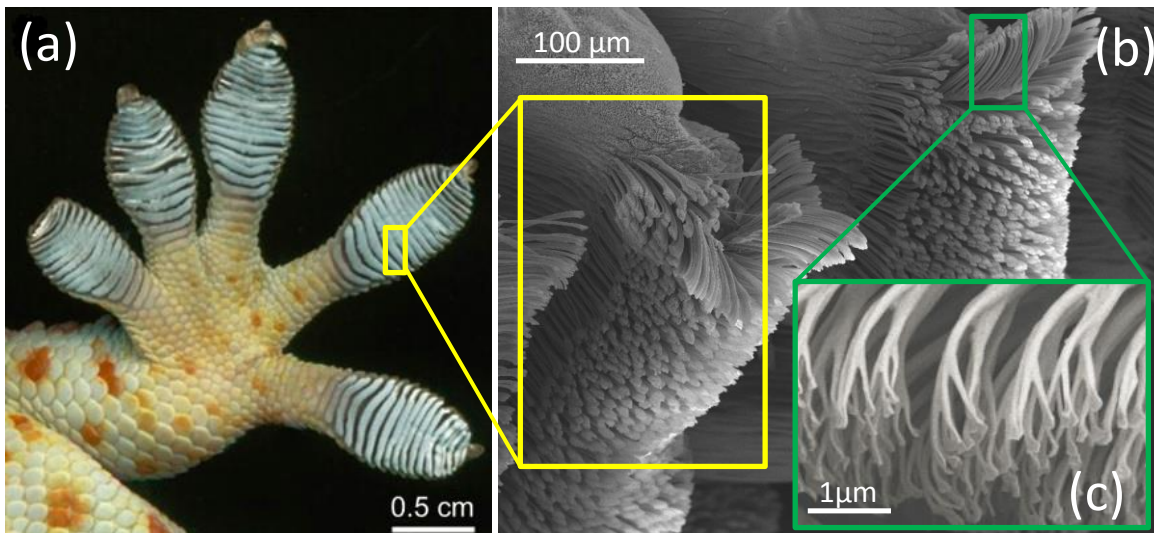
Figure 1.3. (a) Feet toe pads of gecko. (b) SEM image of hair like bristles, setae. (c) Nanoscale arrays of spatula tips [12]

Based on the concept of molecular adhesion, it is possible to change the adhesive properties of surfaces by introducing chemical charges. By tuning surface chemistry, it is much possible to fabricate the surfaces with adhesive/antiadhesive properties.

1.3 Thesis objectives and outline

This thesis will aim to provide an understanding on tailoring and tuning the surface composition of polymers and their subsequent effects on abrasion, adhesion, friction and wear. A framework will be defined to show how nanofillers enhance the hydrophobicity of the polymer composites and how thermal annealing induces a significant improvement in the wear abrasion response. In this framework, we will elaborate the role of primer layer for better adhesion with the substrates and how it impacts the

performance of wear abrasion. Furthermore, a perspective will be given that wear abrasion testing with steel counterpart can be a possible option for future applications where superhydrophobicity and tribology are concerned in conjugated applications.

Focusing further in the field of tribology, further work is also focused on the improvement of friction and wear rate of high-density polymers by incorporating 2D and 3D lubricating fillers. A mechanism is proposed that how a transfer film on counterpart material can help in reducing friction, hence minimizing the material damage. Further explanation is described that ow nanofillers impact in improvement of adhesion with substrates. In addition, an effort has been done to improve the tribology and adhesion of short chain polymers where surface chemistry is tuned to improve tribology and adhesive/antiadhesive properties of the material. Lastly, a biocompatible polymer is synthesized and its perspective applications are explained where improvement in tribology and adhesion is addressed.

We will begin in chapter 2 where details of fabrication of wear resistant superhydrophobic coatings on metal substrates from recycled and non-toxic polymers are explained. Further, the role of a primer layer and of thermal annealing on performance of wear abrasion and tribology of superhydrophobic coatings is investigated. In chapter 3, we will introduce the 2D and 3D fillers in high density polymers and their consequent effects on adhesion and tribology will be examined. The role of transfer film for minimizing the friction and material damage will be discussed. In chapter 4, we demonstrate the improvement in friction and wear of water soluble environmental friendly acrylic copolymer by manifesting the change in chemical composition. In addition, adhesive/antiadhesive properties will be related to the tuning of surface chemistry. In chapter 5, we will discuss the optimization of a method that allows the fabrication of a biocompatible transparent polymer, with special attention to the effect of plasticizer. Finally, in chapter 6, conducted research will be summarized and future directions will be discussed.

2. Analysis of wear abrasion resistance of multilayer recycled high impact polystyrene (HIPS) nanocomposites

2.1 Introduction

Plastics are one of the fastest consumed materials in daily life and their consumption is growing tremendously worldwide. They are the best candidates for replacement of metal components, a relevant example is in packaging where plastic materials are saving 14.2 million tons of oil, ultimately reducing 47.3 million tons of CO_2 per year. Polystyrene, a member of plastic family, is among the most abundantly used plastic with several million tons of production per year [13]. Although polystyrene is widely used for low cost products but its brittle nature hinders in implementation for different industrial uses [14].

To address the aforementioned concern, high-impact modifier copolymers are usually grafted with polystyrene to form an immiscible polymer blend. Polybutadiene is generally mixed with polystyrene to form high impact polystyrene (HIPS) widely used in automotive industry, food packaging, electrical appliances and as building material due to its outstanding properties including good impact resistance, good dimensional stability, recyclability, ease of process and low cost [15,16,17]. HIPS is previously studied in various domains as Braun et al.[18] studied the flammability, thermal and thermo-oxidative properties of HIPS for building materials, Wang et al.[19] investigated the performance of cement mortar made with recycled HIPS, Zhang et al.[20] reported improvement in young's modulus, tensile strength, impact strength and hardness of HIPS by incorporating TiO_2. Although polystyrene is investigated by many researchers for superhydrophobic coatings as Qing et al.[21] reported the fabrication of superhydrophobic polystyrene by adding ZnO primarily used for cotton textiles. Zhu et al.[22] prepared the conductive superhydrophobic polystyrene composite corrosive films for corrosive environments and Xue et al.[23] fabricated the self-healing superhydrophobic surfaces of polystyrene incorporated by SiO_2 nanoparticles, resistive against severe abrasion. According to best of our knowledge, HIPS is never used before for superhydrophobic surfaces specifically for abrasion and tribological perspective.

Superhydrophobic surfaces have received great attention in recent years due to their excellent water-repellency, self-cleaning, anti-icing, antifouling and anticorrosive properties[24,25,26,27,28]. Superhydrophobic coatings are generally fabricated through surface texturing (e.g., hierarchical texture, micro and nanoscale texture) and by chemical modification following the low solid surface energy. In hierarchical texture, surface roughness allows air to be trapped between liquid and the

structures, while the liquid is suspended on the tips of the asperities called Cassie-Baxter state. The Cassie-Baxter state is preferred for obtaining superhydrophobic surfaces as the air pockets reduce the solid to liquid contact area; hence increasing the apparent advancing and receding contact angles while reducing the contact angle hysteresis [29].

However, one major milestone in fabricating robust superhydrophobic surfaces for commercial applications is good substrate-coating adhesion, better wear resistance and excellent anti-abrasion properties[30, 31]. Recent studies reveal that existence of rubbery phase in the coating formulations can impact significantly and improves resilience against abrasion-induced non-wetting texture damage [32]. Since HIPS thermoplastics already contain dispersed micron-sized rubber particles, it could be a model polymer matrix for wear resistant non-wettable nanocomposites.

Substrate-coating adhesion can be achieved by either mechanical adhesion (substrate roughness, mechanical interlocking) or bye the contribution of electrostatic forces, Van der Walls forces, surface energy and molecular boding. Conventionally, mechanical interlocking is achieved by abrading the substrate, allowing the coatings to fill pores, hovels, crevices and micro voids on the substrate. Another approach is to use primer layer which helps to facilitate the susceptible poor adhesion of superhydrophobic surfaces with substrates, providing adequate mechanical strength. In our case, we used perfluorinated acrylic copolymer as a primer layer and investigated the durability by annealing it at different variant temperatures.

In the present work, we present that addition of silica helped to control the surface mechanics, hence, allowing the formation of superhydrophobic nanocomposite coatings bearing good mechanical and tribological properties. Mechanical and chemical properties of the resultant nanocomposite coatings were analyzed systematically by means of several analytical and spectral techniques. The recycled HIPS nanocomposite coatings exhibit better abrasion resisting properties and maintained the superhydrophobicity after linear abrasion cycles. Composite-substrate adhesion was improved by applying an environmentally friendly perfluorinated acrylic copolymer layer. Moreover, the coatings display significant reduction in friction and wear rate after incorporation of silica at a judicious concentration. Post-annealing of composite coatings resulted in phenomenal improvement in abrasion resistance and hydrophobicity.

2.2 Materials and Methods

HIPS polymer with rubber content of ~ 8-13 wt. % that was originating from urban recycled waste was purchased from Heathrow Scientific USA. The average molecular weight (M_w) of HIPS is 260,000 and number average molecular weight (M_n) is 150,000. Molecular weight of rubbery phase (polybutadiene) is 120,000 and M_n 100,000, respectively. HIPS contains approximately 35% of the rubber that is grafted to the polystyrene. Polystyrene beads were purchased from Sigma-Aldrich and used as received.

Perfluorinated acrylic copolymer (PFAC; Capstone ST-100), a commercial aqueous solution was purchased from The Chemours Company, USA [33]. Formulation was based on approximately 20 wt.% polymer dispersed in water. Hydrophobically modified siloxane treated fumed silica, AEROSIL® R812, with an average particle size of 7-40 nm was kindly donated by Evonik industries, Germany. Aluminum substrates with 5.0 cm in length, 2.5 cm in width and thickness of 1.0 mm were purchased from RS components. Reagent grade trifluoroacetic acid (TFA), acetone and chloroform were purchased from Sigma-Aldrich and used as received without any further modification.

2.2.1 Preparation of the nanocomposites

The commercially available water-dispersed perfluorinated acrylic copolymer (PFAC) has been developed for porous structures for the purpose of penetrating stain resistant sealant. Direct transfer of water-dispersed PFAC on smooth surfaces by spraying or roll coating does not produce smooth and adhesive coatings. Hence, a protocol has been developed to be extracted from its aqueous dispersion[34]. In order to precipitate PFAC from the stabilized water dispersion, equal amount of volumes of as received aqueous dispersion and TFA were mixed using a vertex for five minutes at room temperature. A solid precipitated elastic rubbery polymer was obtained by pouring the supernatant, washed several times with distilled water, dried overnight under ambient conditions and dissolved in acetone and 10% by weight solution was formed [35,36]. Furthermore, dilution of the obtained PFAC was done again to get 4% w/v solution for spraying.

For second layer formulation, weighing boat containing high impact polystyrene (HIPS) was dissolved in chloroform with 2wt%. Afterwards hydrophobic silica nanoparticles were mixed into the solution to produce polymer/nanoparticle (HIPS/SiO$_2$) suspensions with varying nanoparticle weight percent with respect to the polymer (0%, 10%, 20%, 30%, 40%, 50% and 60%).For good dispersion of silica nanoparticles, probe sonication was performed for 2 minutes for each of HIPS/SiO$_2$ solution and

was bath sonicated for 3 hours at 59 Hz. To avoid any contamination on surface, the aluminum substrates were cleaned by acetone prior to spray-deposition. Different formulated solutions were then sprayed onto aluminum substrate using an internal mix airbrush spray system (model VL-SET, Paasche). Spray coating was driven by high-pressure airstream at 200 kPa pressure. The distance between the sample and nozzle head was approximately 15 cm.

Perfluorinated acrylic copolymer solution was first deposited onto aluminum substrates and were kept in ambient environment for solvent evaporation following the heat treatment on hot-plate for 5 minutes at 180° C lately. After the deposition of first layer of perfluorinated acrylic copolymer, HIPS/SiO$_2$ solution was sprayed on primer polymer layer by following the same spraying parameters. After spraying, the aluminum substrates were left under ambient environment for 1 hour to evaporate the solvent. HIPS/SiO$_2$ composite layer was annealed by heat gun at 340° C for 2 minutes. For better precision of results, distance between heat gun and specimen was calculated around 5cm while temperature reaching the composite film was confirmed by temperature sensor and was recorded around 220° C. Thickness of the HIPS/SiO$_2$ composite film was around 20-25 µm whereas thickness of the deposited acrylic copolymer film was around 2µm. A schematic of multilayer composition is shown in Figure 2.1.
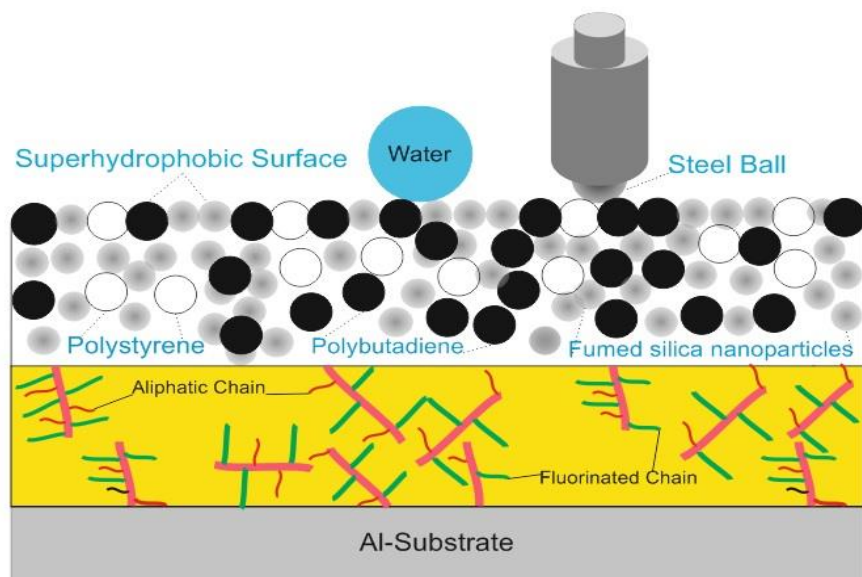
Figure 2.1. Graphical representation of multilayer HIPS nanocomposites. Primer layer contains aliphatic and fluorinated chains whereas HIPS polymer matrix contains polystyrene, polybutadiene and fumed silica nanoparticles.

2.2.2 Morphological characterization

For analyzing the morphology of nanocomposite coatings, scanning electron microscope (SEM, JEOL JSM-6490AL) with 10 and 15 KV accelerating voltage was used, after the specimens were coated by a thin (15 nm) gold layer. For cross section SEM imaging, direct freeze fracture method was used after treating the samples in liquid nitrogen for 10 seconds. Whereas, energy dispersive X-ray (EDX) analysis was performed to see chemical compositions at 10 kV acceleration voltage, 10 mm working distance and 15 sweep counts. Transmission electron microscopy (TEM) was used to characterize the morphology of as received HIPS. Approximately 100 nm thick slices were obtained by cutting the HIPS sheets with an ultra-microtome. The slice was stained in OsO_4 vapor for 10 h before TEM imaging. Images were acquired using a JEOL JEM-1011 TEM (W filament) TEM operated at 200 kV accelerating voltage.

Atomic force microscopy (AFM) images were obtained by a Park system AFM instrument (XE-100) in non-contact tapping mode, mounted on an anti-vibration table (Table Stable TS-150). The AFM was enclosed by an acoustic enclosure. Single-beam cantilevers tips (PPP-NCHR-10M) were used for the data acquisition with less than 10 nm nominal radius and 42 N/m elastic force constant for high sensitivity. The scan rate was between 0.1-0.2 Hz with scanning zoom area of 10×10 μm^2. The resonance frequency was defined around 320 kHz. Acquired images were further processed with WS $\times$ M 5.1 processing software. The roughness characteristics of the surfaces were further determined by using a built-in grain analysis statistical algorithm. The process involves the watershed algorithm that is usually employed for local minima/maxima determination and image segmentation in image processing. AFM topography images are segmented into many zones identified with a certain average roughness. The mean roughness of the image is calculated by averaging the roughness values obtained from three different areas [37].

2.2.3 Variable-angle ATR-FTIR measurements

Variable-angle ATR-FTIR spectra of the samples were obtained with an ATR accessory (Veemax III, PIKE Technologies) coupled to a FTIR spectrometer (Equinox 70 FT-IR, Bruker). All spectra were recorded in the range from 3800 to 600 cm^{-1} with 4 cm^{-1} resolution, accumulating 128 scans. In a typical measurement, the films were gently deposited on the spot of the ATR accessory (ZnSe crystal) and slowly pressed. To ensure the reproducibility of obtained spectra three samples of each type were measured.

The analyzed depth, d_p, of ATR-FTIR spectroscopy depends on several factors such as the wavelength λ, the effective angle of incidence θ_e, the refractive index of the ATR crystal n_1, and the sample n_2, as indicated in the following equation:

$$d_p = \frac{\lambda}{2\pi n_1 \sqrt{\sin^2 \theta_e - (n_2/n_1)^2}} \tag{1}$$

In our variable-angle ATR-FTIR spectrometer $n_1 = 2.4$, n_2 is assumed to be around 1.6 [38] and θ_e may be calculated from the set angle θ_s, n_1, and the face angle of the crystal θ_f:

$$\theta_e = \theta_f + \sin^{-1}\left(\frac{\sin(\theta_s - \theta_f)}{n_1}\right) \tag{2}$$

Table 2.1 shows θ_e and the d_p at 1000 cm^{-1} for all the set angles used in this study.

Table 2.1. Calculated effective angles and analyzed depths for the different set angles used.

θ_s (°)	θ_f (°)	θ_e (°)	d_p at 1000 cm^{-1} (μm)
35	45	40.85	8.75
40	45	42.92	5.73
45	45	45.00	4.37
50	45	47.08	3.55
55	45	49.15	2.99
60	45	51.19	2.58
65	45	53.19	2.26
70	45	55.14	2.01
75	45	57.02	1.80

All spectra were normalized with respect to t d_p at 1000 cm^{-1} using the "ATR correction" command provided for the software (Spectra Manager v2). All spectra showed were measured at 45°.

2.2.4 X-Ray Photoelectron Spectroscopy (XPS)

XPS measurements were performed using a Kratos Axis UltraDLD spectrometer with monochromatic Al Kα source (photon energy = 1486.6 eV) operated at 15 kV and 20 mA. The analysis area was 300

μm × 700 μm in lateral dimensions. Three areas were analyzed throughout sample sizes of about 1 cm×1cm in order to obtain statistical values for atomic composition. Wide spectra (0 eV - 1200 eV) were acquired at pass energy of 160 eV with a step of 1 eV. The Kratos charge neutralizer system was used during data acquisition. Spectra were analyzed using Casa XPS software (version 2.3.16); data fitting was performed using Voigt profiles and Shirley-type backgrounds. High-resolution analyses were carried out with pass energy of 10 eV and step of 0.1 eV. Spectra were charge corrected to the main line of the carbon 1s spectrum set to 284.8 eV (C-C bond).

2.2.5 Annealing temperature measurements

HIPS nanocomposite coatings were annealed with a 2000W Bosch® heat gun. In order to precisely measure the temperature on the surface during hot air impact from a 15 cm distance, a Fluke VT02 visual IR thermometer was employed. After several experimental trials the best annealing temperature was set to 220° C.

2.2.6 Thermogravimetric analysis

Thermogravimetric Analysis (TGA) was performed by TGA Q500 (TA Instruments, USA) to estimate thermal degradation of PFAC, HIPS and HIPS/SiO_2 nanocomposites. Measurements were performed on 3-5 mg samples in an aluminum pan. Specimens were heated from room temperature to 800°C at a heating rate of 10°C /min in nitrogen atmosphere.

2.2.7 Wetting analysis

The apparent static water contact angles (APCAs) and droplet roll-off angles (RAs) were obtained by OCAH 200 (Data Physics, Germany) contact angle goniometer. A droplet volume of 5 μl was deposited and monitored for 30 seconds for all water contact angle (WCA) measurements. For each coating, five measurements were taken at different areas and average values are reported. All RA values were measured at dosing volume 7.5 μl droplet volumes under continuous tilting angular velocity of 1.58°/second. All experiments were performed at 20° C temperature. As soon as a droplet rolled away from the surfaces tilting was stopped and the tilt angle was recorded as RA.

2.2.8 Tribological characterization

Tribological properties of multilayer composite coating were investigated by Micro-Combi tester (Anton Paar GmbH, Germany). Multi-pass scratch tests were performed with a bearing steel ball of radius 500 μm to evaluate the friction and wear resistance. Tip displacement rate was maintained at 10mm/min for a reciprocating distance of 4mm under the constant load of 1N for 30 minutes, for a total

of 75 cycles. All the friction and wear tests were carried out at 20° C while relative humidity (RH) was kept at 40-50 %.

The average values of steady-state coefficient of friction were extracted from the experimental data plots of friction coefficient as a function of number of cycles and sliding distance. All the data presented in the current work were the average of five replicate measurements for each substrate. After each test, the depth of the wear scar d was measured using a stylus surface profiler. Each scar was measured 5 times and average was calculated to use the precise depth of the specimen. Wear volume ΔV of the specimen was calculated from geometrical considerations, by eq. (3),

$$\Delta V = \frac{L}{2} \, r^2 \left(cos^{-1} \left(\frac{r-d}{r} \right) - \frac{\sqrt{r^2-d^2}}{r} \right) \tag{3}$$

where L is the length of stroke in one cycle (mm) and r the radius of the counterpart steel ball (µm). Wear rate was calculated by the ASTM G-99 standard wear rate formula,

$$K = \frac{\Delta V}{F \times N \times L} \tag{4}$$

where F is the applied load (N), L the stroke length in one cycle (m) and N represents the total number of cycles, so that $N \times L$ is the total sliding length.

2.2.9 Wear abrasion measurements

Wear abrasion tests were performed using a linear abrader (Taber® Linear Abraser/Abrader, Model 5750) under a constant load of 17.5 kPa applied pressure, which was intentionally kept somewhat above the general values reported in literature (equal or less than 10 kPa) [39,40,41]. Abrasion tests were performed with a CS-8 calibrase abrasion cylinder tip with stroke length of 5cm, keeping the stroke speed constant at 15 cycles/min. The abradant covered a distance of 5 cm/cycle by performing a back and forth linear periodic motion. The APCA and RAs measurements were taken after every 5 linear abrasion cycles.

2.3 Results and Discussion

2.3.1 Nanocomposite morphology and annelaing

A representative TEM image of the as-received HIPS polymer is shown in Figure 2.2a. Similar morphology was also found in HIPS coatings after spraying and annealing the as-received polymer. As seen in Figure 2.2a, phase separation between the polystyrene and rubber appears in the form of

spheroids. The spheroids are not 100% rubber and are generally known as "salami-like" domains [42], the borders of which are made by the rubber phase. According to the manufacturer, the average rubber content is 10% by weight. This is a classical HIPS morphology that is common in all forms of HIPS regardless of changes in the rubber content, production routes or post processing conditions [15]. Furthermore, Figure 2.2a shows that the spheroids are well dispersed and their size distribution ranges from 2 μm down to 200 nm. The main purpose of rubber toughening of brittle polymers is to dissipate impact and stress energy via a mechanism known as matrix crazing (network of fine cracks). The rubbery phase prevents or delays transmission and transformation of the crazes into cracks. Note that a craze is different from a crack in that it cannot be felt on the surface and it can continue to support a load.
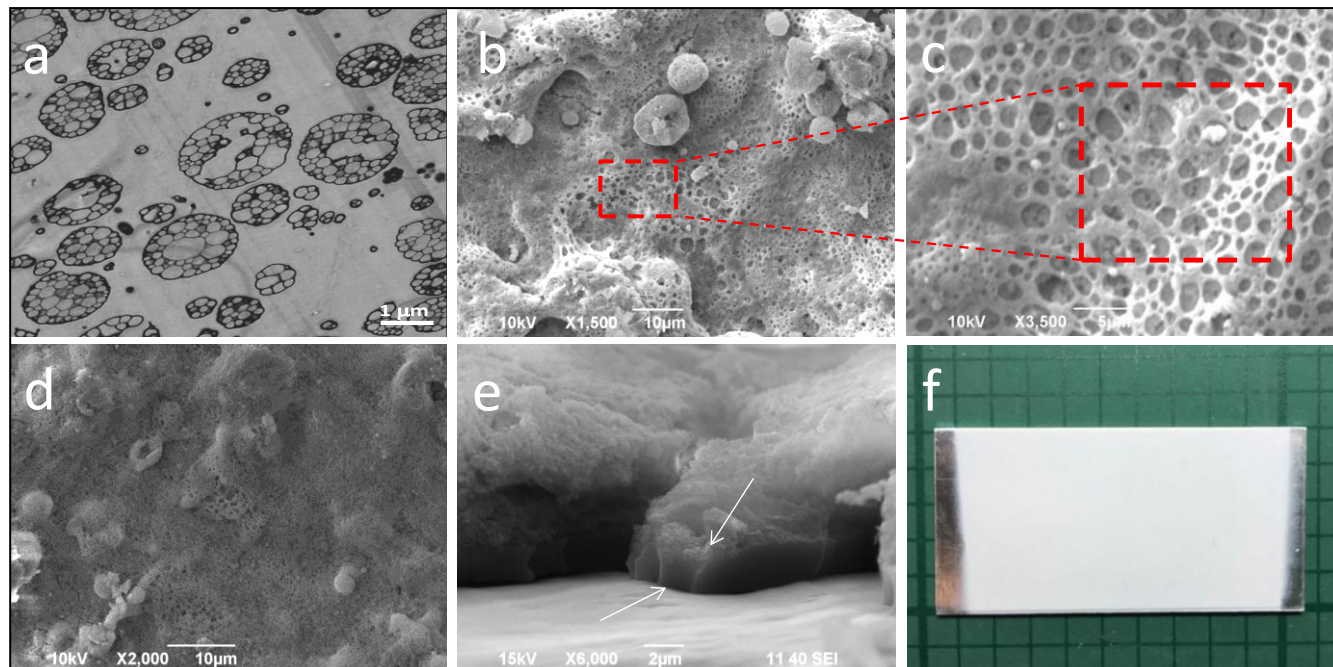
Figure 2.2. (a) Transmission electron microscope (TEM) image of the as received HIPS polymer. The sample was stained in OsO_4 vapor before microscopy. (b) SEM image of the HIPS nanocomposite with 50 wt% SiO_2 concentration (c) Foam like HIPS morphology is visible in the magnified image. (d) Nanocomposite surface morphology after annealing. The foam-like features are preserved. (e) Cross section SEM image showing the interface between the HIPS nanocomposite and the primer PFAC layer over aluminum. (f) Photograph of the annealed HIPS nanocomposite shown in (e) on an aluminum plate.

Loss of superhydrophobicity due to wear abrasion under pressure in polymer nanocomposites is generally attributed to two mechanisms, namely removal of nanoscale filler particles from the binder matrix and cracking and eventual chipping away of the polymer matrix [43]. Depending on the coating

"robustness", this could be reflected as smoothing out of the hydrophobic surface roughness features while the coating remains intact or complete coating failure due to massive material loss [44]. Detailed SEM images generally reveal such changes in morphology after wear abrasion tests. Recent studies show that presence of rubbery phases in such non-wettable nanocomposite coatings contributes to the energy dissipation and preserves superhydrophobicity longer under certain abrasion conditions [31].

Surface morphology of the HIPS/SiO$_2$ nanocomposite top coatings was inspected by SEM as shown in Figure 2.2(b-e). For example, surface morphology of HIPS/SiO$_2$ nanocomposite containing 50 wt. % SiO$_2$ nanoparticles before annealing is shown in Figure 2.2b. Topographical features closely resemble morphology of other non-wettable polymer-SiO$_2$ nanocomposites, with the exception that foam like cellular structures are visible throughout the coating (see Figure 2.2c). This is attributed to HIPS polymer matrix. These foamy structures are common in expanded polystyrene [45]. Presence of these features could be due to solvent evaporation from the coatings in the form of small bubbles that can act in a similar way to blowing agents used in the manufacturing of expanded polystyrene foams [46, 47]. Upon annealing at 220° C, the main morphology appears to remain practically unchanged as shown in Figure 2.2d and the cellular structures are preserved.

The primer layer ensured adhesion of the HIPS nanocomposite on the metal substrate. A cross section SEM image displayed in Figure 2.2e clearly shows that the HIPS nanocomposite top coat forms a uniform and well adhered coating on the ~ 2 μm thick primer layer after annealing. Although prior to annealing, the interface between the primer and the HIPS nanocomposite was also relatively uniform (not shown for brevity); annealing creates a process known as welding of two dissimilar polymer interfaces [48]. Inter-diffusion of both polymers across the interface due to annealing induces strength against fracture and adhesive failure at the interface [49]. Inspection of several other SEM images similar to the one shown in Figure 2.2e revealed that indeed welding between HIPS and/or HIPS nanocomposites and PFAC occurs with a very uniform continuous and crack free interface formation. This is also reflected in the overall macroscopic appearance of the coating as shown in Figure 2.2f.

Thermal annealing of polymer composites is performed in order to form "welding" between dissimilar polymer interfaces as well as polymer matrix-filler interfaces [50]. A secondary outcome is the migration of low molecular weight polymer chains as well as nanoscale fillers towards surfaces or cracks within the polymer matrix. In order to form welded polymer interfaces, thermal annealing needs to be done in such a way that the polymers are not degraded. Figure 2.3 shows the thermogravimetric

measurement results to examine the thermal stability of as-received HIPS and PFAC polymer (primer layer). Weight loss curves are compared in Figure 2.3a and the derivatives of weight loss curves are given in Figure 2.3b. HIPS polymer is a thermally stable resin. No significant weight loss was observed for as-received HIPS before 250° C, however, there exists approximately 7% weight loss between 250° C and 350° C that is attributed to the loss of residual monomeric styrene as well as some impurities originating from recycling process [51]. Major thermal degradation occurs around 425° C (Fig. 2.3b). As opposed to HIPS, PFAC polymer is not thermally resilient. It starts to lose weight at much lower temperatures and about 10% of its total weight is lost before 200° C. Close to 30% of the copolymer degrades at 250° C and between 300° C and 400° C almost all the polymer thermally degrades (Figure 2.3b). Hence, the thermal annealing conditions of the superhydrophobic coatings are dictated by the primer layer PFAC. Before reaching 200° C, however, a much less significant weight loss is noticeable (~ 7%) in PFAC polymer and this is attributed to losses related to surfactant molecules that is also observed with FTIR measurements. Therefore, the maximum hot-plate temperature employed for annealing was chosen to be 180° C. Note that a final annealing step at 220° C for two minutes was also performed (near melting point of polystyrene) by using a heart gun. This way, heat was directly supplied to the surface of HIPS/SiO$_2$ nanocomposite. The reason for this final step was to ensure better welding between the nanoparticles and the polystyrene matrix [52,53,54].
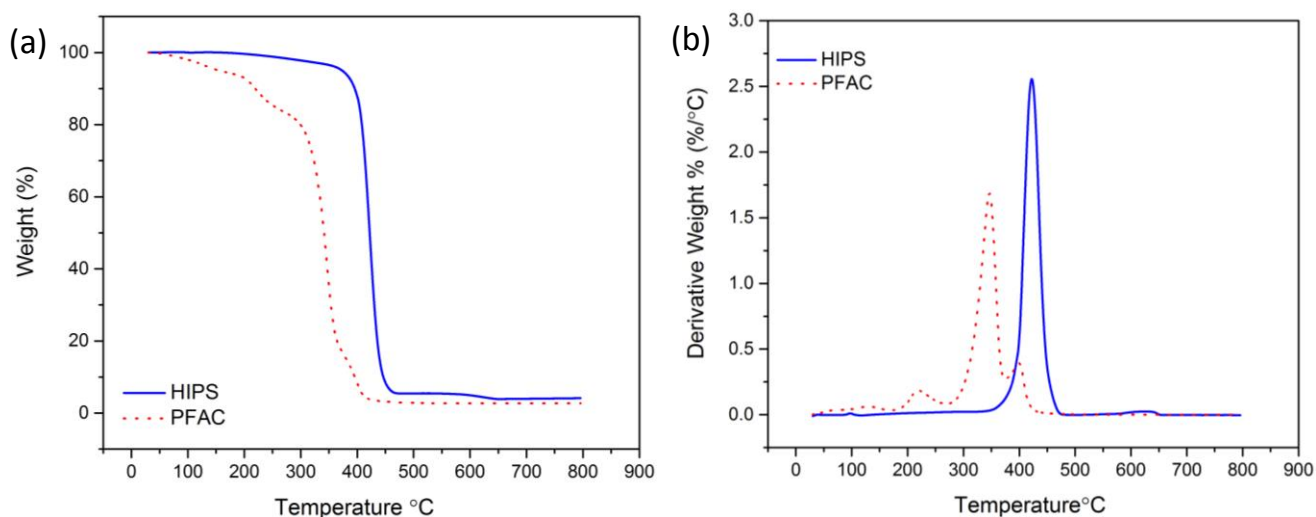
Figure 2.3 (a) TGA thermal weight loss plots for pristine HIPS and PFAC polymers. (b) Derivative of weight loss curves detailing major weight loss temperatures for HIPS and PFAC polymers.

Optimization of annealing also involved annealing of each coating with a different approach. For instance, annealing of pristine HIPS deposited on PFAC primer by suddenly placing it in an oven at

180° C or over a hot-plate creates bubbles and de-wetting zones in the coating as seen in Figure 2.4a. Similarly, HIPS/SiO$_2$ nanocomposites containing SiO$_2$ nanoparticles less than 30 wt.% annealed in the same way produces a network of cracks on the surface as seen in Figure 2.4b. Hence, coatings containing nanoparticles less than 50% by weight were annealed by gradually increasing the annealing temperature to its final value (i.e., 50° C in every 10 minutes). However, the best performing superhydrophobic HIPS/SiO$_2$ coating in terms of both tribological and non-wetting properties also resisted annealing by sudden exposure to 180° C and secondary 220° C without forming any cracks (see Figure 2.4c).
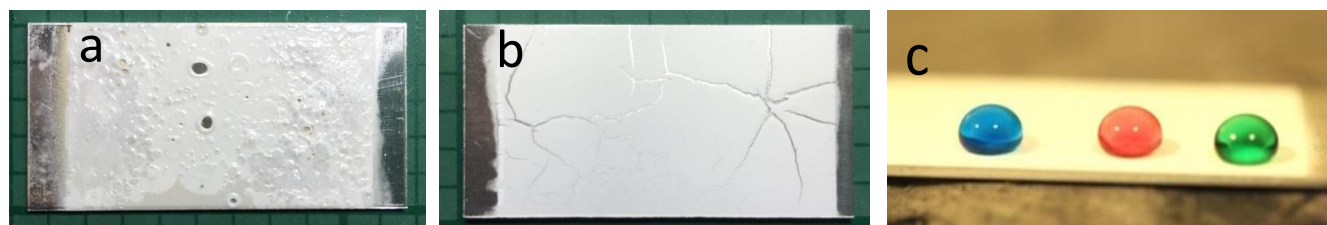
Figure 2.4 Photographs showing effect of annealing on various coatings. All coatings are applied over the PFAC primer. (a) Pristine HIPS coating exposed to sudden annealing temperature of 180° C. (b) HIPS/SiO$_2$ nanocomposite, 20% SiO$_2$, exposed to sudden annealing temperature of 180° C. (c) HIPS/SiO$_2$ nanocomposite, 50 wt.% SiO$_2$, exposed to sudden annealing temperature of 180° C.

2.3.2 Chemical characterization

2.3.2.1 Chemical characterization of the primer layer

The effect of the thermal annealing on the primer layer of PFAC was analyzed by ATR-FTIR and XPS, as illustrated in Figure 2.5. Figure 2.5A shows the infrared spectra of the pristine and annealed PFAC layers. Main bands for pristine PFAC were associated with –CF$_2$– groups (asymmetric and symmetric CF$_2$ stretching modes at 1238 cm^{-1} and 1143 cm^{-1}, respectively) and ester functional groups (C=O stretching mode at 1733 cm^{-1} and C–O–C stretching mode at 1192 cm^{-1}). Furthermore, a band at 1676 cm^{-1} was observed. This absorption can be assigned to the C=O stretching mode of some non-ionic surfactants, such as the condensation products of ethylene oxide with fatty acids that are used in the original polymer water dispersion [55]. This indicates that some of these surfactants are carried over into the acetone spray solutions during extraction. After thermal annealing, this band disappeared, indicating that surfactants were removed.

In addition, XPS was performed to further characterize the changes in surface chemistry induced by the thermal annealing of the primer layer shown in Figure 2.5B. The relative atomic

percentage of carbon, fluorine and oxygen were determined from wide spectra. Results indicated that F/C ratio was increased upon annealing which is probably due to the removal of some carbon-rich compounds from the surface. Furthermore, C1s peaks of pristine and annealed PFAC were deconvoluted. Both samples showed a similar profile characterized by the presence of C-C and C-H groups at 284.8 ± 0.2 eV, C-C-O groups at 285.8 ± 0.2 eV, C-O groups at 287.0 ± 0.2 eV, COOR groups at 289.1 ± 0.2 eV, CF_2 groups at 291.8 ± 0.2 eV and CF_3 groups at 294.1 ± 0.2 eV. Table S2 summarizes the calculated peak area percentages for each component. An increment of COOR and a decrease of C-O and C-C/C-H groups were observed. This could be related to the removing of surfactants revealed by ATR-FTIR spectroscopy. Presence of surfactants in polymer melts and solutions forces polymer chains to form micellar structures. Therefore, it is generally quite challenging to coat polymer films from micellar polymer solutions [56]. Removal of surfactants during latex film formation can cause rearrangement of the polymer chains allowing their assembly into a morphology minimizing air-polymer surface energy [57]. This also allows better interaction of the polymer chains with the substrate and with other dissimilar polymer chains in the absence of surfactants.
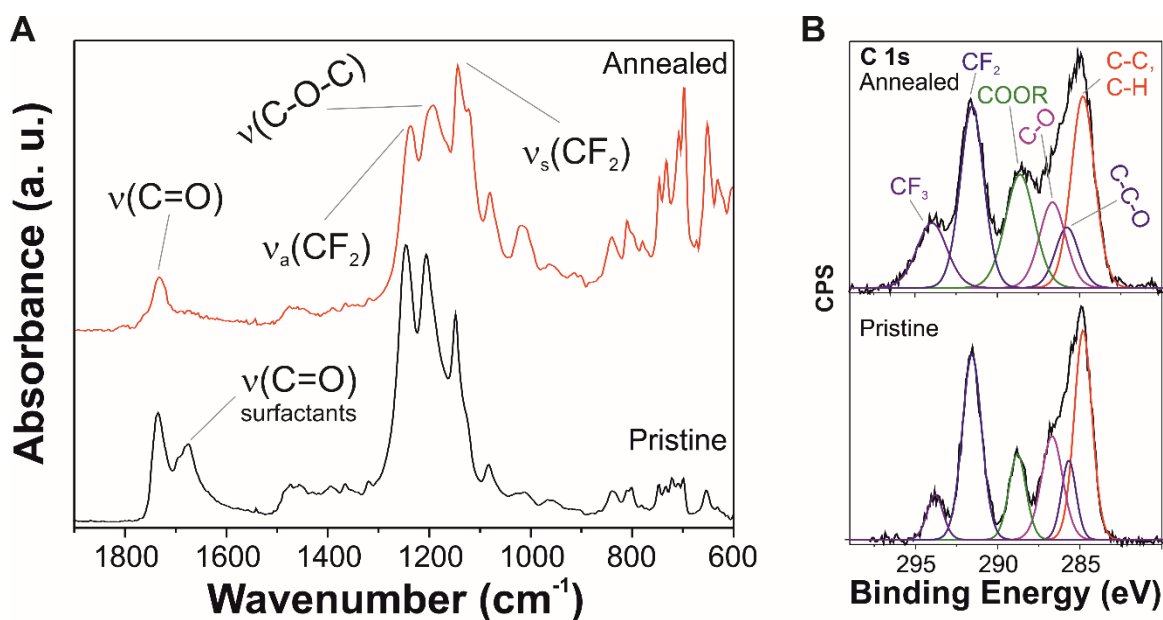
Figure 2.5. A, ATR-FTIR spectra of pristine and annealed layers of primer. Assignments of main vibrations are included. B, High resolution XPS spectra of C1s peak of pristine and annealed layers of primer. Deconvoluted peaks are included. Note that the annealed specimens are heat treated at 180°C on hot plate.

2.3.2.2 Chemical characterization of HIPS/Silica nanocomposites

Similar ATR-FTIR and XPS measurements were also conducted for the HIPS/SiO$_2$ nanocomposites to investigate the effects of thermal annealing, as shown in Figure 2.6. Figure 2.6A shows the ATR-FTIR spectra of pristine and annealed HIPS nanocomposites containing 50 wt. % silica nanoparticles. Bands ascribed to the polystyrene matrix were: C-H stretching mode of the ring in plane at 1491 cm^{-1}, C-H deformation of CH$_2$ groups at 1452 cm^{-1}, and two C-H out-of-plane bending modes of the ring at 749 cm^{-1} and 692 cm^{-1}, respectively [58]. The presence of silica nanoparticles was characterized by the broad band at 1086 cm^{-1} with a shoulder ~1220 cm^{-1}, indicative of amorphous silica. No chemical differences were detected when pristine and annealed samples were compared. However, variable angle FTIR measurements indicated that throughout the coating thickness, variations in the polymer to nanoparticle ratio were observed before and after annealing. This was indicated by the depth-dependent changes in the ratio between the band intensities at 1086 cm^{-1} (SiO$_2$) and 692 cm^{-1} (HIPS) as shown in Figure 2.6B. Clearly more nanoparticles migrate to the surface after annealing. This concentration density decreases significantly within the first 9 µm from the surface upon annealing. On the other hand, as-sprayed coatings dried under ambient conditions display a more uniform nanoparticle concentration density within the first 9 µm from the surface. To quantify this observation further, XPS measurements were also performed on the surface of the coatings. Figure 2.6C shows the wide XPS spectra for non-annealed and annealed samples where F, O, C and Si atoms were identified. The relative atomic percentages of these four elements are presented in Figure 2.6D. A low and constant amount of fluorine from the underlying PFAC layer was detected for both samples. The amounts of silicon and oxygen at the surface were increased upon annealing, with the consequent relative decrease of carbon atom signal intensity. Indeed, the Si/C ratio was increased by a factor of three upon annealing. In agreement with ATR-FTIR, XPS results also point out that annealed coatings have a higher concentration of silica nanoparticles on the surface in comparison to non-annealed ones. Formation of such nanoparticles density gradient in the polymer matrix induced by thermal annealing can be attributed to diffusion, relaxation and transport in thin polymer films [59]. In fact, diffusion and segregation of nanoparticles in polymer films toward the film surface or towards the cracks within the matrix are well studied and this behavior was proposed as a simple means of designing self-healing systems [60].
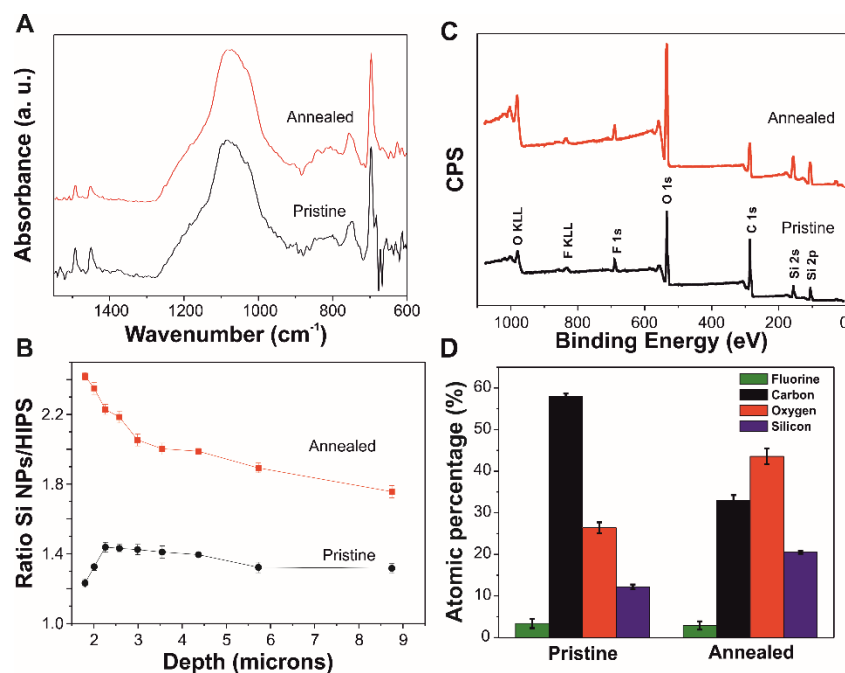
Figure 2.6. A, ATR-FTIR spectra of pristine and annealed nanocomposite samples. B, ratio of the intensity of bands at 1080 cm^{-1} and 692 cm^{-1} associated with Si NPs and HIPS, respectively, for pristine and annealed samples as a function of the depth of analysis. C, Wide range XPS spectra of pristine and annealed samples. D, atomic percentage of F, C, O and Si for pristine and annealed samples. Note that annealed specimens are further heat treated at 220° C with heat gun.

2.3.3 Wetting analysis

As-received HIPS polymer had an apparent static water contact angle (APCA) of 82±3°. The water droplets did not roll away upon tilting even at 90°. Incorporation of SiO$_2$ nanoparticles increased water contact angles by forming micro-nano-scale surface structures (Figure 2.7) as well as due to their hydrophobic surface functionalization [61]. Changes in APCA and water droplet roll off angles (RA) as a function of SiO$_2$ nanoparticle loading can be seen in Figure 2.7 along with the effect of annealing. Silica nanoparticle concentration of 20 wt. % results in water droplets to slide off the HIPS/SiO$_2$ coating surfaces, even though the APCA values are below 120°. As can been seen in Figure 2.7, at 20 wt.% SiO$_2$ concentration, annealing induces the reduction of droplet roll off angles from ~ 45° to 20°, which is a significant advantage for self-cleaning superhydrophobicity. Proper superhydrophobicity threshold (static contact angles exceeding 150°) in terms of APCA can only be obtained when SiO$_2$ concentration within HIPS polymer matrix reaches or exceeds 40% by weight. Annealing still reduces droplet roll off angles however significance of the effect declines compared to 20 wt.% and 30 wt.% SiO$_2$ concentrations. The best nanocomposite coating was achieved for SiO$_2$ concentration of 50% by

weight. Note that for this nanocomposite coating significance of annealing was almost negligible in terms of self-cleaning superhydrophobicity; however, it considerably enhances the tribological and wear abrasion resistance of the coating; as will be discussed next.
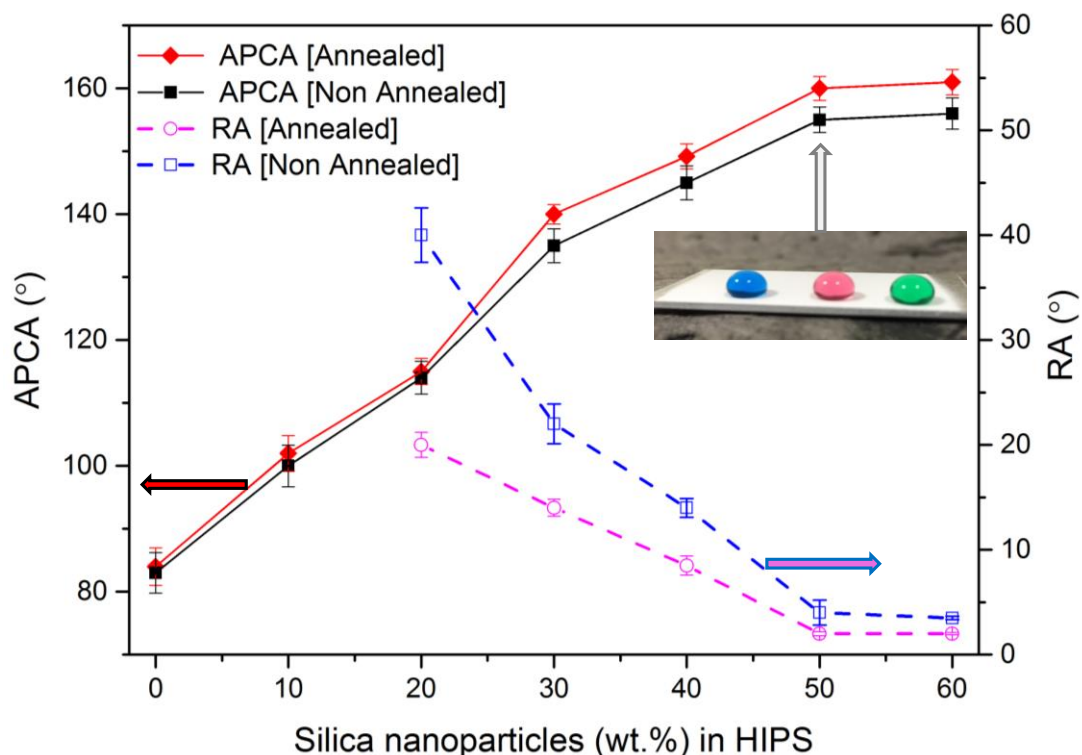
Figure 2.7. Apparent water contact angle (APCA) and droplet roll-off angles (RA) of HIPS nanocomposites with various silica concentrations. PFAC primer layer is present. Effect of annealing is also shown. The inset photo is taken on the coating displayed in Figure 2.2f. (Note that till 10 wt.% silica content, water shedding was not observed even at 90° tilting angle)

2.3.4 Wear analysis

Although there are many routes to measure robustness of the non-wettable surfaces such as tape peel tests for substrate adhesion, underwater ultrasonic processing, sand erosion damage, and abrasion induced wear, no appropriate methods and procedures for testing non-wettable surface robustness have been established yet [62]. Hence, we first performed tribology measurements to analyze frictional properties and scratch resistance of the coatings followed by a more industrial testing method known as Taber® tests to analyze the effect of repeated abrasion wear on superhydrophobicity and water droplet roll off angles.

Average surface roughness of all the coatings studied is presented in Figure 2.8a including the bare aluminum substrate. All the coatings were annealed. Self-cleaning superhydrophobic nanocomposites have approximately 1.4 μm average surface roughness. Once the SiO_2 concentration exceeds 50 wt.% the surface roughness increases by a factor of two. Friction coefficient and wear rate of the nanocomposites are given in Figure 2.8b. The friction coefficient values on nanocomposites between 10 wt.% and 50 wt.% SiO_2 concentrations are practically similar, however, at 50 wt.% SiO_2 concentration the wear rate is lowered by a factor of seven. In general, both the friction coefficient and the wear rate declines when SiO_2 nanoparticles are introduced in HIPS polymer. These measurements approve earlier reports that polymer nanocomposites filled with silica or metal oxide nanoparticles demonstrate lower friction coefficients and enhanced wear properties as long as the nanoparticle dispersion within the polymer matrix is homogeneous [63]. Homogeneous nanoparticle dispersion in polymer nanocomposite coatings also creates a self-similar surface micro-scale roughness which can also contribute in lowering friction coefficient by minimizing solid-solid contact surface area.
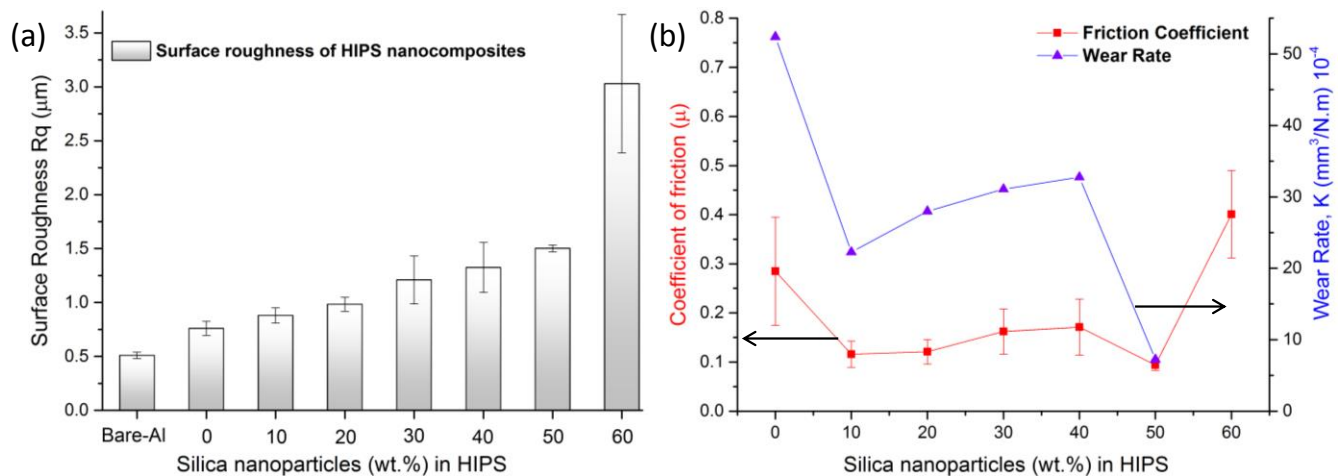
Figure 2.8. Tribological characterization results. (a) Surface roughness measurements. (b) Friction coefficient and wear rate of HIPS nanocomposites with different silica concentrations. In all cases PFAC primer layer is applied. Wear rate was calculated by equation 4.

Note that at 60 wt.% SiO_2 nanoparticle concentration in HIPS, wear rate measurements could not be performed (immediate material removal by the steel ball) due to the fact that surface roughness was increased dramatically (Figure 2.8a).

Wear track (mark) SEM images of representative nanocomposites (containing 20 wt.% and 50 wt.% SiO_2) are given in Figure 2.9. Wear is created by compression induced stresses during testing. In

the case of 20 wt.% SiO_2 concentration, for instance, the wear track (Figure 2.9a) has thin and deep cracks as well as wear debris (Figures 2.9b and 2.9c). Although, no complete material removal is present along the wear track, formation of particle-like wear debris can be attributed to a phenomenon known as fatigue wear. The fact that no crack formation, material removal or wear debris is visible in the SEM images of the 50 wt.% SiO_2 in HIPS samples (magnified images in Figure 2.9 e and f) can be attributed to the combined effects of rubbery domains in HIPS, SiO_2 nanoparticles and the primer layer in transferring and dissipating mechanical stresses [64]. It is also important to note that improvement of wear properties of polymer nanocomposites is generally better when the polymer matrix/nanoparticle interface is established either by grafting or by strong adhesion provided that a homogeneous nanoparticle dispersion is maintained [65]. According to Friedrich et al. [66], surface nanoparticles in polymer nanocomposites can dissipate wear stresses by a topographic mechanism known as smoothening and rolling effect. It is argued that this mechanism can be evoked under certain nanoparticle loadings, which strongly depends on the type of the nanoparticle as well as on the complex polymer/nanoparticle interactions [67].
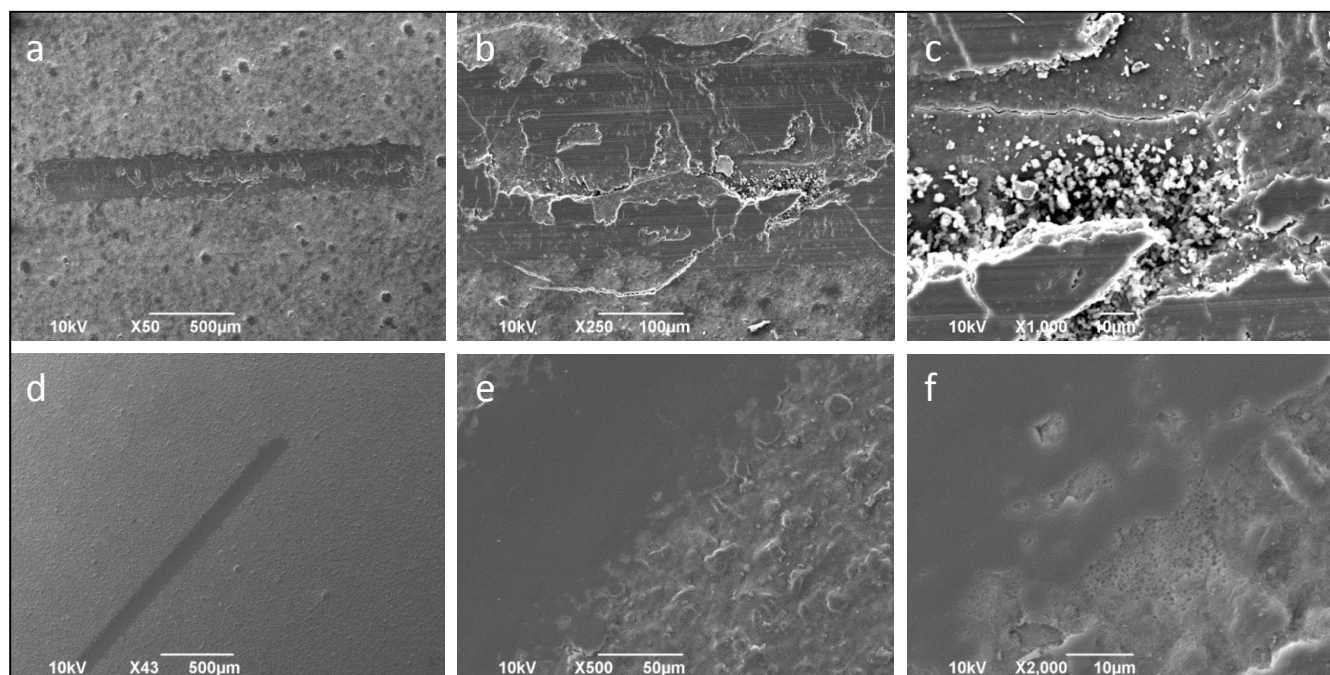
Figure 2.9. SEM images of scratched surfaces. Images of HIPS nanocomposites with 20 wt. % SiO_2 concentration presented in the order of increasing magnification. [(a), (b) and (c)] HIPS nanocomposites with 50 wt. % SiO_2 concentration [(d), (e) and (f)]. All coatings were thermally annealed applied over the primer PFAC polymer layer.

Linear abrasion of the coatings with a mild abradant material comprised of silicon carbide/aluminum oxide abrasive particles embedded in a clay binder was tested with a commercial Taber$^®$ linear abrasion instrument. Linear wear abrasion of two different samples are exemplified herein, namely 20 wt.% and 50 wt.% SiO_2/HIPS nanocomposites. Figure 2.10 shows representative surface morphology after linear abrasion experiments. In the case of 20 wt. % SiO_2/HIPS nanocomposite, formation of wear debris and flaking are visible in the ellipsoidal zones of Figures. 2.10 (a, b). In the case of 50 wt.% HIPS/SiO_2 nanocomposite, however, no significant debris formation is visible but only smoothing out of the protruding micro-bumps are visible (dashed ellipsoidal zones in Figures. 2.10(c, d)).
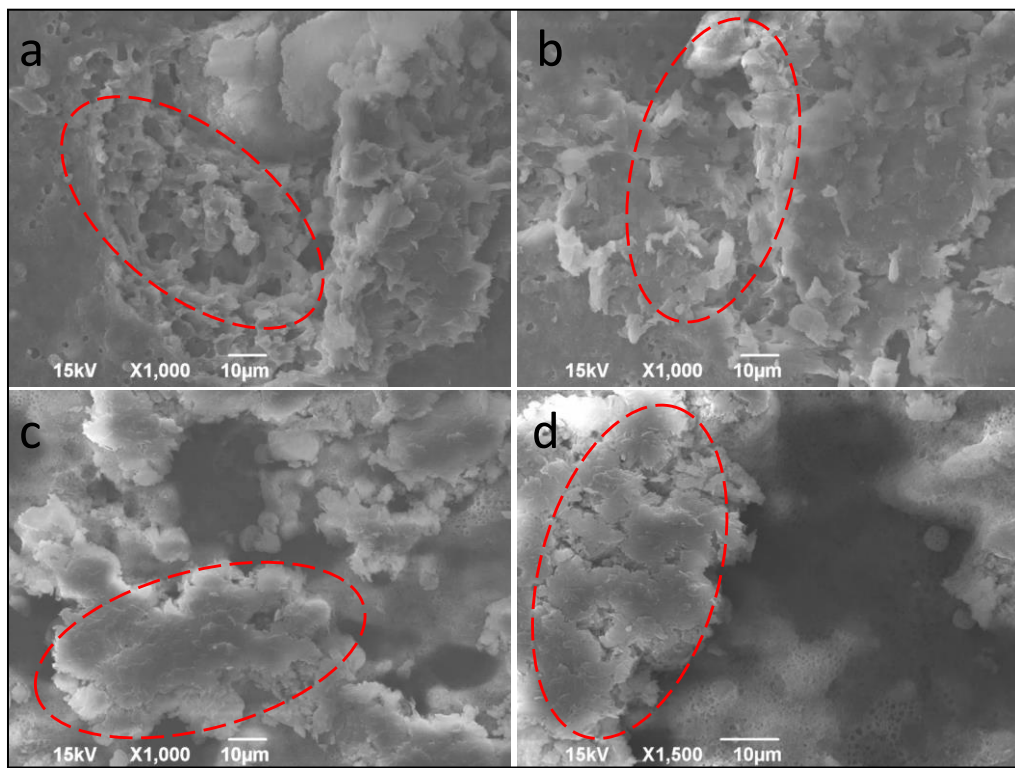
Figure 2.10. SEM images of damaged surface area after linear abrasion test (a, b) showing surface damage on the surface of HIPS nanocomposites with 20 wt.% SiO_2 concentration; whereas in (c, d), marked surfaces showing the cyclic abraded damages on HIPS nanocomposites with 50 wt.% SiO_2 concentration.

This observation confirms the conclusions of Friedrich et al.[66] that well-bound surface nanoparticle networks in certain polymer composites resist wear damage by smoothing out rather than fragmenting and cracking causing material removal.

Figure 2.11 displays changes in APCA and RA as a function of linear abrasion cycles including the effect of annealing. In the case of 20 wt.% SiO_2/HIPS nanocomposites (Figure 2.11a), APCA remained quite stable until the 20th abrasion cycle. After this, hydrophobicity of the non-annealed nanocomposites declined. The effect of annealing is noticeable as the changes in the droplet roll off angles . Non-annealed nanocomposite roll off angles increase to 90° after the 10th abrasion cycle and the droplets clear the surfaces by a very slow stick-slip sliding motion (sticky superhydrophobicity). In the case of annealing, roll off angle gradually increases to 60° at the end of the 20th cycle, a similar sticky droplet sliding behavior was observed. Tribologically stable 50 wt.% SiO_2/HIPS nanocomposites were also resilient to linear abrasion under the conditions studied (Figure 2.11b). APCA values remained above the superhydrophobicity limit all the way to the 35th cycle. However, non-annealed roll off angles increased after the 15th cycle and approaches close to 40° after the end of the experiment. Droplets would still slide off the surfaces but no rolling motion was observed. In the case of annealing, roll off angles started to increase after the 25th cycle. At the end of the 35th cycle, roll off angle values were close to 20°. Since self-cleaning superhydrophobicity is defined as superhydrophobic state with RA$<10^o$ the linear abrasion experiments were terminated after the 35th cycle.
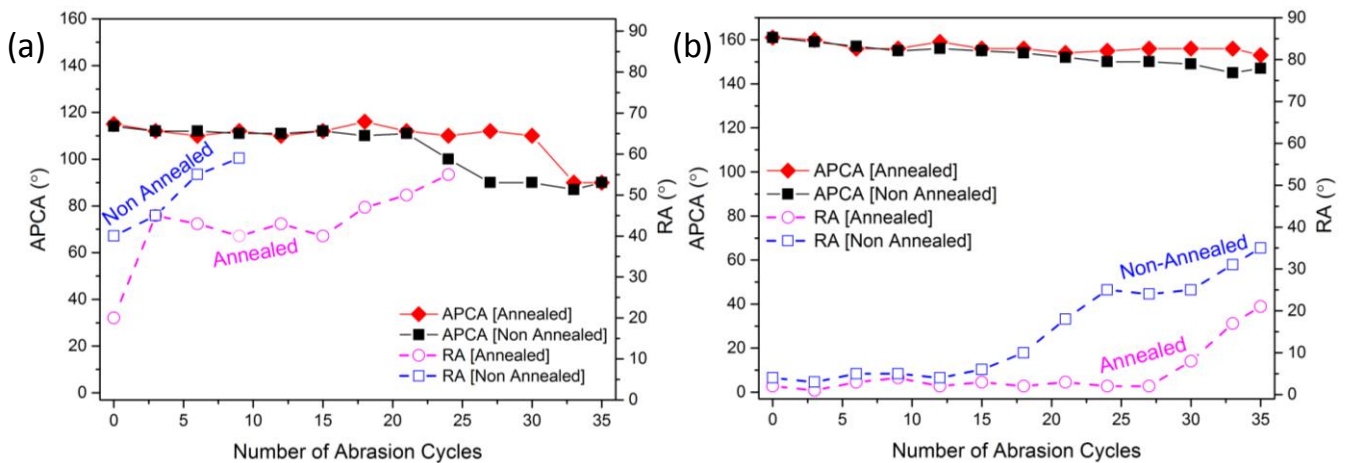
Figure 2.11. Effect of abrasion cycles on wetting characteristics of (a) HIPS nanocomposites with 20 wt.% SiO_2 concentration. (b) HIPS nanocomposites with 50 wt.% SiO_2 concentration. All coatings were thermally annealed applied over the primer PFAC polymer layer. (Note that in Figure 2.11a, no water roll off was observed after 9 and 25 abraded cycles for non-annealed and annealed specimen respectively).

Identical experiments were performed with general purpose polystyrene as matrix. Results on polystyrene/SiO_2 (50 wt.% SiO_2) nanocomposites are given in Figure 2.12. If no annealing is

performed, self-cleaning superhydrophobic properties of polystyrene/SiO$_2$ nanocomposites fail after 15 abrasion cycles. Upon annealing, static water contact angles were preserved above 150° however, still, after 15 abrasion cycles droplet roll off angles exceed 20° indicating a stick-slip non-wettable surface.
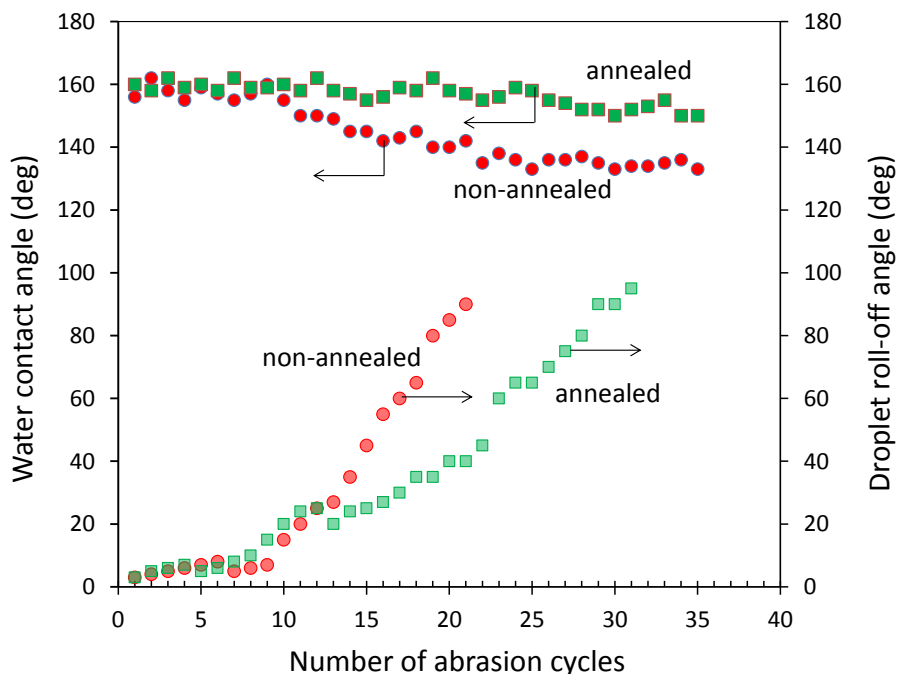
Figure 2.12. Static water droplet contact angles and water droplet roll off angles for general purpose polystyrene/SiO$_2$ nanocomposite coatings with primer PFAC as a function of Taber abrasion cycles

Surface morphology of the nanocomposites was further studied by AFM measurements as shown in Figure 2.13(a-d). AFM measurements were conducted on two different specimen, abraded and non-abraded HIPS nanocomposites (with 50 wt.% fumed silica nanoparticles). The superhydrophobic coatings appear to have dual scale hierarchical topography as can be seen in Figure 2.13a. The calculated average roughness of non-abraded specimen was 525 ± 49 nm. Surface roughness was further analyzed by the water-shed grain analysis algorithm with different roughness areas marked as segments of different colors, shown in Figure 2.13b, clearly indicating many segments of different roughness profiles. Topography of the abraded surface was then analyzed (shown in Figure 2.13c). Abraded AFM image appears to have more smooth surface structure with low roughness calculated as 348 ± 31 nm, confirmed by the grain water shedding analysis (shown in Figure 2.13d). Energy Dispersion X-ray Spectroscopy (EDX) was performed on aforementioned samples to confirm the silica distribution in abraded and non-abraded specimen. EDX mapping of silica distribution in non-abraded surface is shown in inset of SEM image in green points whereas red color mapping signals are

indicating the distribution of silica after abrasion. Results indicate that there was a minimal reduction of approximately 8 % in silica content after abrasion shown in Figure 2.13e (lower layer).

Surface roughness of the superhydrophobic HIPS composites was reduced after abrasion but maintained the dual hierarchical order to ensure that Cassie-Baxter state remains same after some surface features are worn away. After abrasion, microscale bumps in combination with hydrophobic fumed silica prevented from introduction of hydrophilic pinning sites. The reported roughness after abrasion is sufficient for maintaining its water repellency, although it effected the water roll off efficiency which was increased from 2° to 20° after 35 abrasion cycles. Such a roughness profile is sufficient to create the self-cleaning ''lotus effect'' [68] when combined with a uniformly formed hydrophobic surface chemistry shown in Figure 2.13e.
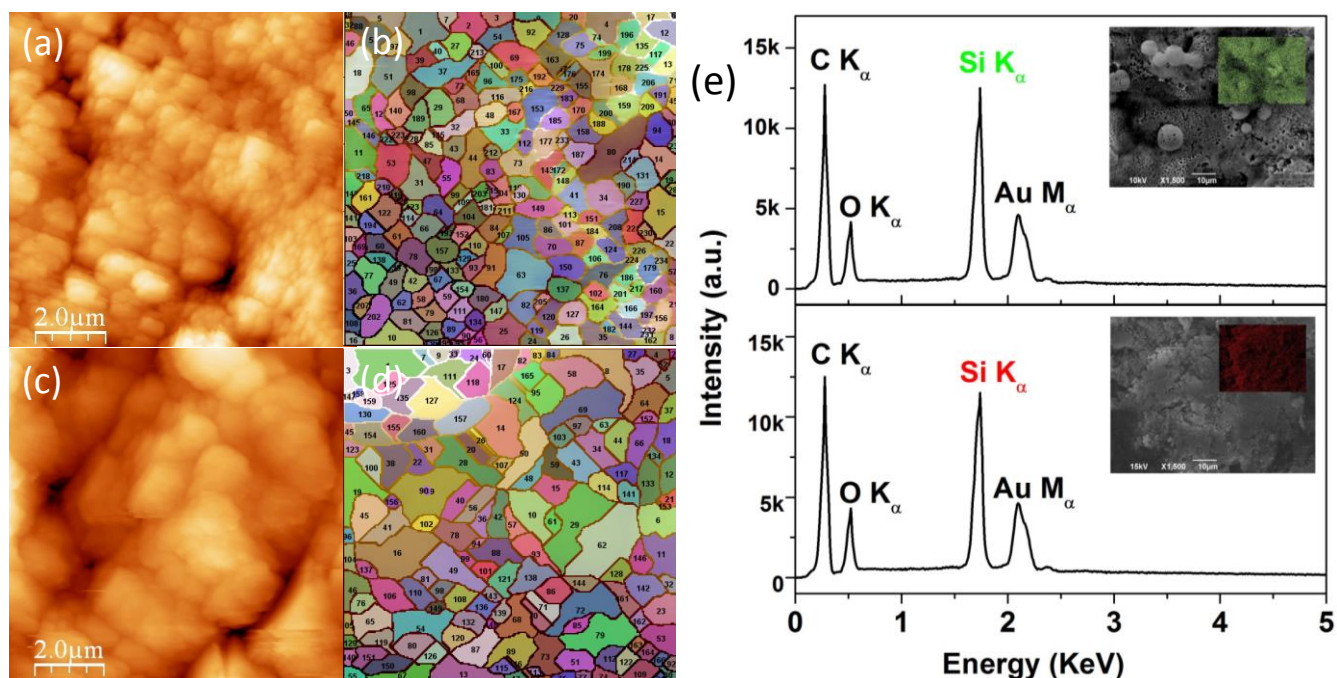
Figure 2.13. AFM topology images. (a) Non-abraded HIPS nanocomposites with 50 wt.% SiO_2 showing natural textured surface. (b) Water grain analysis algorithm of non-abraded structure, each segment indicates an individual roughness area and height (roughness volume). (c) HIPS nanocomposites after abrasion with 50 wt.% SiO_2. (d) Roughness segments of abraded surface generated by water grain analysis algorithm for abraded surface (e) EDX analysis of non-abraded and abraded surfaces respectively. Representative SEM images and EDX mapping are given as insets with indication of silicone as green and red maps. All HIPS specimen used herein are thermally annealed and applied over PFAC primer layer applied over PFAC primer layer.

2.4 Conclusions

In conclusion, we demonstrated a simple fabrication process for superhydrophobic and wear abrasion resistant high impact polystyrene (HIPS) / silica nanocomposite coatings for metal surfaces. All coatings can be made by spray. An environmentally friendly perfluorinated acrylic polymer primer coating layer was needed to increase the adhesion to the metal substrate and therefore withstand abrasion resistance. The best nanocomposite composition was found to be 50 wt.% SiO_2 nanoparticles with respect to HIPS. This coating had the lowest friction coefficient compared to other nanocomposites tested. Tribological measurements on the best performing nanocomposites indicated that wear tracks or marks had no debris, cracks or complete material removal. Additionally, Taber[®] abrasion tests under 15 kPa load confirmed tribological findings and the best nanocomposites resisted superhydrophobic degradation up to 35 continuous linear abrasion cycles. Nanocomposites made with general purpose polystyrene instead of HIPS could resist only 15 Taber[®] abrasion cycles. The reason was attributed to the mechanical energy dissipation capability of rubber domains in HIPS. Thermal annealing of the coatings significantly enhanced the durability of the coatings against tribological wear towards long-lasting self-cleaning superhydrophobicity. Low-cost and non-toxic ingredients with industrial scale production ensure that these non-wettable coatings can be easily applied over large scale metal surfaces as protective waterproof treatments.

3. Enhancement in the tribological response of non-porous nylon 66 based polymeric nanocomposites

3.1 Introduction

Solvent-suspended particles are widely used in lubrication but their applications are limited and hindered by incompatible substrate, unadapt environment, danger of contamination[69,70,71] . Indeed, the elimination of harmful solvents is one of the objectives of Green Tribology, a growing field within the broader one of Green Chemistry, dedicated specifically to reduce the environmental impact of tribological systems [72]. Alternative to such limitations is polymeric nanocomposite coatings, a class of the family of solid lubricants, primarily important for controlling friction and wear where operating conditions become severe and traditional fluid lubricants can never be used, or the formation of hard debris must be avoided in tribological applications[54]. The use of solid lubricant polymers and polymeric nanocomposites is growing in the field of tribology such as gears, bearings, seals, vacuum pumps, prosthesis and implants in medical applications etc. [73,74]. Significance of solid lubricants lies where good resistance to sliding contacts, strong adhesion to the underlying substrate and surface coverage is involved. For instance, with coatings as paints and varnishes[75], in microelectronic systems[76] or machine parts [77], etc.

Among polymers, aliphatic polyamides are extensively used as sliding parts in automotive parts, food packaging, bearings and engineering prodcts[78,79,80]. Nylon 66 is an aliphatic polyamide, used in industry since decades due to its excellent physio-chemical properties, such as high melting point, low permeability, low melting viscosity, ductility, heat resistance, etc.[81]. Despite the good mechanical and tribological properties of polyamides[82], one of the limitations is its poor adhesion to the substrates due to low surface energy and weak mechanical interlock mechanism[83]. Substrate-coating adhesion can be achieved by either mechanical adhesion (substrate roughness, mechanical interlocking) or by the, albeit weak, contribution of molecular bonding that includes electrostatic and Van der Walls forces or H-bond interactions. Conventionally, mechanical interlocking is achieved by abrading the substrate, allowing the coatings to fill pores, hovels, crevices and micro voids created by the abrasion. On the other hand, mechanical abrasion or sandblasting have limitations of operator sensitivity and are difficult to perform on small parts. Wet chemical etching is another technique used to create roughness on a substrate, but its overtreatment can damage parts and has serious hazards and disposal issues. Corona treatment is used for oxidizing the surfaces, however its transient nature and limited polymer choice restricts the applications. In addition, plasma surface treatment is widely used for substrate

pretreatment providing removal of surface contaminants, enhances the wettability and helps in the formation of functional groups, nonetheless it has very costly setup and has restriction of batch-to-batch logistics. A novel and possible approach to the improvement of adhesion is based on the addition of different fillers, exploiting their stronger interaction with the substrate or the improved formation of anchor points for mechanical interlocking[84,85].

Yet the main purpose of fillers is to improve the mechanical properties of polymeric materials, and, among them, their tribological response. The most conventional fillers to reduce friction and wear include hard ceramics such as alumina, polytetrafluoroethylene (PTFE), molybdenum-disulfide (MoS_2) and carbon based materials, often prepared in nanometric size[86,87]. However, these fillers have some limitations, for instance PTFE is well-known for low friction, but has poor wear resistance[88], MoS_2 performs poorly in the presence of humidity[89,90] and graphite has restriction of operating in dry or vacuum environment[91]. Compared to such conventional fillers, graphene has gained great attention in recent years because of its exceptional electrical[92], mechanical, thermal, structural properties and has already shown promising results in tribology as a lubricant additive[93]. As an additive, graphene can have a strong effect on the mechanical properties of a composite material, owing to its high strength (~130 GPa) and elastic modulus (0.5-1 TPa)[94,95]. Graphene has been employed as a filler for different polymers, among which Lahiri et al. incorporated graphene nanoplatelets (GNPs) as a reinforcement element in ultrahigh molecular weight polyethylene to improve its fracture toughness and tensile strength[96], Xu et al. reported the enhancement of tensile strength and Young's modulus by the in situ polymerization of graphene nylon 6 polymer[97], Cataldi et al. studied the improvement in modulus of stiff and soft polymers by the addition of graphene with different thermal treatments[98]. Apart from effect on bulk properties of a composite material, graphene has unique characteristics of interfacial interaction with different substrates, such as silica, copper and nickel[99,100].

Despite the physical properties that make graphene a promising candidate as a solid lubricant or as an additive, such as its bidimensional structure, high surface energy and low permeability to gases[101], its use in the field of tribology is relatively unexplored. Graphene nanoplatelets have been proposed as a thin solid lubricant[102,103] and have shown high wear resistance especially at nanoscale[104,105], but only in few works its performance in macroscopic solid materials has been investigated[106,107]. Notably, Kandanur et al. reduced the wear rate of PTFE by addition of 10 wt.% graphene platelets[108]. A limiting factor to the widespread use of graphene as a tribological material is

its friction coefficient (0.1-0.2)[109] which is still higher than that of the best performing materials, such as PTFE ($<$ 0.05).

Aim of this work is to study the polymeric composites containing GNPs as a solid lubricants. Nylon 66 was chosen as the polymer matrix for owing its wide spread usage in industry and due to the reason that it has good mechanical and tribological properties. Processing of nylon 66 is usually done by extrusion or hydraulic press to form bulk specimen. Solvents required to cast the nylon 66 films are usually formic and hydrochloric acids or cresol[110,111] resulting in porous membrane with relatively poor mechanical properties, unsuitable for use where tough mechanical parts are needed. To produce non-porous dense films, a new solvent based method was developed[112]. Interestingly the nylon 66 films produced by trifluoroacetic acid (TFA) solvents resulted in good mechanical properties as compared to porous nylon 66 films. Herein, by following this novel route of preparing non-porous nylon 66 coatings, a study is conducted by incorporating PTFE and graphene nanoplatelets (GNPs) for tribology application. The GNPs/nylon66/PTFE composites show strong adhesion and a three-fold reduction in friction and wear rate, compared to the pure nylon 66. The best performance was obtained for an amount of GNPs of 0.5% in weight.

3.2 Materials and Methods

Nylon 66, polyamide (PA)66, was purchased from Sigma-Aldrich with molecular weight of MW=120,000. Degree of polymerization DP was around 531 with density of 1.14 g/mL. Grade Pure G+ Graphene nanoplatelets (GNPs), with lateral dimension of a few micrometres and a thickness of a few nanometers[113], were kindly provided by Directa Plus (Lomazzo (CO) − Italy). Polytetrafluoroethylene (PTFE) with nominal particle size of ˷ 1μm, aluminum oxide nanoparticles with nominal particle size of 13nm and Ethyl Cyanoacrylate (Permabond 105) were purchased from Sigma-Aldrich.

Reagent grade solvent trifluoroacetic acid (TFA), dimethyl sulfoxide (DMSO) and acetone were purchased from Sigma-Aldrich and used as received.

3.2.1 Sample preparation

Composite coatings of nylon 66 were prepared using different GNPs concentrations while keeping constant the concentration of PTFE with respect to the nylon 66. The preparation of the nylon 66 is described in detail in Ref. [112]. Briefly, nylon 66 was first dissolved in solution of TFA and acetone with

1:1 volume ratio to obtain 7 wt.% polymer in solution. After the nylon 66 pellets were completely dissolved, PTFE was added to the solution at concentration ratio of 5 wt.% with respect to nylon 66. GNPs were then added at different weight fractions, ranging from 0 wt.% to 3 wt.% with respect to nylon 66. Solutions were bath sonicated at 40 Hz for 3 hours and at 59 Hz after 24 h to get homogeneous dispersion of both PTFE particles and GNPs. The choice to include PTFE in all composites was taken after screening tests (not reported) showed significantly higher friction when it was not added. A complete schematic for the preparation of non-porous nylon 66 composite films is explained in Figure 3.1.

Glass substrates were cut to a rectangular shape, cleaned with acetone and bath sonicated for 60 minutes for the removal of residues. A simple dip coating method was used for the deposition: the substrates were dipped in the solution for 10-15 seconds and left in fume hood for the solvent to evaporate. All the samples prepared and their labels are presented in Table 3.1.

Table 3.1: Labels and PTFE and GNPs concentration of the prepared samples

	Concentration (Nylon66 to 100%)	
Sample label	PTFE wt.%	GNPs wt.%
P0G0	0	0
P5G0	5	0
P5G0.1	5	0.1
P5G0.2	5	0.2
P5G0.3	5	0.3
P5G0.4	5	0.4
P5G0.5	5	0.5
P5G1	5	1.0
P5G2	5	2.0
P5G3	5	3.0

Additional samples were fabricated with the same technique substituting GNPs with alumina nanoparticles, as a reference for the tribological tests. Samples of Ethyl Cyanoacrylate (ECA) were also deposited with the same technique starting from a solution of dimethyl sulfoxide (DMSO) and acetone, as a reference for the adhesion tests.
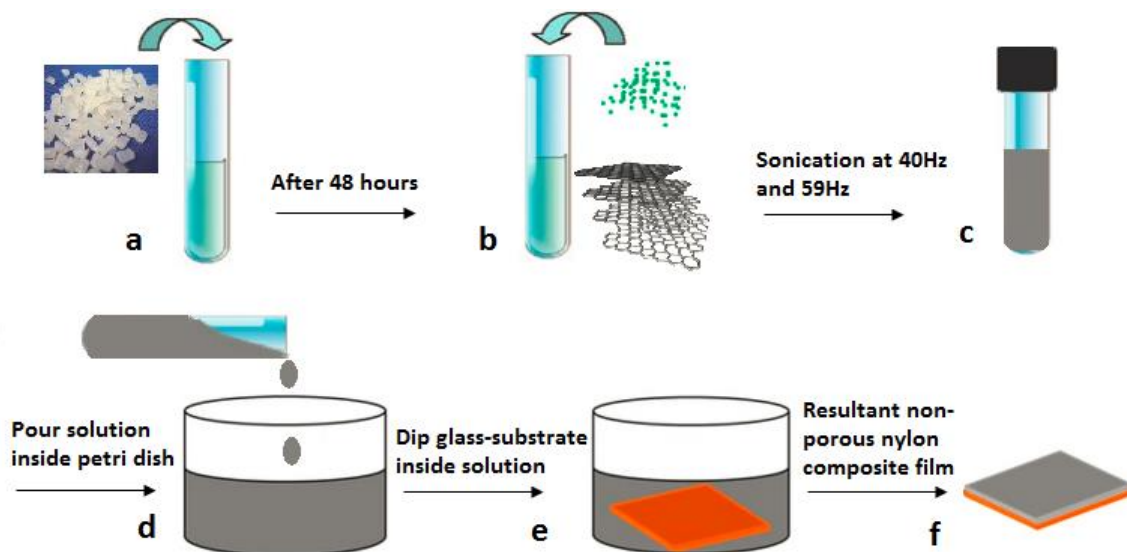
Figure 3.1. (a) Add porous nylon 66 pellets inside TFA, Acetone solvents (b) Add PTFE and GNPs inside non-porous nylon 66 solution (c) Sonicate at 40Hz for 3 hours and then at 59Hz for 1 hour (d) Pour composite solution inside petri dish (e) Dip glass substrate inside petri (f) Solid lubricant non porous nylon 66 composite film

3.2.2 Morphological characterization

The morphology of the films was studied by Optical Microscopy (Leica DM 2500M) and Scanning Electron Microscopy (SEM, JEOL JSM-6490AL operating at 10kV and JEOL JSM 7500FA operating at 5 kV). Films were sputtered with a thin layer of gold or graphite before observation to improve conductivity.

Grazing Incidence X-ray Diffraction (GIXRD) analysis was performed on a Rigaku Smartlab equipped with a 9 kW CuKα rotating anode, operating at 40 kV and 150 mA. A Göbel mirror was used to convert the divergent X-ray beam into a parallel beam and to suppress the Cu Kβ radiation, while a 0.5° Parallel Slit Analyzer was employed in the receiving optics. The diffraction patterns were collected with a fixed grazing incidence angle ω of 3° and over a 2θ angular range from 7° to 60°, with a step size of 0.05°. The specimens were placed on a zero-diffraction quartz substrate and measured at room temperature. GIXRD data analysis was carried out with the PDXL 2.1 software from Rigaku.

3.2.3 Mechanical characterization

The Young's modulus and hardness of the samples were characterized by nanoindentation on an Anton Paar UNHT equipped with a diamond Berkovich tip. Maximum load was 1 mN, loading and unloading time 30 s, with a dwell time at maximum load of 30 s to allow viscous relaxation. Young's modulus E and hardness H were calculated from the unloading curves with the Oliver & Pharr method. At least 10 repetitions were conducted for each material, and results are presented as average value and standard deviation.

3.2.4 Tribological characterization

Multi-pass scratch tests were performed on a Micro-combi tester (Anton Paar Gmbh, Germany), to evaluate friction and wear resistance. A bearing steel ball of 500 µm radius was used as a counterpart for rubbing. The tip displacement rate was 10 mm/min for a reciprocating distance of 4 mm, corresponding to a frequency f= 0.042 Hz, under the constant load of 1 N, corresponding to a Hertzian pressure $p \sim 90\ MPa$, for 75 cycles, corresponding to 30 minutes. All the friction and wear tests were carried out at laboratory conditions (21±1°C, 50±5%RH).

The average values of steady coefficient of friction, following the running-in phase, were extracted from the experimental data plots of friction coefficient. A typical friction trace is reported in Figure 3.2. All the data here are the average of five replicate measurements for each material.
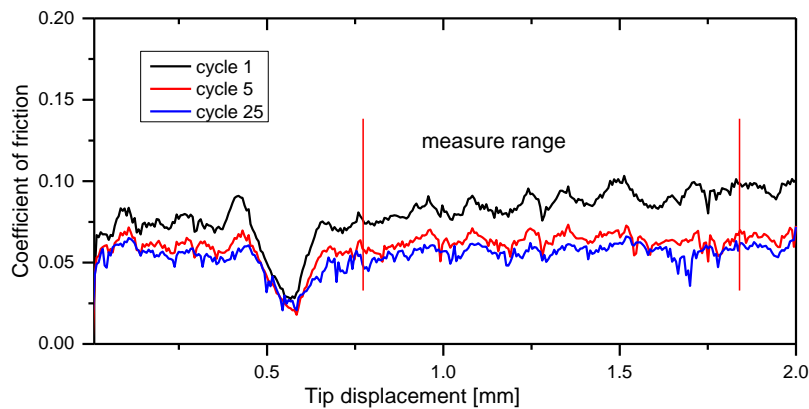
Figure 3.2. friction trace for selected cycles of P5G0.5 sample. Friction is averaged from the signal within a chosen range to avoid artifacts caused by surface features, indicated between the red lines.

After each test, the depth of the wear scar d was measured using a stylus surface profiler (DektakXT, Bruker). Each scar was measured 5 times and the average was calculated. The wear volume, ΔV, of the specimen was calculated from geometrical considerations, with Equation (1):

$$\Delta V = \frac{L}{2} \, r^2 \left(\cos^{-1}\left(\frac{r-d}{r}\right) - \frac{\sqrt{r^2-d^2}}{r} \right) \qquad (1)$$

where L is the length of the stroke in one cycle and r is the radius of the counterpart steel ball. The wear rate was calculated by the ASTM G-99 standard wear rate formula:

$$K = \frac{\Delta V}{F \times N \times L} \qquad (2)$$

where F is the applied load (N), L the stroke length in one cycle (m) and N represents the total number of cycles, so that NL is the total sliding length[34].

Moreover, the adhesion of coatings deposited on the glass substrates was evaluated by a progressive scratch test, during which the load was increased linearly from 0.03 (Hertzian pressure $p{\sim}60\ MPa$) to 10 N ($p{\sim}190\ MPa$) over a scratch length of 2 mm, with a sliding rate of 1 mm/min and acquisition rate of 30Hz. After each test, optical images were acquired to examine the damage mechanisms and to evaluate the failure critical load, corresponding to the load at which the glass substrate is exposed. In order to evaluate the significance of the measured values, additional tests were performed on Ethyl Cyanoacrylate (ECA). Such polymer is specifically designed as an instant adhesive, it was therefore taken as a positive control.

3.2.5 Chemical characterization

µRaman spectra were collected at ambient conditions using a Horiba Jobin Yvon LabRAM HR800 spectrometer, equipped with a microscope. A 632.8 nm excitation line, in backscattering geometry through a 50× objective lens, was used to excite the specimens, at the low power of ~0.25 mW. The experimental set-up consists of a grating 600 lines/mm with spectral resolution of approximately 1 cm^{-1}. Raman spectra were collected from the pristine surface, as well as from the scratch, after the wear test and from the steel ball used as rubbing counterpart.

3.3 Results and discussion

3.3.1 Films morphology and structure

Uniform composite films were obtained through the dipping method, with thickness varying among samples between 10 and 20 µm. Roughness of the films was measured on a stylus optical profiler (DektakXT, Bruker), yielding values in the range of 765-780nm. Figure 3.3(a-d) shows the optical

images of the surface of selected samples. The nylon 66 matrix appears dense and non-porous. GNPs are clearly visible in loaded samples, owing in part to the transparency of nylon 66 to visible light.
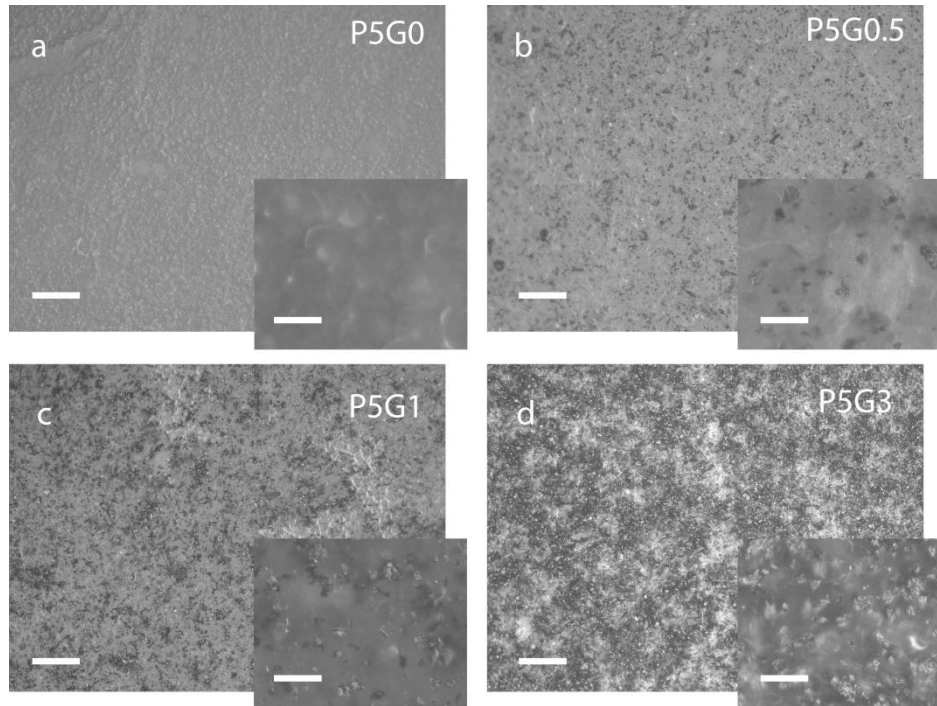
Figure 3.3. Optical images of the studied nanocomposites: a) P5G0, b) P5G0.5, c) P5G1, d) P5G3. Higher magnification is shown for each material in the inset. Scale bars are 50 μm in the main images, 10 μm in the insets.

GNPs distribution is fairly homogeneous in all samples, with tendency towards slightly larger clusters as the GNPs concentration is increased. These observation were confirmed by SEM images on selected samples, reported in Figure 3.4(a-b). As the amount of GNPs is increased, nanoplatelets tend to form slightly large clusters. PTFE particles can also be seen in both samples.
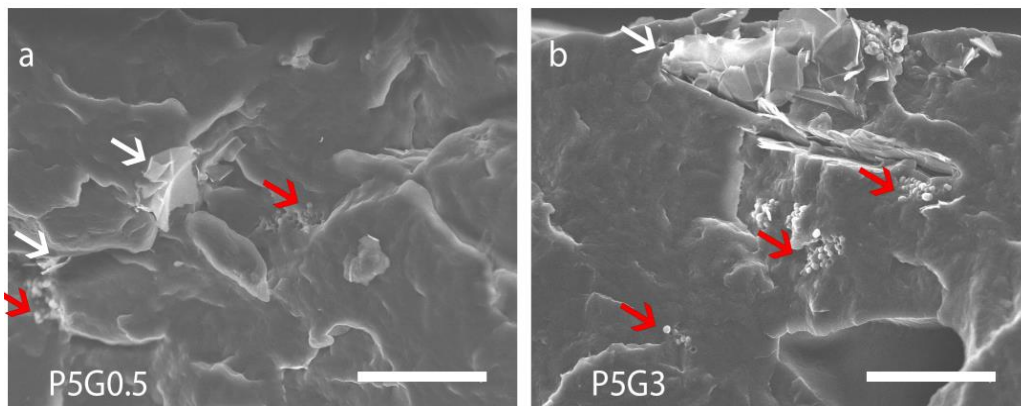
Figure 3.4. SEM cross-sections of selected samples, scale bars 50 μm: a) P5G0.5 and b) P5G3; GNPs are indicated by white arrows, PTFE microparticles by red arrows. . A relatively large GNPs cluster is visible at the surface of P5G3

X-ray diffraction spectra were acquired on selected samples and are shown in Figure 3.5a. The main peaks are ascribed to the triclinic α phase of nylon 66, at 20°, corresponding to the (100) plane, and at 24°, corresponding to the (010)/(110) doublet. Morphology-wise, the former is associated with the intra-sheet, the latter to inter-sheet diffraction. A broad amorphous halo is also evident, centered at around $22°^{114}$. Considering the intensities of the crystalline peaks and the amorphous halo, no appreciable differences in the crystallinity are evident. On the other hand, the ratio between the (100) and the (010)/(110) peaks, shown in Figure 3.5b, is slightly modified for GNPs concentration larger than 0.5%, going from 0.76 (P5G0 and P5G0.5 samples) to 0.52 (P5G1) and to 0.48 (P5G3). Such phenomenon was observed already, and is associated to the GNPs intervening in the crystallization from solution, with the effect of weakening the intrasheet bonding between crystalline sheets [112]. Interestingly, the addition of a small amount of graphene, up to 0.5 wt.%, does not modify the ratio, suggesting that the platelets thickness is low enough to not affect the structure, i.e. dispersion is good and aggregation minimal.
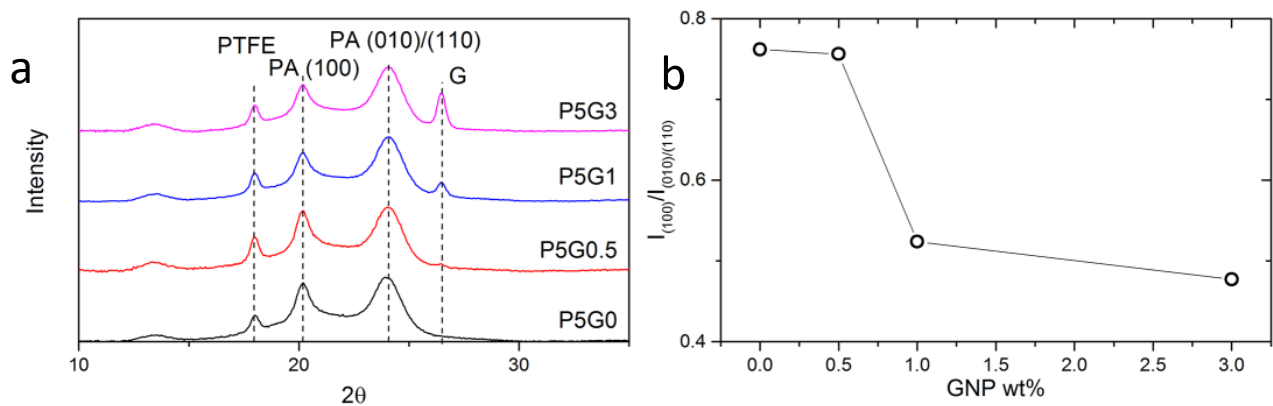
Figure 3.5. a) GIXRD spectra on P5G0, P5G0.5, P5G1 and P5G3 samples; b) evolution of the $I_{(100)}/I_{(010)/(110)}$ peaks ratio as a function of graphene content.

3.3.2 Mechanical and tribological properties

Nanoindentation results are shown in Figure 3.6a. Young's modulus is weakly affected by variations in GNPs concentration. The only value significantly higher than the rest is that of P5G0.5 samples ($p<0.01$ as calculated through ANOVA). Such increment is in line with our previous findings in a similar system[98] and suggests good dispersion of the fillers as compared to the other compositions.

Interestingly, hardness increases only slightly and with little statistical significance as the GNPs concentration is augmented. Overall, the mechanical properties can be considered weakly affected by the composition, therefore any variation observed in the tribological response cannot be explained only as a consequence of such properties.

The friction coefficient and wear rate of the materials as a function of GNPs concentration are presented in Figures 3.6b and 3.6c, respectively. It can be observed that the pure PA66 film has a coefficient of friction of ca. 0.19, whereas addition of PTFE fillers results in a significant reduction of the friction coefficient to ca. 0.12. The addition of GNPs results in a further decrease of the coefficient of friction: increasing the GNPs concentration from 0.1%-0.5% results in a large decrease in coefficient of friction, with the lowest value, 0.06, obtained for the P5G0.5 samples. As the GNPs concentration increases further, from 1.0% to 3.0%, the beneficial effect of the GNPs is reduced, and the values of the friction coefficient increase up to ca. 0.13. The specific effect of GNPs in combination with PTFE can be better appreciated if compared with similar composite coatings in which GNP is replaced with another effective low-friction additive, such as aluminium oxide. Direct comparison, reported in Figure 3.7a, shows values of friction in the same order, but not as low as our best results, obtained with GNPs.
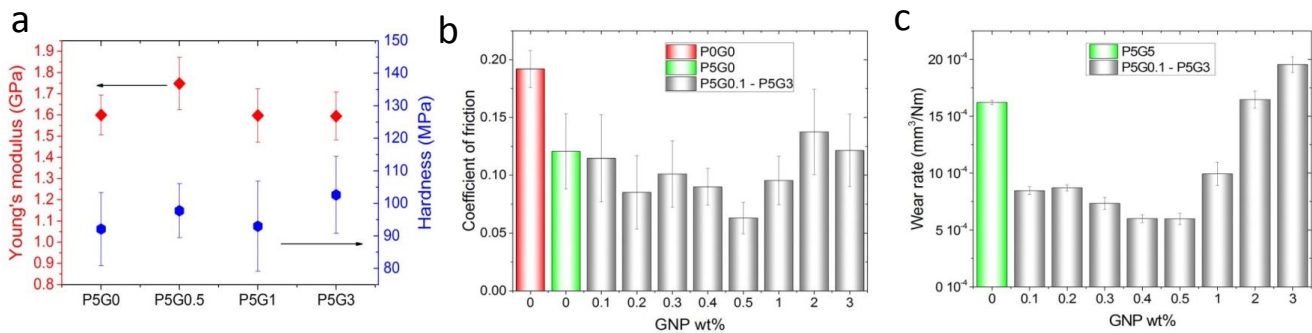
Figure 3.6. (a) Mechanical properties, (b) coefficient of friction and (c) wear rate of nylon/PTFE composite at different GNPs concentrations

A similar behavior can be seen in the wear rate measurements: the increment of the GNPs concentration improves the wear resistance, which exhibits a minimum at 0.5% GNPs concentration. As shown in Figure 3.6c, the wear rate drops from 16.21×10^{-4} mm^3/Nm for the P5G0 sample, down to 5.98×10^{-4} mm^3/Nm for the P5G0.5 sample. Similar to the friction coefficient case, our results compare favorably to those obtained on materials reinforced with aluminum oxide (Figure 3.7b). It is worth noting that it was not possible to measure wear rate of the pure nylon film due to its poor adhesion with

the glass substrate. It was however possible to obtain reliable values of the friction coefficient, which is a less stressful test for the material, only by attaching the films to the substrate with thin double side tape.
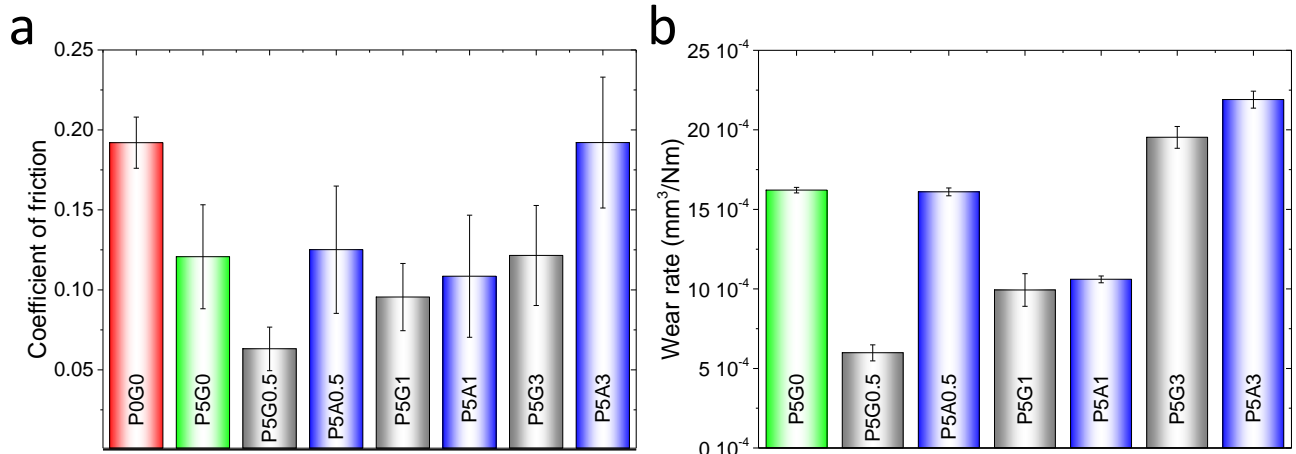
Figure 3.7. Comparison of the Coefficient of friction and wear rate of selected samples, with equivalent samples prepared with Al_2O_3 (nominal size 13 nm) instead of GNPs, as in Table S1

Figures 3.8(a-c) show the SEM images of the scratched surface of the P5G0, P5G0.5 and P5G3 samples. All present fairly smooth surfaces, which suggests that the wear mechanism is the adiabatic formation of a transfer film, typical for semi-crystalline polymers. Only the P5G3 sample presents few debris at the sliding path edges. P5G0, on the other hand, exhibits numerous longitudinal cracks (Figure 3.8a), probably due to plastic deformation which nucleates below the contact area[115] and, when the stress imposed by the steel ball is released, maintains the deformation, so that a tensile stress is generated on the layer of material above, deformed elastically, leading to fracture. In the presence of GNPs, damage has the form of transverse, rather than longitudinal, cracks, with just a few occurrences in the P5G0.5 samples (Figure 3.8b) and a larger number in the P5G3 samples (Figure 3.8c). Transverse cracks are attributed to decohesion at the Nylon 66/GNPs interface, which is typical in composites based on layered nanofillers[116] and leads to the formation of debris in the case of P5G3 samples.
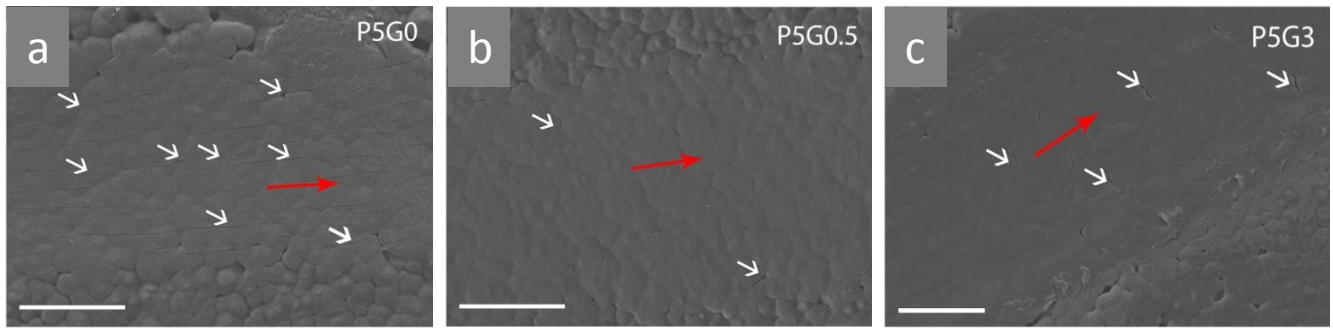
Figure 3.8. (a-c) SEM images scratched surfaces from selected samples, scale bars are 50 μm, red arrows indicate the testing direction: in P5G0 (a) arrows indicate longitudinal cracks; in P5G0.5 (b) only a few transverse cracks are visible, whereas in P5G3 (c) they are more frequent.

The improvement can be attributed to the formation of a transfer film between the coating and the rubbing counterpart: a thin layer of material is transferred to the steel ball, and spread along the scratching area, so the low-friction material is present in both sliding surfaces. PTFE is, indeed, well known for creating a transfer film upon sliding contacts, which reduces substantially the friction of material[117]. On the other hand, the presence of a transfer film by itself does not guarantee low wear rate as well: PTFE, with its poor performance when used as a bulk material, well exemplifies this counterintuitive behavior, while the addition of fillers, especially alumina, improves this aspect by several orders of magnitude[118,119].

In PTFE, fillers bear part of the load and arrest crack propagation and hinder large-scale fragmentation, so that material removal is lower, and in some cases induce chemical bonding of the formed film to the sliding surfaces[120].
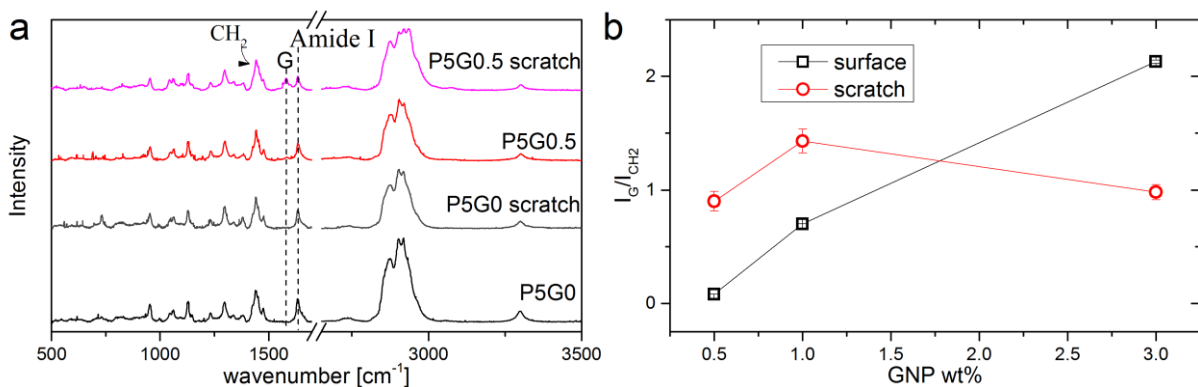
Figure 3.9. a) Raman spectra of P5G0 and P5G0.5 samples, on pristine and scratched surfaces; b) I_G/I_{CH3} peaks ratio as a function of graphene concentration, on pristine and scratched surfaces

In order to highlight the mechanisms of formation of transfer films and possible chemical interactions, Raman studies were performed on the pristine surface of the samples, as well as on the scratch formed on the surface after the wear test. In Figure 3.9a the Raman spectra of the P5G0 and P5G0.5 films are shown. The spectra taken from the pristine surface are those typical of the nylon 66 spectra prepared with the TFA-acetone solvent[112]. Briefly, the peak at 1636 cm^{-1} is assigned to the amide I group, while the peak at 1296 cm^{-1} is assigned to CH$_2$ twisting mode, the peak at 1445 cm^{-1} and the band centered at approximately 2908 cm^{-1} are assigned to CH$_2$ bending and stretching modes, respectively. Finally, the N–H stretching of the amide A is observed at 3300 cm^{-1}. In the same figure, the Raman spectra of the nylon 66/graphene samples is depicted for the 0.5% graphene concentration, where the G peak of graphene is located at 1580 cm^{-1}. Increasing the graphene concentration results in a higher intensity of G peak and the appearance of the other characteristic peaks of graphene, such as the D peak (~1345 cm^{-1}) and the 2D peak (~2700 cm^{-1}) (spectra not shown here). The intensities of the G peak, normalized by the intensity of methylene twisting peak at 1445 cm^{-1}, are shown for the pristine surface and the scratch in Figure 3.9b. As expected, the normalized G peak increases with increasing graphene concentration for the pristine surface. Considering the spectrum acquired on the steel counterpart, the formation of a transfer film is confirmed by the presence of graphene.

From the spectra acquired on the scratched lines, Fig. 3.9b, no chemical interactions of GNPs with either PTFE or the nylon 66 matrix are visible; we attribute to the high surface energy of GNPs the improvement of the physical adhesion to both surfaces, while their bidimensional structure facilitates plains sliding, much like the effect of well-disperse modified nanoclay added to nylon 6[116]. On the other hand, the variation of the G peak as a function of GNPs concentration suggests that the formation of a graphene transfer film does not follow the same behavior in all composites: the amount of graphene on the scratch imprint is higher than that on the untested surface in the case of low graphene concentration, up to 0.5 wt. %, and is lower for concentration of 1.0 wt. % and above, as shown in Figure 3.9b. In the former case GNPs are exposed during the first sliding cycles until a robust film is formed. In the latter case, instead, we attribute the lower amount of GNPs to low distance in between neighboring GNPs, so that the elastic mismatch with the matrix leads to mechanical removal of small platelet clusters which can induce third-body abrasion on the soft polymer, as shown by Khedkar et al.[118]. A similar influence of the platelets size, in a broader range of size, can be seen comparing graphene and graphite as fillers: the difference in wear rate can be as high as an order of magnitude, for a given concentration[108]. The fact that the Young's modulus is not increased with the

GNPs content confirms, indeed, that the dispersion is not optimal beyond a threshold value. A scheme of this mechanism for the formation of transfer film and its dependency on the amount of GNPs is shown in Figure 3.10.
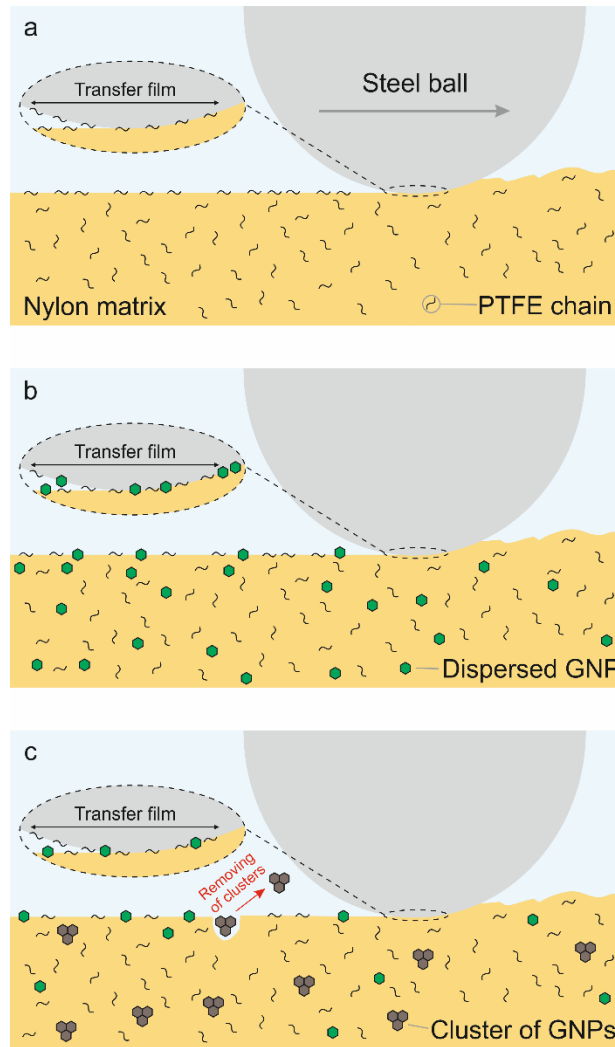
Figure 3.10. Proposed mechanism of transfer film formation for different GNPs loading: in (a) in the absence of GNPs, PTFE forms a transfer film with low friction but poor wear resistance; (b) with the addition of 0.3-0.5wt. % GNPs, the transfer film is continuous and reduces dramatically the wear rate; (c) larger amounts of GNPs induce the formation of clusters, which are removed by the sliding ball, hindering the formation of an effective transfer film.

This mechanism is compatible with the observations of the scratched areas (Fig. 3.8a-c): in the absence of graphene the visible longitudinal cracks indicate plastic deformation below the surface, similar to ductile plowing. The addition of graphene by reducing the friction hinders the tip penetration, so that overall damage is lower and consists only of few cracks, in locations probably weaker from the production process.

The role of PTFE in enhancing the tribological response of the material is quantitatively more difficult to define, as its presence was not detectable by Raman spectroscopy. Phenomenologically, its presence together with graphene reduces the friction coefficient to lower values than those of composites with the same amount of GNPs but without PTFE. It is thought, therefore, that the presence of GNPs has the dual effect of participating in the formation of the low-friction transfer film and of reinforcing the PTFE, thus reducing the wear rate, due to its rigidity and strength.

Overall, this mechanism is supported by the running-in evolution of friction coefficient: in the absence of graphene (sample P5G0), after a few cycles at low friction (≈0.09) a progressive increment indicates the removal of the transfer film; for low amounts of graphene (P5G0.5 and P5G1) friction decreases rapidly and remains stable, whereas for higher amount (P5G3), friction does not show a reduction as large.

3.3.3 Adhesion

To evaluate the adhesion between the composite films and the glass substrate, progressive scratch tests were performed on films deposited on glass slides. The critical load for failure was then optically defined using the built-in microscope and the results are presented in Figure 3.11a. The choice of glass as a substrate was dictated by the experimental need to univocally identify the onset of damage, which would be unreliable on metallic materials. Although extrapolation of our results would be speculative, the improvement granted by GNPs can be evaluated considering its intrinsic adhesion force: few-layers graphene has been shown both experimentally[121] and theoretically[99] that its adhesion to silica and copper is similar, which suggests that the adhesion improvement from graphene as a filler might be generalized. As expected, the pure nylon 66 films (P0G0 samples) did not adhere on the glass substrate due to the low surface energy of both materials. Similarly, the P5G0 sample showed very low adhesion, with visible damage starting at 3 N. Addition of GNPs, on the other hand, increased the adhesion gradually, with maximum values for the P5G0.3, P5G0.4, P5G0.5 samples. Further addition of graphene is detrimental for adhesion, although the values of critical load are still higher than those of the samples without GNPs.

In order to overcome the limitations of the testing technique to provide absolute values of adhesion, and thus estimate the significance of our materials, we conducted tests on a material specifically designed as a bonding agent, ethyl cyanoacrylate. The critical load in this case was indeed higher, as expected, but only by a factor of 2 over our best-performing materials. We consider this

comparison an indirect confirmation of the effectiveness of GNPs to facilitate the application of nylon 66 as a robust coating.
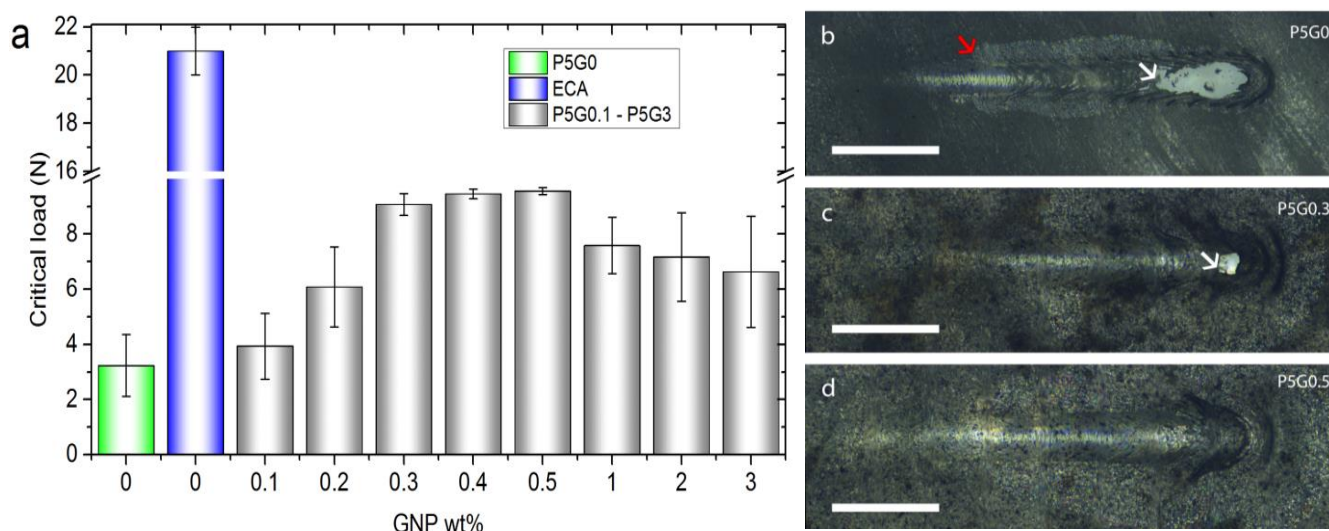
Figure 3.11. (a) Progressive scratch test critical load of nylon 66/PTFE/GNP composites and ECA as reference; Optical images of P5G0 (b), P5G0.3 (c) and P5G0.5 (d). Scale bar is 500 μm. In the absence of graphene (panel b) two damage mechanisms are present: delamination (red arrow) and substrate decohesion (white arrow). With the addition of GNPs, both mechanisms are hindered, first delamination (panel c), then substrate decohesion (panel d).

Observation of the damaged samples using the built-in optical microscope indicates two damage mechanisms, namely delamination and shear-driven material removal. The former is visible in the absence of graphene and is characterized by uplift of an area around the scratch mark (red arrow in Figure 3.11b). The latter can be identified by the removal of the film and the exposure of the glass substrate and appears at low load, ca. 3 N, in the P5G0 samples, while it was not measurable in the unfilled polymer, as mentioned above. With the addition of GNPs, the critical load increases fairly linearly, reaching the maximum for the P5G0.5 sample, which in most cases did not show either damage mechanism (Figure 3.11d). For higher GNPs concentration, values are slightly progressively lower.

Overall, the improvement follows the same trend as the wear tests, with the best performance from the P5G0.5 sample. The enhancement provided by graphene is attributed to its high interfacial energy. At higher GNPs concentration, similarly to the tribological results, the formation of small clusters of GNPs induces the formation of defects at interface, causing the earlier onset of film detachment.

3.4 Conclusions

We have developed a composite coating based on solvent-cast nylon 66 with the addition of PTFE and graphene nanoplatelets in several concentrations. We have found that the friction coefficient, wear rate and adhesion to the glass substrate are greatly improved by the addition of both fillers, provided that the graphene nanoplatelets achieve good dispersion and do not modify the inter-crystallites structure of nylon 66. If this condition is fulfilled, graphene creates a robust transfer film that optimizes the tribological response and increases the interfacial energy. Such optimal condition was found at 0.5 wt.% GNPs, whereas further addition of graphene leads to flakes agglomerates easy to remove upon scratching.

4. Tuning the tribological properties of perflourinated acrylic co-polymer coatings by pH control

4.1 Introduction

Lubrication plays a critical role in our daily lives for energy saving and controlling the CO_2 emission by enhancing the efficiency of fuel and by increasing the machine service life. With the advancement of the field of material science, different novel materials are developed, carrying better surface coating properties that provides more efficient lubrication[122]. Low friction and anti-wear surfaces are the targets of the field of tribology and surface engineering. Liquid lubricants are well known to provide the low coefficient of friction but there are many practical situation where fluid lubricant is not a viable option due to certain limitations including high vacuum, high temperatures, radiations, corrosive gases, high pressure, high loads and in fretting wear and corrosion environment. However these limitations provoked the scientists to work in the field of tribology especially on solid lubricants, the most suitable candidate for the situations where fluid lubricants are not suitable[108]. Applications of solid lubricant where liquid lubricants are undesirable includes space vehicles, aircrafts, automobiles, textile equipment, dental implants, space vehicles, agricultural and mining equipment [123].

Surfactants perform a wide range of functions in tribology as they possess basic lubrication functionality. Examples of surfactants with lubricating properties that can be modified include emulsification/demulsification, oxidation resistance, and corrosion/rust prevention. In surfactants, studies revealed that fluorinated ionic liquids show a low friction coefficient and wear by forming a reactive film on the sliding contact but all these observations are done in liquid phase lubrication. Tribology of surfactants in solid lubricants is relatively unexplored.

Among surfactants, perfluorinated acylic copolymers are particularly interesting materials since they own unique surface properties, such as remarkably low surface energy, low friction coefficient, repellency to both water and oil[124,125,126,127]. In addition, perfluorinated acrylics with C6 chemistry have been approved by the United States environmental protection agency (EPA) for industrial use because of their environmental friendliness[61]. These polymers are vastly utilized in textile or construction industry to obtain hydrophobic and oleophobic surfaces[128]. One of the perfluorinated aclyic copolymer named as Capstone ST-100 is widely used in industry as a penetrating sealant for porous surfaces and as a surfactant and repellent for owning the aforementioned characteristics. Herein, a brief understanding of perfluorinated acylic copolymer as a solid lubricant is conducted.

One of the drawback of perfluorinated acrylic copolymers is that it contains short chains, hence limits its implication in applications of sliding contact due to poor tribological properties of such materials, in terms of either friction coefficient or wear rate. Typical solutions to overcome these limitations include the tailoring or modifying the surface composition. Tailoring of short chain polymers is possible by addition of hard particles to the polymeric matrix and surface modification can be done by chemically modifying the surfaces. One of the example of surface modification is polytetrafluorethylene (PTFE)-aluminum oxide composites as previously it was considered that the surface chemistry is not an important factor in the formation of transfer film and that the effect of counter surface on low wear is purely a mechanical phenomenon, but recent studies have shown that the carboxylate polymer chains form a transfer films that increases the wear resistance dramatically in polymeric solid lubricants[120].

Herein we show the tuning of tribological properties of a polymeric coating, achieved just by pH modulation. To prove the mechanism, samples of a perflourinated acrylic copolymer were produced by spray-coating starting from aqueous dispersions with pH values ranging from 2.6 to 9.1, by addition of either HCl or NaOH. In order to explore the use of the perflourinated acrylic copolymer in contact sealing applications, and to validate the general character of the lubrication mechanism, scratch tests were performed with steel and rubber ball counter parts. In addition, adhesion tests were performed to analyze the effect of pH variation on adhesive/antiadhesive properties. The antiadhesive properties of spray-coatings against vulcanizing rubber can be controlled by formation of polyelectrolyte fluoroacylates as well as by generation of chemical charges. Influence of these chemical charges and polyelectrolyte is systematically explained by analyzing the tribological and anti-adhesive results.

4.2 Materials and Methods

Perfluorinated acrylic copolymer (Capstone ST-100) was purchased from DuPont USA. Capstone ST-100 is a 20 wt.% water dispersion of fluorinated acylic latex developed as a penetrating sealer for porous surface. According to Schutzius et.al.[129] the prepared formulated dispersion meets the goals of US Environmental Protection Agency (EPA) stewardship program which means that the product is environmental friendly as it contains C6 chemistry, a general schematic of the chemical structure is presented in Scheme 4.1. NaOH pellets and HCL solutions were obtained from Sigma Aldrich and used as received. Aluminum substrates were purchased from RS components.
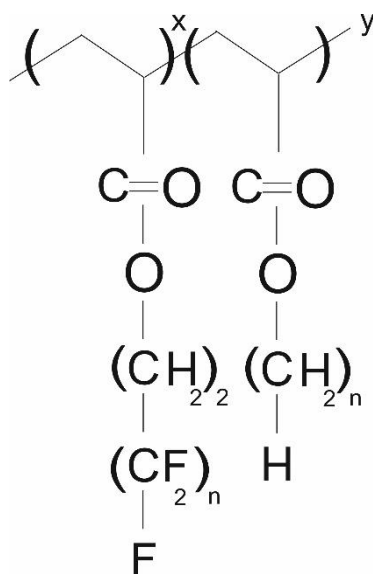
Scheme 4.1. Chemical structure of Capstone ST-100

Different formulations were prepared by diluting perfluorinated acrylic copolymer dispersion (Capstone ST-100) with water to 1 wt.% and then mixing with different volumes of aqueous basic solutions (NaOH, 1.0 mol/L) or acidic solutions (HCL, 1.1 mol/L). Complete detail of formulations is explained in Table 4.1. These formulations were vortex mixed for several minutes and airbrush spray coated on aluminum substrate after washing the substrates with acetone to remove any contaminants.

Table 4.1. Details of water based formulations and their measured pH modulated values

Sample #	NaOH 1.0 mol/L (mL)	HCl 1.1 mol/L (mL)	pH
1	-	0.25	2.6
2	-	1.10	3.4
3	-	-	3.8
4	0.10	-	4.6
5	0.20	-	4.9
6	0.30	-	5.3
7	0.40	-	6.1
8	0.50	-	9.1

Spraying distance was set to 20 cm with a 2 bar gauge air pressure. During spraying, aluminum substrates were heat treated at 130° C for evaporation of solvents and to obtain a uniform coverage of coating. After spraying all the specimen were left at conditions for one hour to cool down under ambient temperature. Thickness of the coatings is calculated between 1-2 μm.

4.2.1 Infrared Spectroscopy

Infrared spectra of the samples were obtained with an Attenuated Total Reflectance (ATR) accessory (MIRacle ATR, PIKE Technologies) coupled to Fourier Transform Infrared (FTIR) spectrometer (Equinox 70 FTIR, Bruker). All spectra were recorded in the range of 600 cm^{-1} to 4000 cm^{-1} with a resolution of 4 cm^{-1}, accumulating 128 scans. For accuracy, three measurements of each sample were recorded.

4.2.2 Tribology Characterization

In order to characterize the tribological behavior of the material, multi-pass scratch tests were performed on a Micro-combi tester (CSM-Instruments, Switzerland) on samples by evaluating friction and wear resistance. A bearing steel ball of 500 μm in radius was used as a counterpart for rubbing. Additionally, a rubber counter ball experiment was run to validate the results from different counter-part materials. Tip displacement rate was maintained at 10mm/min for a reciprocating distance of 4mm under the constant load of 1N for 30 minutes, for a total of 75 cycles (Figure 4.1). All the friction and wear tests were carried out at 20-25°C and relative humidity (RH) of 40-50%.
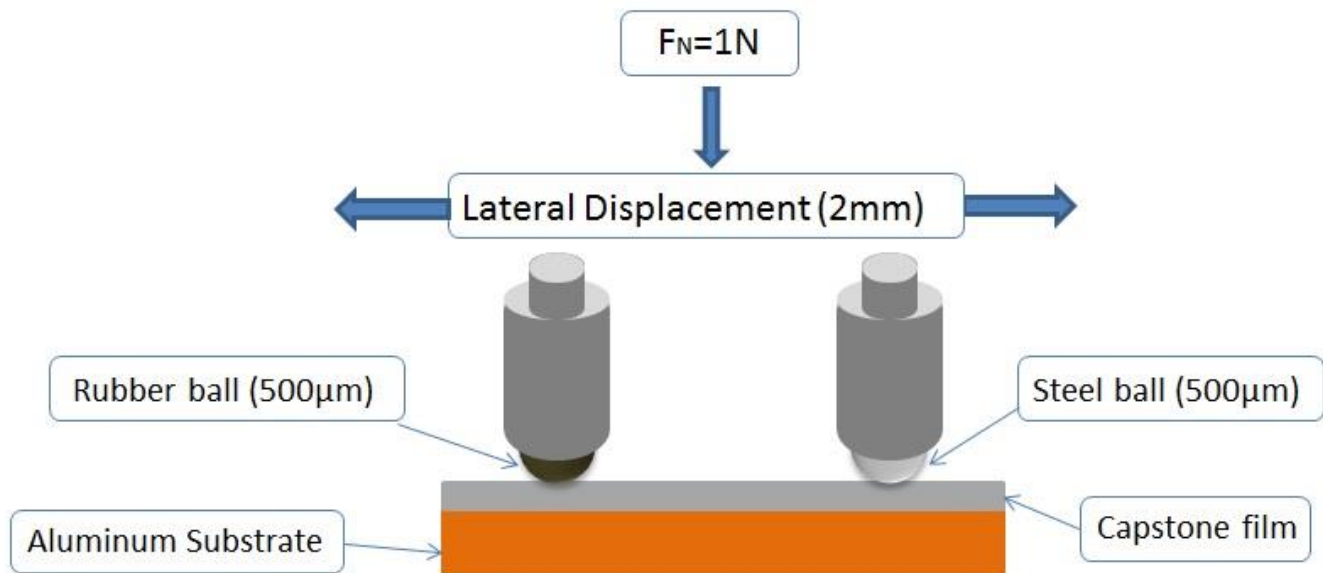
Figure 4.2. *Scheme of scratch test measurements*

The average values of steady-state coefficient of friction were extracted from the experimental data plots of friction coefficient as a function of number of cycles and sliding distance. All the data presented in the current work were the average of five replicate measurements for each substrate.

After each test, the depth of the wear scar d was measured using a stylus surface profiler. Each scar was measured 5 times and average was calculated to use the precise depth of the specimen. Wear volume ΔV of the specimen was calculated from geometrical considerations, by eq. (1),

$$\Delta V = \frac{L}{2}\, r^2 \left(\cos^{-1}\left(\frac{r-d}{r}\right) - \frac{\sqrt{r^2-d^2}}{r} \right) \qquad (1)$$

Where L is the length of stroke in one cycle (mm) and r the radius of the counterpart steel ball (μm). Wear rate was calculated by the ASTM G-99 standard wear rate formula,

$$K = \frac{\Delta V}{F \times N \times L} \qquad (2)$$

Where F is the applied load (N), L the stroke length in one cycle (m) and N represents the total number of cycles, so that N*L is the total sliding length.

4.2.3 Adhesion strength experiment for vulcanizing butyl rubber

An ad hoc experiment was designed to measure the antiadhesive properties of perfluorinated acrylic copolymer in rubber tire vulcanization process and to measure the consequent effects of pH on adhesion strength. The fundamental step of experiments are explained in Figure 4.2. After spray coating the perfluorinated acrylic copolymer on aluminum substrates, surface was overlaid with the sheet of uncured butyl rubber. Alumina plate without any coating was attached on uncured rubber on the uncovered face and was hot pressed for 30 minutes at 150° C. The adhesion strength was measured needed to separate the butyl rubber from coated material substrate. For this purpose, an ad hoc configuration of instrument (Instron 3365 Dual Column) was implemented. The top non-coated aluminum substrate was connected to the moving arm of the Instron by steel wires and mechanical arm was moved vertically at a speed of 3 mm/min. The force required for the movement was recorded until the top non-coated aluminum substrate detaches from the coated aluminum substrate.
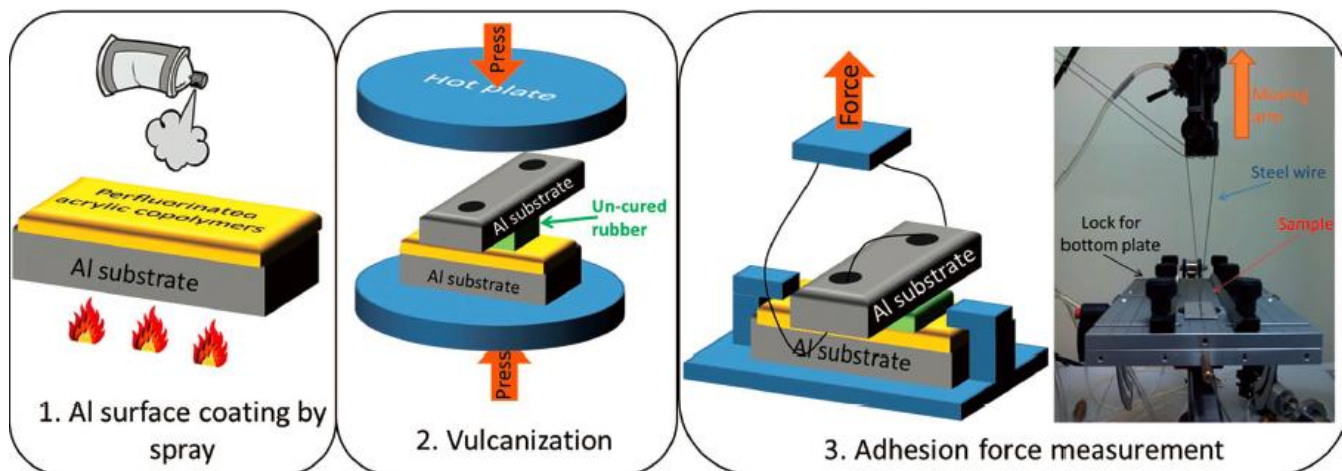
Figure 4.2. Schematic of the fundamental sets of experiment designed to measure adhesion strength of perfluorinated acrylic copolymer sprayed on aluminum substrate and a process of volcanizing rubber tire, one side attached with the polymer coating and other side attached with aluminum. Last section photograph indicating the mechanism of designed experiment.

4.3 Achieved Results

4.3.1 Chemical Analysis

Chemical characterization was performed by ATR-FTIR to analyze the spectral changes occurred by chemical interactions. Figure 4.3 A shows the IR spectra in the region between 1800-600 cm^{-1} of samples with different pH values including 9.1, 3.8 and 2.7 respectively. Main bands for pristine Capstone ST-100, pH 3.8, were associated with $-CF_2-$ groups (asymmetric and symmetric CF_2 stretching modes at 1238 cm^{-1} and 1143 cm^{-1}, respectively) and ester functional groups (C=O stretching mode at 1733 cm^{-1} and C–O–C stretching mode at 1192 cm^{-1}), methylene (CH_2 scissoring bend at 1465 cm−1 and CH_2 rocking bend at 728 cm−1) groups are observed. When acid is added to the aqueous solution, pH 2.7, there is no chemical spectral change observed in the system. On the other hand after adding base, pH 9.1, two new vibrations are observed and ascribed as carboxylate functional groups (asymmetric and symmetric COO− stretch at 1560 and 1411 cm−1, respectively). Ratios between intensities of bands at 1560 cm^{-1} (carboxylate stretching) and 1732 cm^{-1} (carbonyl stretching) are calculated to show how exponentially or gradually the ratio increases or decreases after addition of acid or base (Figure 4.3 B). Results revealed that for the as prepared and acidic samples, ratio is zero but after addition of base, in the range of pH 3.8 to 6.1, the ratio exponentially increases and later on from 6.1 to 9.1 ratio is more gradual.

Based on this increment in ratio after adding base, we presume that a reaction of saponification occurred between the ester groups of the perfluorinated acrylic co-polymer and the NaOH molecules resulting in the production of sodium carboxylates and alcohol residues (Figure 4.3B inset). A model is drawn to further explain the mechanism, shown in Figure 4.3C for the reactivity of the generic perfluorinated acrylic co-polymer with acid and base. Chemical charges (carboxylate anions and sodium cations) are formed along with production of sodium carboxylate groups and nominated as fluoroacrylic polyelectrolyte polymer.
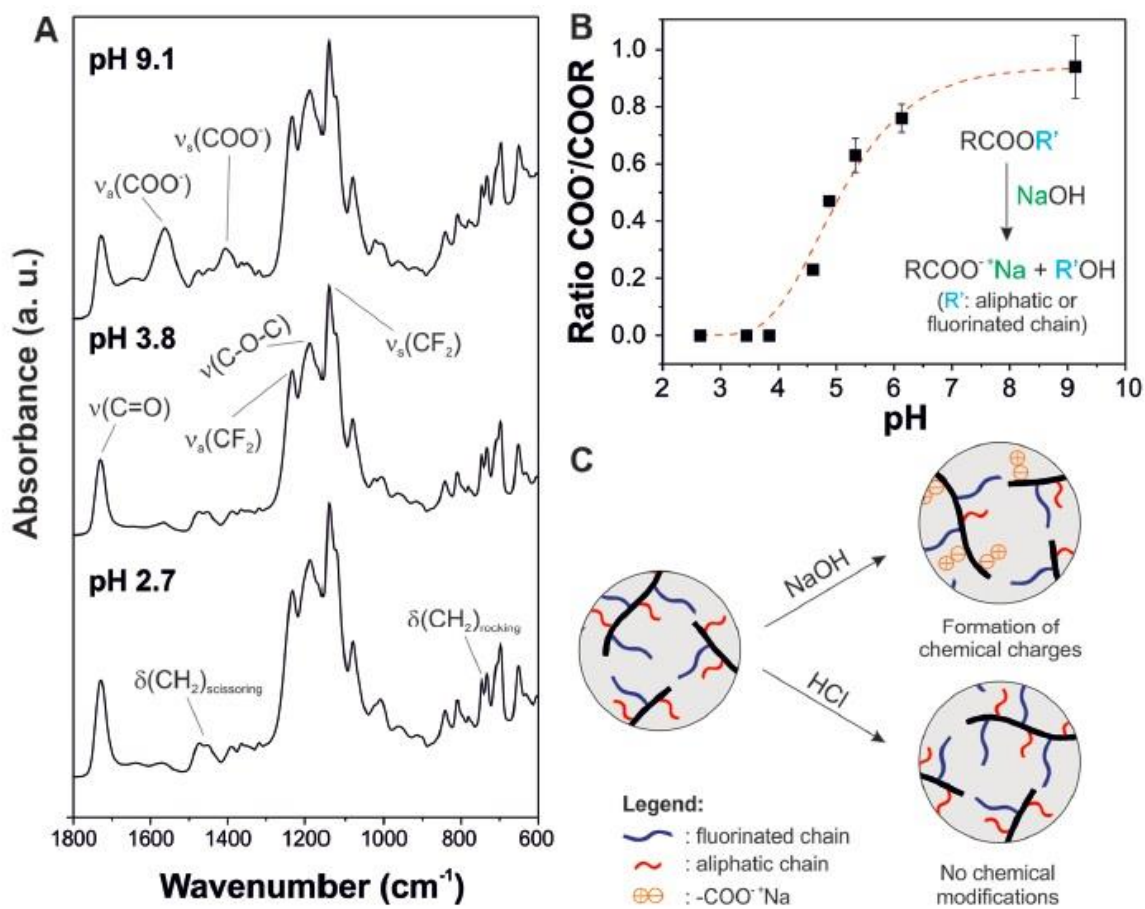
Figure 4.3. A) ATR-FTIR spectra of sprayed perfluorinated acrylic copolymer coating with variant pH conditions. B) Variation of the ratio of intensities of carboxylate and ester groups at different pH conditions. C) Schematic representation of chemical reactivity with NaOH and HCl.

4.3.2 Tribology and adhesion results

Tribological tests were performed on unmodified perflourinated acrylic copolymer coatings and by varying the pH content in the polymer dispersion. As discussed previously, improvement of such short chain polymers contains significant importance due to their versatile use in industry. Improvement in

the tribology and adhesion is analyzed systematically by measuring friction, wear and adhesion. The friction coefficient and wear rate of perfluorinated acrylic copolymer coatings on aluminum substrate as a function of pH are presented in Figure 4.4 and 4.5, respectively. It can be seen that addition of HCl (pH < 3.8) does not modify the tribological properties of the material whereas on contrary, addition of NaOH (pH > 3.8) resulted in exceptional improvement in friction coefficient and wear resistance. In detail, increasing the base (NaOH) resulted in a large decrease in coefficient of friction; the lowest average friction measured was ca. 0.116, obtained for pH 5.3, while the highest value was ca. 0.338, for pH 3.8. The rise in pH significantly reduced the friction coefficient of the coating, leading to 3 times lower frictional coefficient, shown in Figure 4.4. Similarly while using rubber ball for counterpart, friction values decreased from ca. 0.53 to ca. 0.32 at pH 5.3 showing that friction was reduced not only for steel counterparts but also for rubber counterparts.
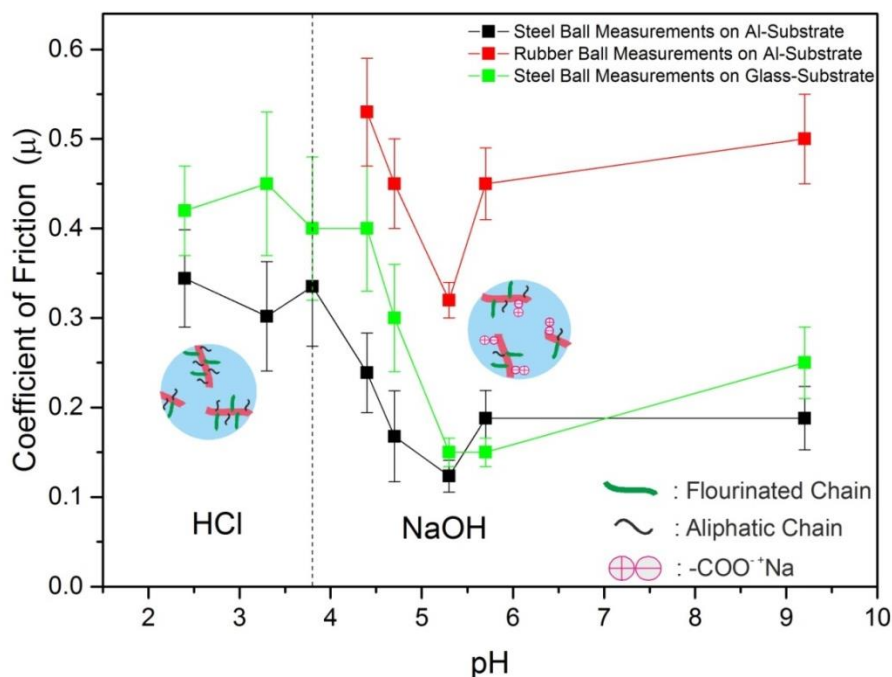
Figure 4.4. Friction coefficient results for steel and rubber counterparts conducted on the perfluorinated acrylic copolymer coatings with variable pH concentrations.

A similar behavior can be seen in Figure 4.5 for the wear rate measurements: the increment of pH to fluoropolymer improved the wear resistance, with a minimum at pH 5.3. Significant decrease in wear rate was observed which is quite evident, with 48.14×10^{-3} mm^3/N-m wear rate at pH 3.8 which is improved to 0.73×10^{-3} mm^3/N-m at pH 5.3 reporting over 65 times reduction in wear rate.
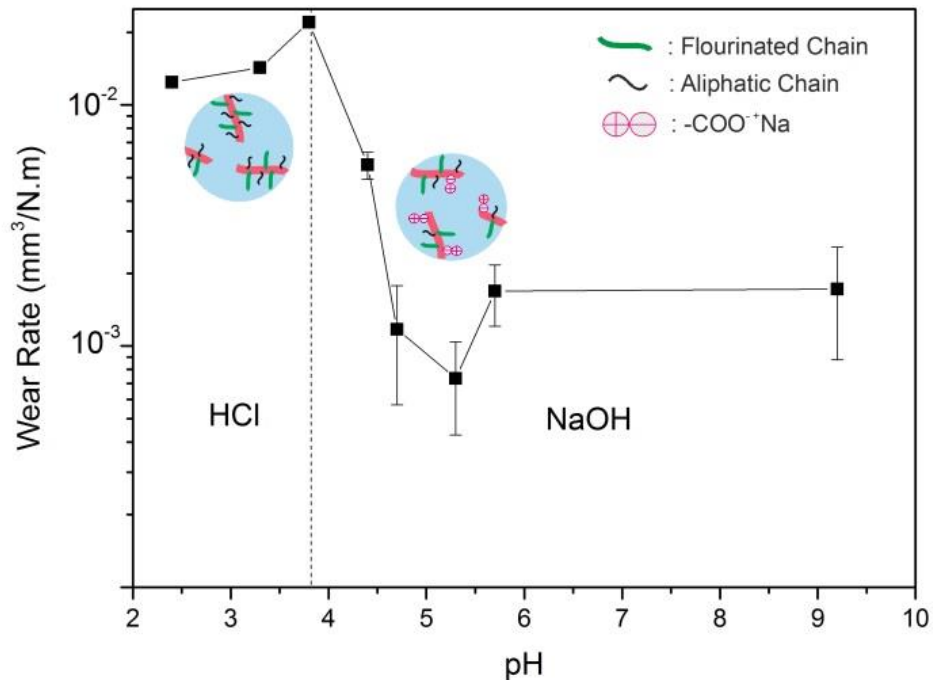
Figure 4.5. Average values of wear rate measured on perfluorinated acrylic copolymer coatings with function of pH modulation.

The adhesion results are explained in Figure 4.6 showing the variation of measured rubber/aluminum adhesion force, as the function of pH of the perfluorinated acrylic copolymer dispersions. These experiments were performed using an ad hoc system designed to simulate the rubber tire vulcanization process and to measure the consequent adhesion force required to detach coated substrate from butyl rubber (Figure 4.2). As can be seen in Figure 4.6, aluminum substrates coated with non-modified perfluorinated acrylic copolymer dispersions, pH 3.8, are strongly bonded to the vulcanized rubber and force required to detach it from the coated substrate is close to 80 N. Adhesion force does not change appreciably when pH is reduced with HCl (pH < 3.8) showing no significant improvement for the anti-adhesive perspective. On the other hand increasing pH with NaOH (pH > 3.8) shows a remarkable improvement in releasing capacity of the coating. In particular, a minimum adhesion force with 6 N was observed for the case when pH was maintained at 4.7 that is ten times less than the actual adhesion force of non-modified perflourinated acrylic copolymer. Stable adhesion force between 6 N to 14 N was observed in the range of pH (4.7 - 5.5) and interestingly it's the same region where we observed the low coefficient of friction and improved wear rate signifying the appropriate pH range where carboxylate functional groups were formed that are thought to be responsible for such improvement.
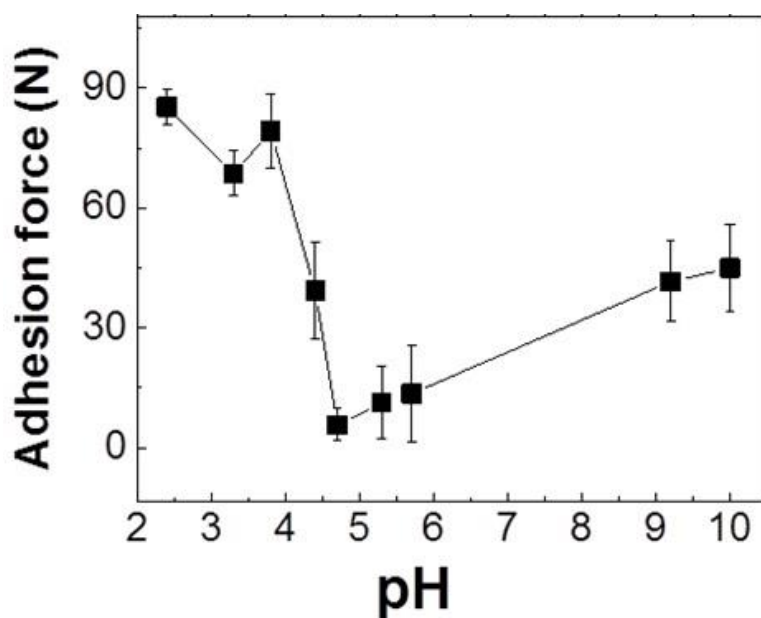
Figure 4.6. Adhesion force between rubber and aluminum spray coated with perfluorinated acrylic copolymer dispersions with different pH conditions.

The improvement in the tribological properties (reduction in friction coefficient and wear rate) and release capability of the surfaces (anti-adhesive properties) due to solution's pH adjustment (close to pH 5) can be attributed to lowering of surface energy that can lead to reduction of Van der Waals interactions between bodies[130]. Carboxylate groups are thought to be responsible for lowering the wear rate as previously it is proved that metal carboxylates can create a transfer film upon sliding contact, which can substantially reduce the friction coefficient and material damage with numerous contribution in lubricants, used as additives[131,132]. Specifically for NaOH, the improvement can be referred to chemical modifications occurred after formation of sodium carboxylates.

4.4 Conclusions

Tribological tests were systematically investigated, experimental results show that fluoropolymer with 1% concentration of water, with addition of 300μl NaOH, leading to pH 5.3, yielded significant decrease in friction coefficient and high wear resistance as compared to other formulations. Friction coefficient was decreased 3 times and wear rate was reduced from 48.14×10^{-3} mm^3/N.m to 0.73×10^{-3} mm^3/N.m reporting over 65 times reduction in wear rate. Thus the friction and wear properties of fluoropolymer can be enhanced significantly by tuning its pH. Furthermore, adhesion results revealed that adhesion force for base-modified formulations changed significantly to 6 N from 80 N (for non-modified configurations).

5. Environmentally benign ultra-transparent PECA coatings with multifunctional applications

5.1 Introduction

Cyanoacrylates have been used since decades in adhesives, forensic sciences and medical applications[133] for its non-toxicity, biodegradability and non-immunogenic behavior[134]. However usage of cyanoacrylate is limited by its intrinsic brittleness, high reactivity and extremely rapid anionic polymerization[135]. These limitations can be tuned by appropriate solvents, chemically modify the alkyl chains with moieties or by physically blending with other components such as plasticizers or thermoplastic elastomers, allows to tailor their mechanical and chemical properties[136].

Poly ethyl 2-cyanoacrylate (PECA), a member of cyanoacrylate family, contains short chains with less toxicity as compared to methyl structured cyanoacrylate [137]. Among other properties of PECA, control of polymerization and transparency has paramount importance due to their increasing use in fabrication of superhydrophobic surfaces[138,139], drug delivery nanoparticles[140,141] and in flexible lithium ion batteries [126,142] to name a few. The main challenge of fabricating PECA coatings is that cyanoacrylate monomers are high reactivity under ambient conditions as well as their instability under elevated temperatures. Previously lot of research has been conducted to control the rapid polymerization of alkyl cyanoacrylates. For instance Mele *et al.*[143] controlled the polymerization of PECA by adding dimethyl sulfoxide (DMSO) and acetone to fabricate zwitterion nanofibers coatings. Similarly Han *et al.* [144] controlled the degradation of PECA by copolymerizing poly methyl methacrylate (PMMA) with free radical bulk polymerization. Nevertheless very few studies have been conducted on transparency of PECA coatings.

Control on transparency of cyanoacrylates is an intricate phenomenon and is strongly related to solvent dependence and evaporation rate. The solubility parameters of cyanoacrylate monomers in various common solvents have been reported[145]. Cyanoacrylate allows good solubility in polar solvents such as dimethyl formamide, acetone, dimethyl sulfoxide (DMSO). Few of the polar solvents start exothermic reaction with the cyanoacrylate monomers, like DMSO can initiate the zwitterion polymerization instantly[146]. Although these solvents contribute in initialization of polymerization but to obtain transparent coatings from such solvents is difficult. The ketones can be considered moderately polar aprotic solvents[147]. Cyclopentanone, cyclic ketone, is used in numerous industrial applications as a green solvent with high boiling point of 130°C and is recently added in the GSK green solvents

guide[148]. For the very first time, cyclopentanone has been used for solubility of ECA monomers and for fabrication of PECA coatings. High boiling point of cyclopentanone makes it more suitable for controlled polymerization of ECA. To overcome the brittleness, benzyl alcohol was added along with ECA monomers at different v/v ratios. Interestingly there was no phase separation observed during polymerization and a negligible reduction in transparency was observed. In addition, role of benzyl alcohol is also to inhibit the anionic polymerization of ethyl cyanoacrylate.

Herein, we report a simple inexpensive method for fabrication of highly transparent poly ethyl-2-cyanoacrylate (PECA) coatings. The process is a single-step solution casting from a common solvent, cyclopentanone, of ethyl-2-cyanoacrylate monomers. The prepared coatings and free standing films demonstrate remarkable transparency (higher than 92%) with first report to achieve it. The morphology, thermo-physical properties of the PECA coatings are characterized. By taking advantage of its low contact angle hysteresis, developed material is proposed for the fog harvesting application and significant results are achieved. Furthermore, tribological properties of steel are improved by decreasing the friction more than 6 times and wear rate was improved more than 9 folds by self-assembling graphene nanoplatelets in ECA solution.

5.2 Materials and Methods

Ethyl 2-cyanoacrylate (ECA, Permabond 105, Sigma Aldrich), cyclopentanone, benzyl alcohol, glycerol, diiodomethane, dimethyl sulfoxide (DMSO) were purchased commercially. Grade pure G+ graphene nanoplatelets (GNPs) with lateral dimensions of few micrometer and a thickness of few nanometer were kindly provided by Directa Plus (Lomazzo (CO)-Italy). All the chemicals were used as received without any further purification.

Ethyl 2-cyanoacrylate (4.48 ml), highly active monomer, was homogeneously mixed in 50 ml cyclopentanone. Benzyl alcohol was added in accordance with v/v ratio of ECA ranging from 10-50%. Solutions were drop casted on microscopic glass slides after cleaning with acetone and bath sonicated for 60 min. Drop casted solutions were covered by aluminum foil cups after making small holes on the surface to obtain uniform coatings and left in aspiration hood for 24 hour. Obtained coatings were named according to concentration ratios between ECA/benzyl alcohol including PECA [100:0], PECA [90:10], PECA [80:20], PECA [70:30], PECA [60:40] and PECA [50:50] respectively.

5.2.1 Optical and Thermal Characterization

UV-vis spectra was performed to investigate the transparency of all fabricated samples. Square shaped specimens (2×2 cm^2) were cut from glass deposited coatings and free-standing films. The UV absorbance measurements were carried out by Varian CARY 300 Scan UV-visible spectrometer in the wavelength range of 200-800 nm. The transmittance percentage values were calculated using following equation.

$$T(\%) = \left(\frac{1}{10^A}\right) \times 100$$

Where, T and A are transmission and absorbance values of the experimented material, respectively.

The materials degradation temperature was evaluated by thermogravimetric analysis (TGA). Samples were scanned from 30° C to 600° C at a heating rate of 5° C/min under nitrogen atmosphere set as a flow rate of 50 mL/min. TGA data were analyzed in the form of mass loss and rate of mass loss derivative with respect to temperature.

5.2.3 Chemical and Morphological Characterization

μRaman spectra were collected at ambient conditions using a μRaman spectroscopy (Renishaw Invia, United Kingdom), equipped with a microscope. A 514 nm laser excitation line, in backscattering geometry through a 100x objective lens, was used to excite the specimens with numerical aperture of 0.75 at low power of 0.4 mW. Raman spectra were collected from the pristine surface, as well as from the scratch, after the wear test. Chemical changes in the structure were further studied by attenuated total reflectance-fourier transform infrared (ATR-FTIR) spectrometer (Equinox 70 FT-IR) equipped with an ATR accessory (MIRacle ATR, PIKE Technologies). All spectra were acquired in the range from 4000 cm^{-1} to 600 cm^{-1} with 4 cm^{-1} resolution, accumulating 128 scans.

The morphology of the coatings was observed by scanning electron microscopy (SEM, JEOL JSM-6490AL operating at 10 KV) after sputtering 10 nm gold coating prior to imaging.

5.2.4 Mechanical and Tribological Characterization

The Young's modulus and hardness of the coatings were characterized by nanoindentation on an Anton Paar UNHT equipped with a diamond Berkovich tip. Maximum load was 1mN whereas loading and unloading time was 30 s, with a dwell time at maximum load of 30 s to allow viscous relaxation.

Young's modulus E and hardness H of the materials were calculated by the Oliver & Phar method with at least 10 repetitions for each material.

Multi-pass scratch tests were performed on a Micro-combi tester (Anton Paar Gmbh, Germany), to evaluate friction and wear resistance. A bearing steel ball of 500 μm radius was used as a counterpart for rubbing. The tip displacement rate was 20 mm/min for a reciprocating distance of 4 mm, corresponding to a frequency f= 0.042 Hz, under the constant load of 5 N, for 300 cycles, corresponding to 30 minutes. All the friction and wear tests were carried out at laboratory conditions (21 ± 1°C, 50 ± 5%RH).

The average values of steady coefficient of friction, following the running-in phase, were extracted from the experimental data plots of friction coefficient. All the data here are the average of five replicate measurements for each material. After each test, the depth of the wear scar d was measured using a stylus surface profiler (DektakXT, Bruker). Each scar was measured 5 times and the average was calculated. The wear volume, ΔV, of the specimen was calculated from geometrical considerations, with Equation (1):

$$\Delta V = \frac{L}{2}\, r^2 \left(cos^{-1}\left(\frac{r-d}{r}\right) - \frac{\sqrt{r^2-d^2}}{r}\right) \qquad (1)$$

where L is the length of the stroke in one cycle and r is the radius of the counterpart steel ball. The wear rate was calculated by the ASTM G-99 standard wear rate formula:

$$K = \frac{\Delta V}{F \times N \times L} \qquad (2)$$

where F is the applied load (N), L the stroke length in one cycle (m) and N represents the total number of cycles, so that NL is the total sliding length [34].

Moreover, the adhesion of coatings deposited on the glass substrates was evaluated by a progressive scratch test, during which the load was increased linearly from 0.03N (Hertzian pressure $p{\sim}60\ MPa$) to 10 N ($p{\sim}190\ MPa$) over a scratch length of 2 mm, with a sliding rate of 1 mm/min and acquisition rate of 30Hz.

5.3 Results and Discussion

5.3.1 Surface Morphology and Transparency

Figure 5.1(a-c) demonstrates the PECA coatings with different solvents including acetone, DMSO/acetone and cyclopentanone. It can be seen that both of the films deposited in acetone and DMSO appeared to be opaque whereas with cyclopentanone PECA coatings were ultra-transparent. Reason for such transparency can be attributed to slow evaporation of solvent that let the monomers react in a controlled way with moisture in the air. Two factors that can significantly impact on transparency of cyanoacrylate are selection of high-boiling point solvent and controlled environmentfor evaporation. Both of these factors were acknowledged, as cyclopentanone has high boiling point $\approx 130°$ C and controlled environemnet was provided by covering the drop casted samples with aluminum foil with controlled hole size in it. SEM analysis was performed on different prepared coatings for analyzing the surface morpohology. SEM images (Figure 5.1d, 5.1e) revealed that PECA coatings prepared in DMSO and DMSO/acetone solvents contain some defects on the surface, visible throught the images. Whereas PECA coatings prepared with cyclopentanone are more smooth and uniform as shown in Figure 5.1e. Roughness of the PECA coatings prepared with cyclopentanone was less than 20 nm.
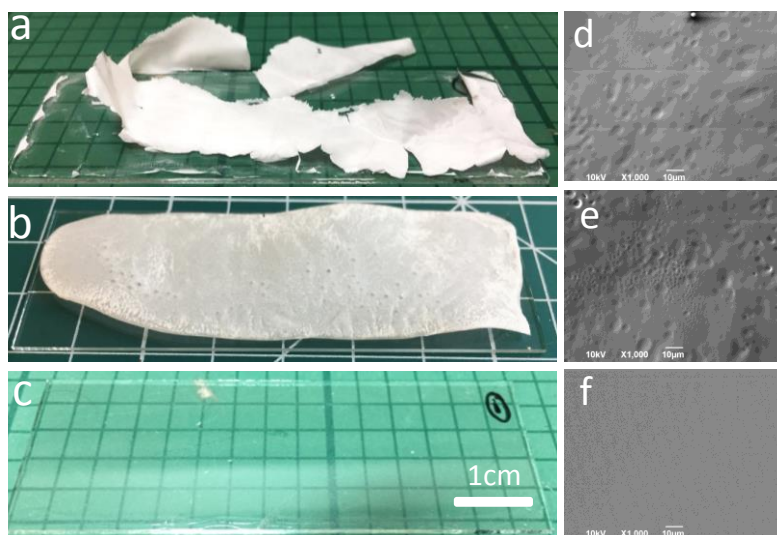
Figure 5.1. (a-c) Photographs of PECA coatings, prepared in different solvents. (a) PECA film prepared in acetone solvent. (b) PECA film prepared in DMSO/acetone. (c) Drop casted PECA coating processed in cyclopentanone (d-e) SEM images of PECA in different solvents (h) UV-vis spectra of PECA coatings and free standing film, inset shows the glass substrate coated with PECA flexible transparent PECA film

UV-vis spectra measurements were performed to determine the transparency of PECA coatings. The produced PECA coatings were highly transparent to visible light, with transmission spectra showing 99.9% transparency when coated on glass substrates as shown in Figure 5.2. Transmittance reduced to 98.5 percent after 1:1 v/v ratio addition of benzyl alcohol. It is worth noting that these measurements were performed with reference to glass substrate. Similarly transparency tests were conducted for free standing PECA films for a good comparison to other transparent materials. PECA [100:0] exhibited more transparency as compared to glass and many other commercially available transparent films. For microscopic glass, transparency was recorded around 91.4% (shown in green dotted lines, Figure 5.2) whereas for PECA [100:0] transmittance was approximately 92.5%. Interestingly our fabricated PECA coatings are more transparent than poly methyl methacrylate (PMMA) allowing 92% transmittance[149].
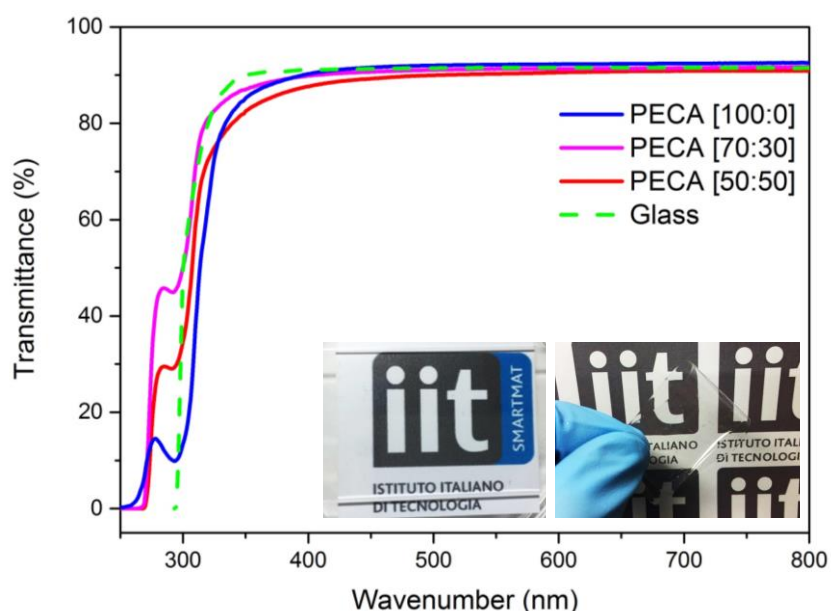
Figure 5.2. UV-vis spectra results for PECA with variant concentrations of benzyl alcohol and pristine glass

5.3.2 Chemical characterization and TGA results

ECA polymerizes rapidly with the atmospheric moisture, called the anionic polymerization, where a nucleophile attacks its β-unsaturated carbon to form a carbanion. The resulting carbanion attacks another monomers and cascades the polymerization reaction. Responsible elements for higher rate anionic polymerization of ECA are electron withdrawing groups,–CN and –COO– bonded to its α-C, stabilizes the resultant carbanion[150]. The polymerization mechanism of ECA is explained in Figure 5.3. It has been reported previously that polar solvents can initiate the zwitterion polymerization of n-alkyl 2 cyanoacrylates [143]. According to this model we can state that the polymerization of ECA monomers

started in the solvent, cyclopentanone (weak O-H bonding at CH_3 terminus) following the anionic polymerization that mainly occurred due to moisture in the air leading to chain propagation. Compared to the frequently used free radical polymerization mechanism, the anionic polymerization has the advantages of tolerance of oxygen and moisture, lower polymerization activation energy, and long living active centers. Tolerance of oxygen and moisture allows its polymerization occurred inside the solvent and under air environment whereas low activation energy and long living active centers permit its polymerization under ambient temperatures, resulting in high molecular weight polymer. Herein, role of benzyl alcohol is to inhibit the rapid polymerization and can act as a terminator for the polymerization as the protons and hydroxide can terminate the process that can be transferred from either from benzyl alcohol or from water molecules.
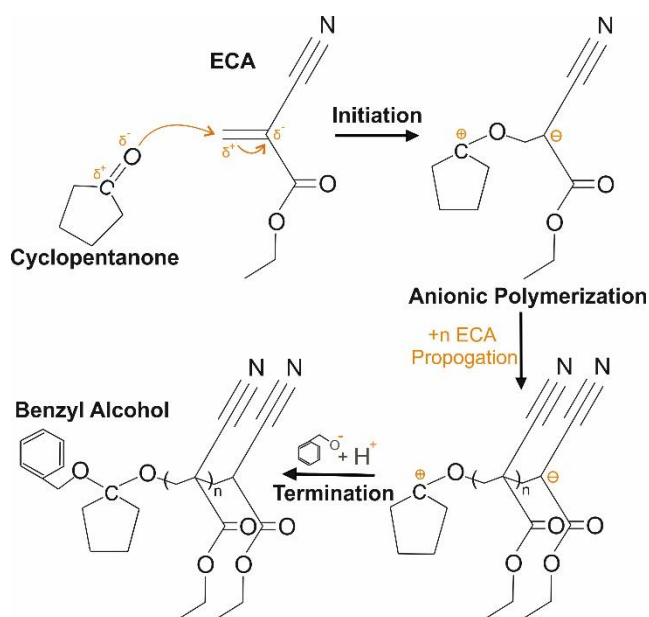
Figure 5.3. Proposed scheme of the reactions occurring for the polymerization of ECA (initiation, propagation and termination).

The reaction occurring and polymerization confirmation was done by comparing the Fourier transform infrared spectroscopy (FTIR) spectra of the PECA coatings with benzyl alcohol concentrations. Several bands assigned to the functional groups of the polymerized ethyl 2-cyanoacrylate molecule can be identified in Figure 5.4a. A strong absorption band at 2991 (–CH2, asymmetrical stretching vibration), the conjugated C=O stretching at 1742 cm^{-1}, the C=C stretching at 1614 cm^{-1}, and C–O stretching vibration at 1248 cm^{-1} [151,152,153]. The disappearance of peaks at 3127 cm^{-1} (=CH2, stretching vibration) and 1665 cm^{-1} (–C=C–, stretching vibration) in PECA confirmed that the polymerization reaction was completed. The peaks due to C $\equiv$ N stretching for PECA is seen at 2250 cm^{-1} (shown in inset of Figure

5.4a). In the ECA monomers, –CN stretching is observed at 2239 cm^{-1} [154]. This shift in wavenumber is due to the significant stabilization of the carbanion formed by delocalization of the negative charge, or an effect of inter- and intramolecular hydrogen bonding[155]. The presented IR spectrum consists of the typical vibrations of PECA without contribution of cyclopentanone solvent. However a very broad peak of O–H stretching appeared for PECA [70:30] and PECA [50:50] at 3335 cm^{-1} mainly due to benzyl alcohol. PECA was found to interact with benzyl alcohol via hydrogen bonding.
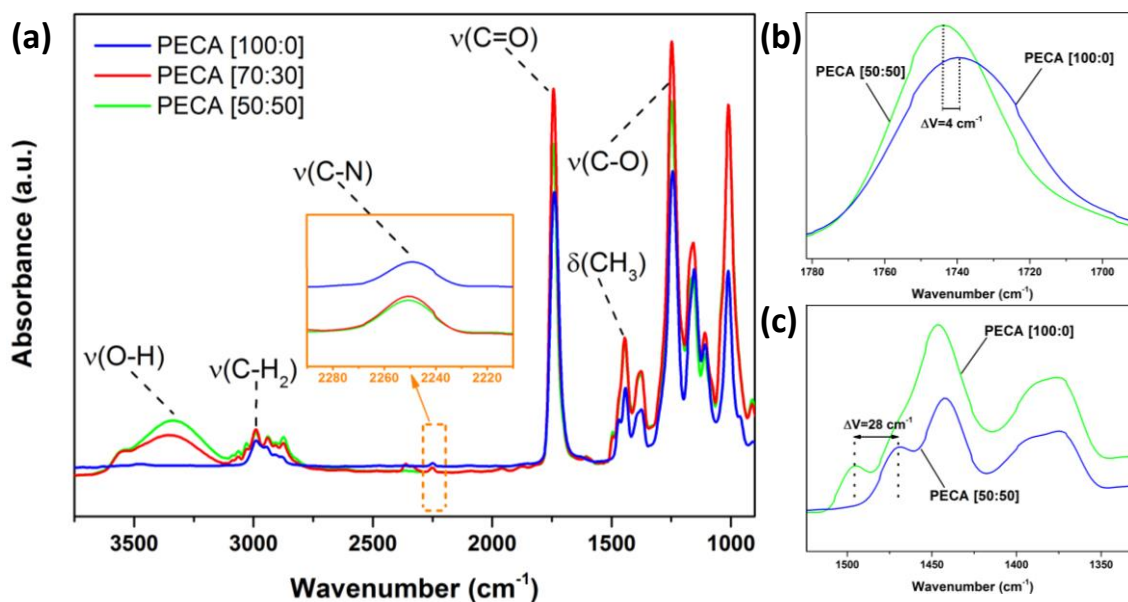
Figure 5.4. (a) FTIR spectra of PECA with different concentrations of benzyl alcohol. (b) Figure 5.4 (b & c) showing the shift of peaks occurred at conjugated C=O stretching,1742 cm^{-1}, with a shift of 4 cm^{-1} wavenumber. Whereas a shift of 28 cm^{-1} wavenumber is observed at CH$_3$ bending, 1467 cm^{-1}. Please note that these shift in wavenumbers were observed after addition of benzyl alcohol in the monomer content.

Thermal degradation mechanism of the prepared PECA and PECA/benzyl alcohol coatings was investigated by thermogravimetric analysis (TGA) as shown in Figure 5.5. PECA typically degrades in two primary steps. First degradation starts at ≈160 °C corresponds to first step, which is the degradation of hard segments in cyanoacrylate and the formation of isocyanates and alcohols, primary or secondary amines, olefins, and carbon dioxide. The second step degradation is associated with soft segment degradation (160 °C – 250 °C), leading to remaining thermal decomposition that is in agreement with the literature[156],[157]. There is no residue remaining beyond 390 °C. Benzyl alcohol, however hindered the polymerization of PECA and caused it to degrade earlier at around 225°C. Inset of Figure 5.5 shows first weight derivatives for pristine PECA and PECA with benzyl alcohol at

different volume fractions. Pristine PECA [100:0] demonstrates a sharp derivative peak at 240 °C, however, when mixed with benzyl alcohol, two small peaks appear at 241 °C and 220 °C. Further addition of benzyl alcohol resulted a complete transition to sharp peak at relatively lower temperature ca. 210 °C. This transition of first weight derivative for PECA and benzyl alcohol endorse a strong chemical interaction between benzyl alcohol and cyanoacrylate groups as seen in the FTIR spectra.
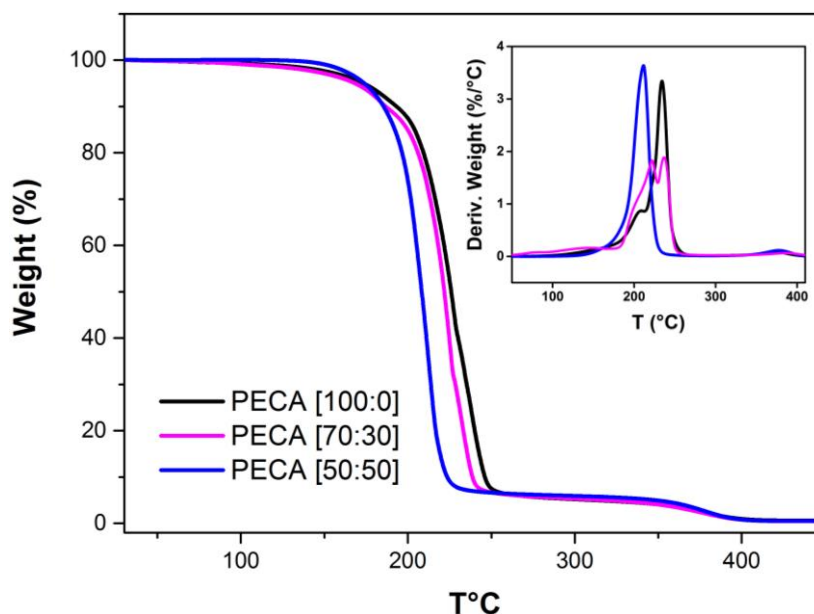
Figure 5.5. Thermogravimetric analysis (TGA) of pristine PECA and PECA with benzyl alcohol. Inset showing derivative weight percentage loss of PECA with and without BnOH.

5.3.3 Annealing effect on adhesion of PECA coatings

To evaluate the adhesion between PECA coatings and the glass substrate, progressive scratch tests were performed on films deposited on glass slides. The critical load for failure was then investigated by SEM. Figure 5.6 (a-d) presents the residual scratch patterns after progressive load scratch test with the diamond indenter. Coatings containing benzyl alcohol, Figure 5.6 (a-c), exhibited several fractures. These kind of fractures can be ascribed to the tensile cracking mechanism where the indenter advances along the scratch direction while compressing the material ahead and the material behind is stretched [158]. Such fractures are generated when external load overcomes the ultimate strength of the coated material [159]. Another aspect for such formulations of cracks is that benzyl alcohol hindered the polymerization of ECA that can cause result of short chain polymerization, not sufficient to bear the critical load of diamond counterpart and resulted in cracks formulation.

To evaluate the deformation caused by compression in progressive scratch test, compression zone area was calculated in accordance with applied load. According to statistics, scratched width becomes narrower after addition of benzyl alcohol (Figure 5.6f) that is predominantly due to decrease in plasticity of the material. Figure 5.6e is the SEM image of PECA coatings without annealing whereas annealing at 130°C for 10 minutes made a detrimental effect and enhanced the scratch resistance (Figure 5.6d). It is presumed that there were still the solvent residues inside the coating that weakens the adhesion between PECA coatings and the glass substrate.
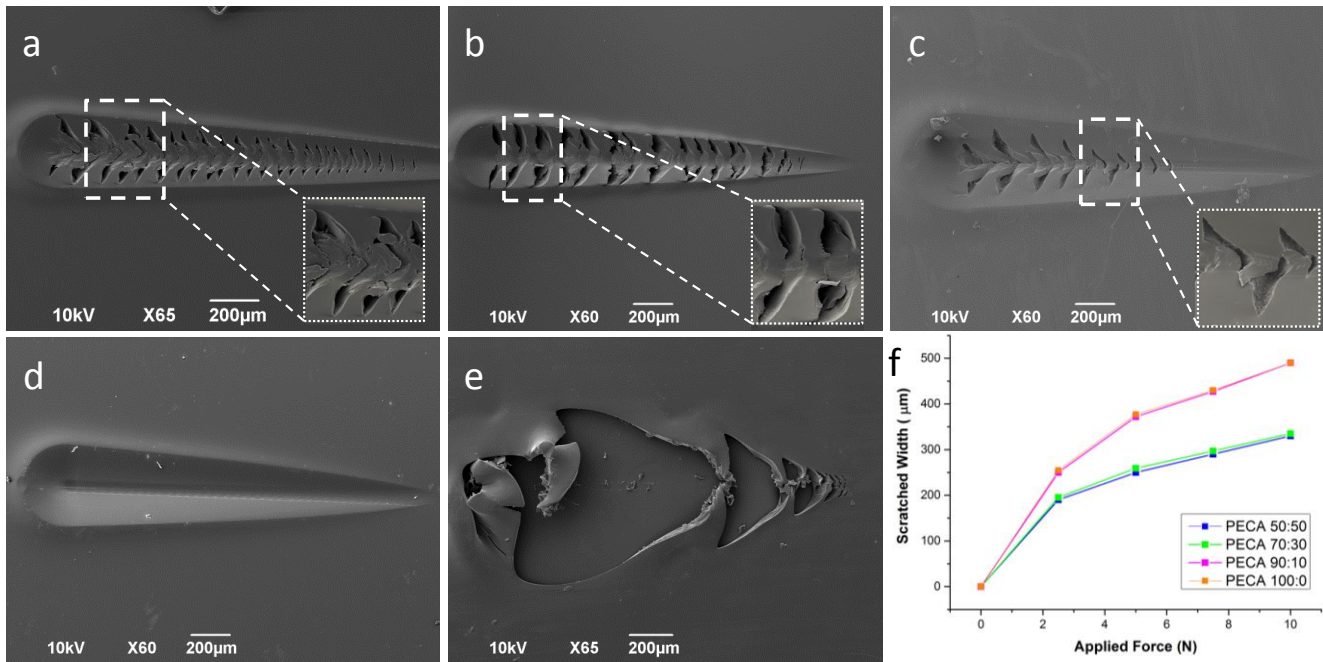
Figure 5.6. Progressive scratch test SEM images and scratched width analysis (a-d) SEM images of annealed PECA coatings with variant benzyl alcohol concentrations; PECA 50:50, PECA 70:30, PECA 90:10 and PECA 100,0 respectively (e) SEM image of PECA 100:0 without annealing (f) Comparison of scratched width at compression zone in different applied force regions.

5.4 Applications

5.4.1 Fog Harvesting

Water shortage has been a major problem in arid and humid environments. One of the solution is collecting water from foggy wind inspired by darkling beetles of the Nambia desert and biomimetic approaches [160]. Although much research has been conducted on creating contrast surfaces i-e, both hydrophobic and hydrophilic structures for good efficiency of water collection but these surfaces are hard to fabricate and are applicable only in laboratory environment [161]. Hurdle of creating these structures at micro and macro level demands a new material with ease of processing that contains

hydrophilic characteristics while exhibiting low contact angle hysteresis. For the first time, cyanoacrylate has been experimented for the application of fog harvesting. Its hydrophilic nature (best for pinning the micro and nano-droplets initially) and low contact angle hysteresis (ideal for coalescence and water sliding) makes it an ideal candidate for water collection applications.

An experimental setup (Figure 5.7a) established recently by Davis et al.,[162] was used for estimating the water collection ability of fabricated transparent cyanoacrylate coatings. The designed experiment allows for the recording of the total amount of water collected during the entire test, the time and weight of each collection episode, eventually providing more accurate and reliable results. An absolute comparison with other reported materials from literature is problematic, as the results are strongly dependent on testing conditions and fog accumulation sources. To address the concern, a direct comparison has been performed by choosing superhydrophilic, hydrophobic and superomniphobic materials as a control specimens. Four different materials were selected for water collection efficiency comparison including glass slides, polytetrafluoroethylene (PTFE), superomniphobic (SO) surface with poly dimethylsiloxane (PDMS) islands on the surface[162] and PECA coatings with different concentrations of benzyl alcohol.

The mechanism of fog collection, composed by the phases of pinning, coarsening and sliding, is explained in Figure 5.7b. Water condensation was observed after few minutes of fog exposure followed by coalescence, droplets sliding and water dripping from the substrate. Interestingly water condensation started very early on the surface after 15 minutes, which is attributed to the hydrophilic nature of the material. These tiny condensed pinned droplets converted into relatively big droplets after few more minutes of fog exposure. Coalescence was observed after 40minutes leading to water sliding after 50minutes and eventually the first droplet dripped down on the balance scale at approximately 60 minutes.

Water collection was calculated by weight scale and a comparison is shown in Figure 5.8a. In case of SO surfaces fabricated by Devis et.al., total amount of water collected was 142 mg. For glass surface total amount of water collected was 53mg and only one droplet fell down the surface at 80 minutes and remaining droplets started puddling on the bottom edge of the substrate. For PTFE, total water collected was 62.3 mg but it took 102 minutes to collect the only droplet as hydrophobic surfaces take much longer time for condensation. Water collection for PECA coatings was significantly much higher as PECA [100:0], PECA [70:30] and PECA [50:50] collected 138 mg, 146 mg and 156.8 mg of

water respectively in total time span of 120 minutes with three droplets accounted on the balance for each coating. Efficiency of PECA [50:50] coatings is comparatively higher than other cyanoacrylate coatings. Reason is attributed to reduction in surface tension after introduction of benzyl alcohol in cyanoacrylate coatings [163] allowing water droplets to coalescence faster than pristine PECA coatings.

In general, the liquid water on superhydrophilic surfaces flows down vertically due to gravitational force but pins at the bottom edge of the substrate and forms a liquid puddle. Similar trend was observed on glass substrates and elaboration of liquid puddling is exemplified in Figure 5.8b. Whereas there was no such trend observed in case of PECA coatings as contact angle hysteresis was minimal and water droplet started sliding and eventually dropped off the substrate. Figure 5.8b elaborates the droplet puddling and sliding mechanism on the bottom edge of substrate while changings are explained with reference to time.
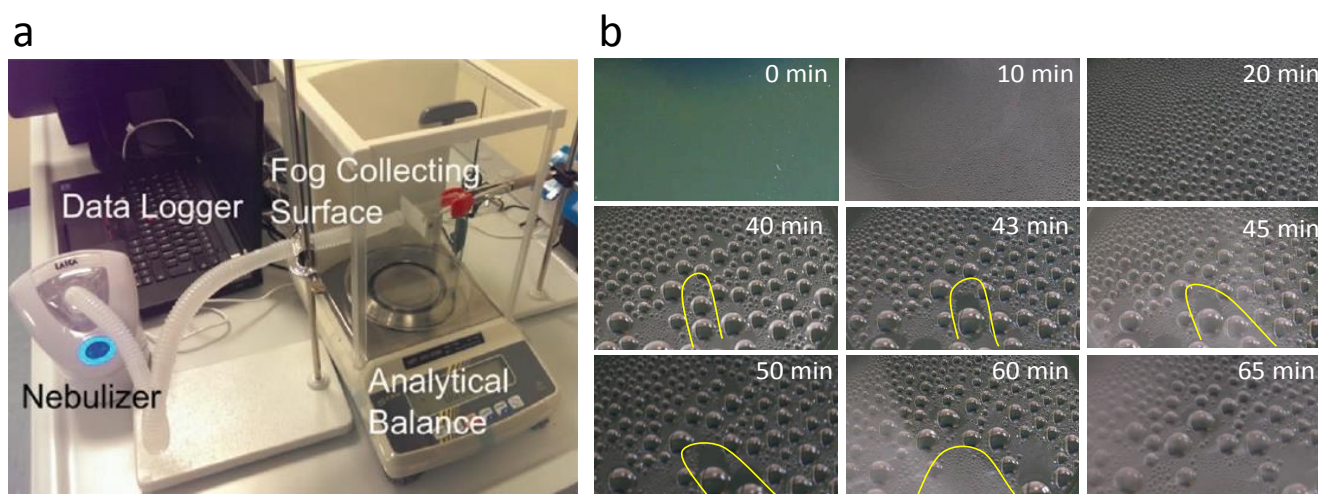
Figure 5.7. a) Photograph of the water collection setup b) Images of PECA surface showing the patterns of water coallescence

Furthermore, contact angle hysteresis and surface tension experiments were performed to validate the acquired results of fog harvesting and are discussed in Figure 5.8c. There are many factors influencing the contact angle hysteresis including surface roughness, chemical heterogeneities, surface deformation, liquid adsorption/desorption, molecular rearrangements etc.[164]. PECA is already reported for its self-cleaning property with low contact angle hysteresis $(\Delta\Theta)$[143] where contact angle hysteresis $\Delta\Theta$ was calculated approximately 24°. Please note that this contact angle hysteresis was measured on a surface of electro-spun fibers which is structurally different from our fabricated surfaces. As a consequence contact angle hysteresis is reduced to ca. 18° for PECA [100:0] whereas it further reduced

to ca. 14° for PECA [50:50]. Surface tension of cyanoacrylate coatings was estimated by different liquids (diiodomethane, diethylene glycerol, dimethylsulfoxide (DMSO), ethylene glycerol, formamide) and mixtures of water and ethanol. The interpreted solid surface energy of PECA [100:0] coatings is calculated as 33.17 mN/m whereas for PECA [50:50] it reduced to 29.5 mN/m. Water contact angle for the PECA coatings was calculated around 72°. Reduction in surface tension induces a critical role in minimizing the resisting force due to hysteresis, as can be calculated by given formula,

$$f_p = w\sigma\,(cos\Theta_R - cos\Theta_A) \qquad\qquad {}^{165}$$

In this equation, w is the width of the droplet and σ is the surface tension, Θ_R is the receding contact angle and Θ_A is the advancing contact angle.
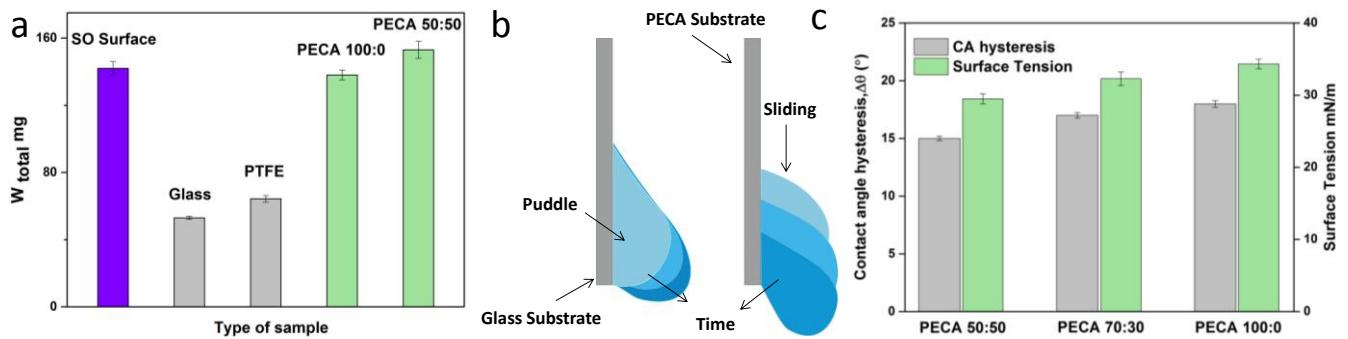
Figure 5.8. a) Comulative mass of water collected after 120 minutes for different surfaces b) Phenomenon of water puddling and water sliding c) Plots of contact angle hysteresis and surface tension of PECA coatings with benzyl alcohol concentrations.

5.4.2 Self-assembly of GNPs on steel substrates

Graphene is well known for performing as a solid lubricant where reduction in friction and minimal material damage is required[166]. There are different methods commonly used to deposit large area graphene polymer coatings for tribological studies in macroscale contact, including chemical vapor deposition (CVD), physical vapor deposition (PVD) etc., to name a few[103]. Although these techniques of graphene deposition are producing low friction coatings, high cost and difficult preparation process hurdle practical applications. One of the possible method to uniformly deposit graphene on macroscale is self-assembly of nanoplatelets either by covalent bonding of graphene with substrates[167], by Marangoni effect[168] or by introducing a polymer matrix in solution processing, behaving as an adhesive agent between graphene nanoplatelets and substrate.

PECA as a solid lubricant was previously investigated[143] and results show that it can be used as a solid lubricant. Although very small friction coefficient was reported, short chain polymers are

usually bad for sliding contacts, which can intrude high wear rate of such materials. Herein, a method is proposed where monomers of ethyl 2-cyanoacrylate (ECA) are drop casted along with GNPs. ECA is known for its anionic polymerization which can rapidly start its polymerization with the help of weak basis and moister in air. As PECA is a short chain polymer which allowed GNPs to assemble itself on top of the substrates. A schematic is presented in Figure 5.9 (a-d) for explaining the mechanism. Figure 5.9(a, b) representing self-assembly of platelets on the steel substrates that were placed in glass petri-dish prior to depositing the material. After one day of solvent evaporation (Figure 5.9c), glass petri-dish was heat treated at 140°C for five hour to completely evaporate the cyclopentanone solvent and reformation of PECA that was used for improvement in the boding strength between graphene platelets and steel substrates. Degradation temperature for PECA is approximately 155°C which is marginally closed to the heat-treated temperature, so we can presume that melting occurred on the surface. After five hours of heat treatment, a very uniform surface was obtained (Figure 5.9d). It has been reported that cyanoacrylate polymers undergo an unzipping process where polymer chain ends deprotonates, resulting in rapid DE polymerization of the polymer backbone, followed by rapid re-polymerization of liberated monomers resulting in daughter polymer backbones of much lower molecular weight[169]. Similar phenomenon is expected to happen in our experimented protocol as excessive heat stimulates the unzipping process in PECA.

μRaman was performed to analyze the spectra of PECA/GNPs coatings with emphasis on 0.2 wt.% GNPs (best obtained percentage for tribological results), shown in Figure 5.9e. According to the Raman spectra, stacking of graphene nanoplatelets resulted in multilayer graphene platelets. Graphene fingerprint peaks are present at 1345 cm^{-1} (D peak), 1585 cm^{-1} (G peak) and 2701 cm^{-1} (2D peak). Inset on 2D peak showing the D1, D2 peaks on the valley. SEM image (inset of Figure 5.9e) showing the segregated GNPs on the surface. Furthermore, in order to investigate the sliding induced disorder and bonding state of C-network, Raman spectroscopy was employed to examine the effects after the friction and wear test. The sliding process resulted in an increase of D-peak intensity (line 2, ID/IG=0.812 compared to ID/IG =0.22 of the initial coated surface), Figure 5.9f, suggesting that the surface became defective and disordered after linear scratch test with 5N applied load and 300 cycles. To understand the mechanism of defects produced by induced force, applied load was increased to 10N. Raman spectra signal was weak and the D peak intensity also increased (line 3, ID/IG =2.704), indicating the surface was badly worn out but still some graphene platelets left in the wear track. Despite the high load of 10N, the friction coefficient was still less than 0.2, after complete wear cycles.
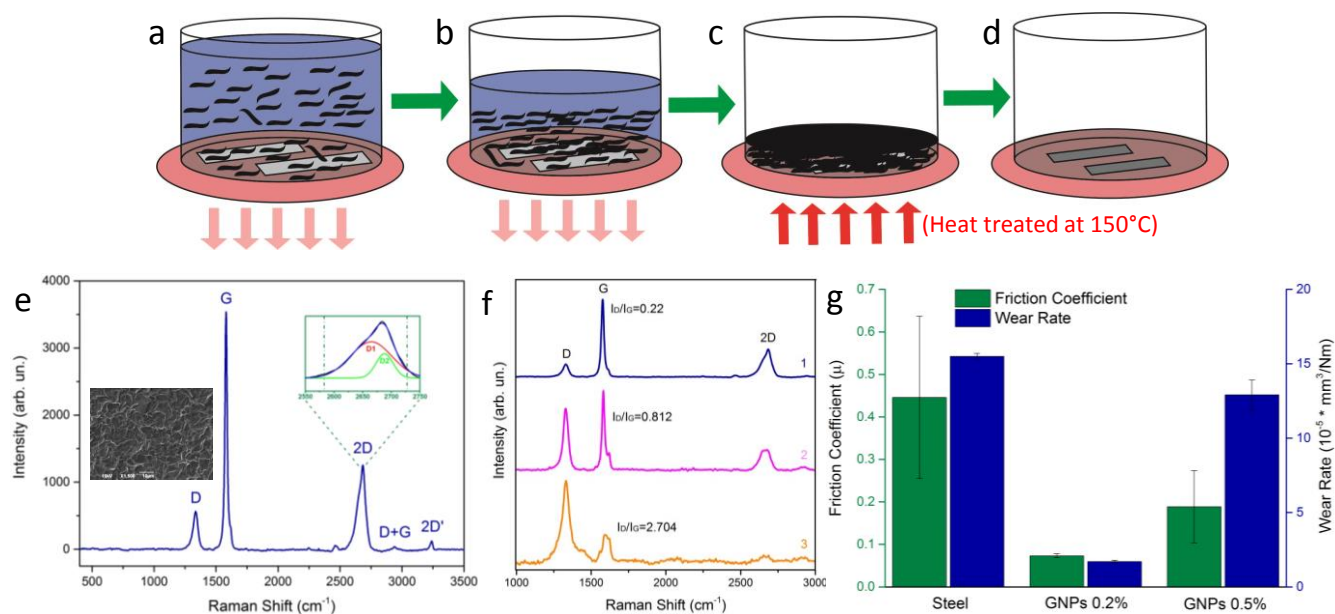
Figure 3.9. (a-d) Mechanism of self-assembly of GNPs on steel substrates (e) μRaman studies of GNPs with 0.2% addition (f) Raman spectra of corresponding areas on steel substrate and (f) tribology results of steel substrate and GNPs fillers with variant concentrations.

Tribological measurements were performed by varying different concentrations of GNPs in accordance with ECA monomers from 0.1-0.5%. The friction coefficient and wear rate of the materials as a function of GNPs and steel are presented in Figure 5.9g. It can be observed that the steel substrate has a coefficient of friction of ca. 0.445 after 300 cycles, whereas after self-assembling GNPs in PECA matrix, a significant reduction in friction was observed specifically for 0.2 wt.% GNPs matrix to ca. 0.0732. Further increase in GNPs concentration from 0.2% to 0.5% resulted in increase of friction up to ca. 0.188, which can be mainly due to agglomeration of graphene platelets. A similar behavior can be seen in the wear rate measurements: the addition of the GNPs resulted in improvement of the wear resistance, which exhibits a minimum at 0.2% GNPs concentration. As shown in Figure 5.9(g), the wear rate for steel substrate is 15.5×10^{-5} mm^3/Nm, which is reduced down to 1.7×10^{-5} mm^3/Nm after 0.2% addition of GNPs in PECA matrix. It is worth noting that it was not possible to measure wear rate of pristine PECA as it could not withstand the complete number of cycles for wear rate measurements.

Furthermore, to investigate the surface morphology of PECA/GNPs coatings, scanning electron microscopy (SEM) was employed and SEM images are presented. Figure 5.10 (a, b) show the surface morphology of PECA with segregation of GNPs at 0.2% and 0.5%. Figure 5.10 (c) represents the SEM

images of the scratched surface of GNPs 0.2% with fairly smooth surface, which suggests the adiabatic formation of a transfer film. Whereas specimen containing 0.5% GNPs exhibited poor wear resistance, transversal cracks and debris are visible on the surface. Transversal cracks are attributed to decohesion at the PECA/GNPs interface, which is very usual in composites based on layered nanofillers[116] and leads to formation of debris in our case. Figure 5.10 (e) show the surface morphology of steel after cyclic load, wear debris are evident on complete wear track.
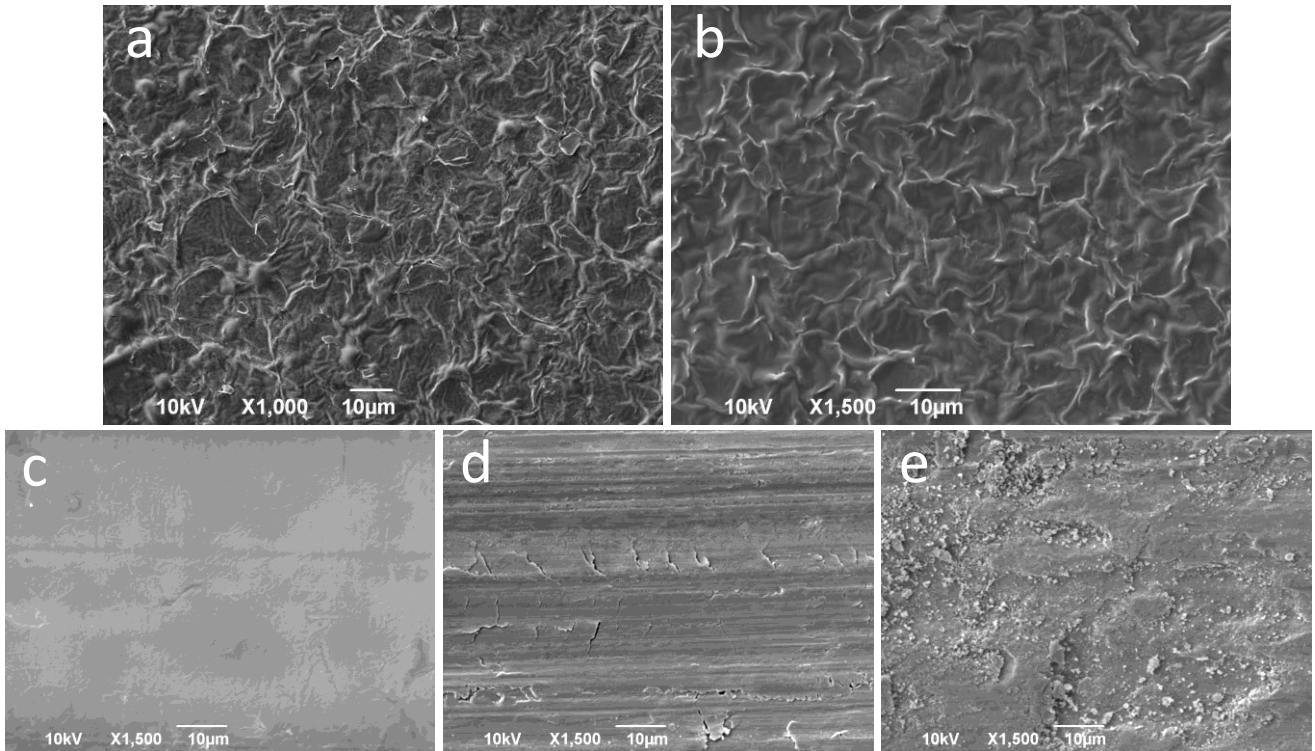
Figure 5.10. SEM images of (a) PECA with 0.2wt.% GNPs (b) PECA with 0.5 wt.% GNPs (c) surface morphology of 0.2wt.% GNPs after 300 wear cycles (d) wear track image with 0.5wt.% GNPs after 300 cycles, transversal cracks are visible (e) Wear track on steel substrate, wear debris are clearly visible.

5.5 Conclusions

We report a simple inexpensive method of fabricating highly transparent poly ethyl 2-cyanoacrylate (PECA) coatings. The process is a single-step solution casting from a common solvent, cyclopentanone, of ethyl cyanoacrylate monomers. The prepared coatings and free standing films demonstrate remarkable transparency (higher than 92%) with first report to achieve it. By taking advantage of its low contact angle hysteresis, developed material is proposed for the fog harvesting application and significant results are achieved. Furthermore, tribological properties of steel are

improved by decreasing the friction more than 6 times and wear rate was improved more than 9 folds by self-assembling graphene nanoplatelets in ECA solution.

6. Closing Remarks

6.1 Thesis Summary

The goal of this thesis is to uncover the mechanism of surface engineering of polymer composites, which is known since the end of 20th century. Despite of the decades of research in this area in the past, it is still challenging to fabricate polymeric coatings with enhanced wear resistance and improved adhesion strength. However, significant advances in understanding these mechanisms at nano-regime have gotten us closer to full understanding. In this thesis we have tackled the problems of durability of both short and long chain polymeric coatings by first developing an understanding of thermodynamics, surface chemistry and transfer film formation and then connecting that to macroscopic behavior. In essence, the framework of the proposed models, based on relevant physics, surface chemistry and size scales of nanofillers, is verified via appropriate experiments.

- At the nanoscale level, we developed a framework to enhance the wear abrasion of water-repellent styrene-based polymer by incorporating silica nanoparticles and by explaining the mechanism of inducing thermodynamic effect on the structures by heat treatment. Significance of rubber domains in polymer matrix is manifested for releasing the mechanical energy dissipation. Furthermore, the role of primer layer is justified for enhancement in adhesion of polymeric coatings, resulting in the improvement of wear-abrasion resistance. These phenomenon's give us the ability to predict how rubbery domains in polymer matrix, and the addition of a primer layer would affect interfacial properties of superhydrophobic surfaces, as a function of abrasion cycles.

- In engineered thermoplastics, which are highly desirable in industrial applications, improvement in tribology and adhesion strength imparts a significant interest. While dealing with metallic counterparts these thermoplastics can be detrimental, because they introduce wear debris on the surface when scratched, that can lead to fracture and fatigue, ultimately deteriorating the coatings. But, with lubricating nanofillers we could begin to dissect the material damage. We examined the friction and wear, working upon previous literature of different nanofillers including aluminum oxide nanoparticles, PTFE microparticles, graphene nanoplatelets. We recognized the effectiveness of using graphene nanoplatelets in polymer matrix owing to its significant mechanical strength, its 2D structure (ideal for solid lubricants),

increased surface energy (for better adhesion with substrates) and its film formation with counterparts, helping to reduce the friction and wear rate for a long number of cycles.

- Recognizing the significance of water based perfluorinated acrylic copolymers in industrial usage as a penetrating sealant for porous surfaces, as a surfactant and for owing the properties of water and oil repellency, we discovered that improvement in tribology of such materials is possible by inducing the pH modulation in the polymer content. Applied potential can modify the surface properties in terms of its adhesion strength towards rubber, aluminum and steel counter-materials. The achieved results gives us insight that by modifying the surface chemistry, it is possible to tune the tribological properties of short-chain polymers.

- At the end, a framework is proposed for controlling the polymerization of cyanoacrylate polymers where a novel strategy is adopted by using non-polar dry solvent to control the polymerization. The effect of benzyl alcohol as an additive is studied, as a way to improve its brittleness and introducing the flexibility by retaining its ultra-transparency. Applications are proposed, experiments are performed for the proposed ideas and it is proved that cyanoacrylate could be an ideal matrix for assembling graphene platelets on any substrates for its short chains, allowing graphene to deposit on the substrate, exploiting the strong adhesion of cyanoacrylate, as it is used commercially as a super glue. Another application is proposed that fabricated coatings could be a potential material for fog harvesting for owning very smooth surfaces with relatively low surface tension, low contact angle hysteresis and its hydrophilic nature for better condensation of tiny water droplets harvested from dense fog.

6.2 Future work

While many future directions could be taken from this work, we will discuss four in particular that would be valuable for surface engineering science and industry. First, our observation about heat-treatment of polymer nanocomposites especially for superhydrophobic surfaces where overcoming the wear abrasion is a major concern. Migration of nanoparticles towards the surface after thermodynamically rearranging the polymer chains could be of significant interest for the applications where surface roughness should be maintained against wear abrasion cycles. Such treatment can influence the surface mechanics, hence improving the overall performance of system. It will be interesting to replace nanoparticles with silica and to see the annealing effect on the migration of nanoparticles that how they behave in the polymer matrix. In addition, introduction of rubbery domains

in polymer matrix can result in improvement for mechanical energy dissipation. Another factor that can be crucially important is better adhesion with the substrate and primer layer can critically enhance the wear abrasion. These polymeric primer layers can melt with dissimilar polymers containing different glass transmission temperatures.

Second, the choice of fillers can play a role for improvement in the tribological properties of engineered polymers. Specifically for the solid lubricants, nanofillers that can create transfer film on counterpart material can drastically impact on performance on friction and wear. Such formation of transfer films can help to sustain the friction coefficient in a stable regime and helps to avoid material removal.

Third, utilizing the surface chemistry of water based perfluorinated acrylics, it is possible to change the adhesion strength, friction and wear as proved in chapter 4. It will be interesting to add electron accepting nanoparticles like Al_2O_3, TiO_2 nanoparticles in perfluorinated acrylic copolymer matrix to observe the behavior of metal carboxylates that tends to adhere with metal counterparts, creating a transfer film as is previously studied with polytetrafluoroethylene polymers. A combination of both mechanisms, modulation of pH and addition of aluminum oxide nanoparticles, could lead to an improvement with advantages of ease of applications and low impact of capstone for owing its environmental friendly nature. In the best case scenario, wear rate could be further reduced.

Finally, as cyanoacrylate is a biocompatible and biodegradable polymer. It will be interesting to find its perspective in medical instruments for the protection purposes. In some medical devices, blood tends to stick on the medical instruments; fabricated transparent coatings (explained in chapter 5) could be a solution for medical devices to prevent from blood clotting. Further, a detailed study of long-term performance and robustness of cyanoacrylate polymers could be of particular interest especially under harsh conditions for example, humid environment, large applied tangential forces etc.

Appendix

Publications

- Masood, M. T., Papadopoulou, L, Evie., Heredia-Guerrero, J. A., Palazon, F., Bayer, I. S., Athanassiou, A., & Ceseracciu, L. (2017). Graphene and polytetrafluoroethylene synergistically improve the tribological properties and adhesion of nylon 66 coatings. *Carbon, (122).*

- Masood, M. T., Heredia-Guerrero, J. A., Ceseracciu, L., Palazon, F., Athanassiou, A., & Bayer, I. S. (2017). Superhydrophobic High Impact Polystyrene (HIPS) Nanocomposites with Wear Abrasion Resistance. *Chemical Engineering Journal*.

- Radaelli, G., Heredia-Guerrero, J. A., Masood, M. T., Ceseracciu, L., Davis, A., Carzino, R., ... & Athanassiou, A. (2016). Highly Effective Antiadhesive Coatings from pH-Modified Water-Dispersed Perfluorinated Acrylic Copolymers: The Case of Vulcanizing Rubber. *Advanced Materials Interfaces*, *3*(13).

- Masood, M. T., Ceseracciu, L., Athanassiou, A., & Bayer, I. S. (2017) Environmentally benign ultra-transparent PECA coatings for multipurpose applications. (In communication)

Conferences Contribution

- Masood, M. T., Radaelli, G., Heredia-Guerrero, J., Bayer, I. S., Athanassiou, A., Ceseracciu, L., "Tuning tribological properties of perflourinated acrylic co-polymer coatings by pH control" EAMC 2016, Stockholm Sweden (Oral Presentation)

- Masood, M. T., Papadopolou, E, L., Heredia-Guerrero, J., Bayer, I. S., Athanassiou, A., Ceseracciu, L., "Enhancement in the tribological response of non-porous nylon 66-based nanocomposites" TriboUK 2017, Imperial College London (Oral Presentation)

- Masood, M. T., Heredia-Guerrero, J., Ceseracciu, L., Athanassiou, A., Bayer, I. S., "Analysis of wear abrasion resistance of multilayer recycled high impact polystyrene (HIPS) nanocomposites" SMT 31, Mons Belgium (Oral Presentation)

Bibliography

1.   Baekeland, L. H. Original papers: The synthesis, constitution, and uses of bakelite. *Ind. Eng. Chem.* **1,** 149–161 (1909).

2.   Chang, I. Y. & Lees, J. K. Recent Development in Thermoplastic Composites: A Review of Matrix Systems and Processing Methods. *J. Thermoplast. Compos. Mater.* **1,** 277–296 (1988).

3.   Fillers, F. *Also of Interest : Macromolecules Polymer Dispersions and Their Industrial Applications An Introduction to Plastics Handbook of Polymer Reaction Engineering Supercritical Carbon Dioxide in Polymer Engineering*. (2005).

4.   Kojima, Y. *et al.* One-pot synthesis of nylon 6–clay hybrid. *J. Polym. Sci. Part A Polym. Chem.* **31,** 1755–1758 (1993).

5.   Marquis, D. M., Guillaume, É. & Chivas-joly, C. Properties of Nano fi llers in Polymer. *Nanocomposites Polym. with Anal. Methods* 261 (2005). doi:10.5772/21694

6.   Ma, M. & Hill, R. M. Superhydrophobic surfaces. *Curr. Opin. Colloid Interface Sci.* **11,** 193–202 (2006).

7.   Barthlott, W. & Neinhuis, C. Purity of the sacred lotus, or escape from contamination in biological surfaces. *Planta* **202,** 1–8 (1997).

8.   Ensikat, H. J., Ditsche-Kuru, P., Neinhuis, C. & Barthlott, W. Superhydrophobicity in perfection: The outstanding properties of the lotus leaf. *Beilstein J. Nanotechnol.* **2,** 152–161 (2011).

9.   Tian, X., Verho, T. & Ras, R. H. A. Moving superhydrophobic surfaces toward real-world applications. *Science (80-.).* **352,** 142–143 (2016).

10.   Dasari, A., Yu, Z. Z. & Mai, Y. W. Fundamental aspects and recent progress on wear/scratch damage in polymer nanocomposites. *Mater. Sci. Eng. R Reports* **63,** 31–80 (2009).

11.   Autumn, K. Mechanisms of Adhesion in Geckos. *Integr. Comp. Biol.* **42,** 1081–1090 (2002).

12.   Eadie, L. & Ghosh, T. K. Biomimicry in textiles: past, present and potential. An overview. *J. R. Soc. Interface* **8,** 761–775 (2011).

13. Hallensleben, M. L. & Chemie, H. Polystyrene and Styrene Copolymers. *Ullmann's Encycl. Ind. Chem.* **29,** 6.5-621 (2012).

14. Brostow, W. & Lobland, H. E. H. Predicting Wear From Mechanical Properties of Thermoplastic Polymers. 1–4 (2008). doi:10.1002/pen

15. Vilaplana, F., Karlsson, S. & Ribes-Greus, A. Changes in the microstructure and morphology of high-impact polystyrene subjected to multiple processing and thermo-oxidative degradation. *Eur. Polym. J.* **43,** 4371–4381 (2007).

16. Katančić, Z., Travaš-Sejdić, J. & Hrnjak-Murgić, Z. Study of flammability and thermal properties of high-impact polystyrene nanocomposites. *Polym. Degrad. Stab.* **96,** 2104–2111 (2011).

17. Vilaplana, F., Ribes-Greus, A. & Karlsson, S. Degradation of recycled high-impact polystyrene. Simulation by reprocessing and thermo-oxidation. *Polym. Degrad. Stab.* **91,** 2163–2170 (2006).

18. Braun, U. & Schartel, B. Flame retardant mechanisms of red phosphorus and magnesium hydroxide in high impact polystyrene. *Macromol. Chem. Phys.* **205,** 2185–2196 (2004).

19. Wang, R. & Meyer, C. Performance of cement mortar made with recycled high impact polystyrene. *Cem. Concr. Compos.* **34,** 975–981 (2012).

20. Zhang, J., Wang, X., Lu, L., Li, D. & Yang, X. Preparation and Performance of High-Impact Polystyrene (HIPS)/ Nano-TiO 2 Nanocomposites. *J. Appl. Polym. Sci.* **87,** 381–385 (2002).

21. Qing, Y. *et al.* Facile approach in fabricating superhydrophobic ZnO/polystyrene nanocomposite coating. *Appl. Surf. Sci.* **285,** 583–587 (2013).

22. Zhu, Y. *et al.* Stable, superhydrophobic, and conductive polyaniline/polystyrene films for corrosive environments. *Adv. Funct. Mater.* **16,** 568–574 (2006).

23. Xue, C.-H., Zhang, Z.-D., Zhang, J. & Jia, S.-T. Lasting and self-healing superhydrophobic surfaces by coating of polystyrene/SiO 2 nanoparticles and polydimethylsiloxane. *J. Mater. Chem. A* **2,** 15001 (2014).

24. Callies, M. & Quéré, D. On water repellency. *Soft Matter* **1,** 55–61 (2005).

25.   Fürstner, R., Barthlott, W., Neinhuis, C. & Walzel, P. Wetting and self-cleaning properties of artificial superhydrophobic surfaces. *Langmuir* **21,** 956–961 (2005).

26.   Cao, L., Jones, A. K., Sikka, V. K., Wu, J. & Gao, D. Anti-Icing superhydrophobic coatings. *Langmuir* **25,** 12444–12448 (2009).

27.   Zhang, H., Lamb, R. & Lewis, J. Engineering nanoscale roughness on hydrophobic surface - Preliminary assessment of fouling behaviour. *Sci. Technol. Adv. Mater.* **6,** 236–239 (2005).

28.   Mohamed, A. M. A., Abdullah, A. M. & Younan, N. A. Corrosion behavior of superhydrophobic surfaces: A review. *Arab. J. Chem.* **8,** 749–765 (2015).

29.   Wang, W. *et al.* Superhydrophobic Coatings with Edible Materials. *ACS Appl. Mater. Interfaces* acsami.6b06958 (2016). doi:10.1021/acsami.6b06958

30.   Xu, Q. F., Mondal, B. & Lyons, A. M. Fabricating superhydrophobic polymer surfaces with excellent abrasion resistance by a simple lamination templating method. *ACS Appl. Mater. Interfaces* **3,** 3508–3514 (2011).

31.   Milionis, A., Languasco, J., Loth, E. & Bayer, I. S. Analysis of wear abrasion resistance of superhydrophobic acrylonitrile butadiene styrene rubber (ABS) nanocomposites. *Chem. Eng. J.* **281,** 730–738 (2015).

32.   Wong, W. S. Y., Stachurski, Z. H., Nisbet, D. R. & Tricoli, A. Ultra-Durable and Transparent Self-Cleaning Surfaces by Large-Scale Self-Assembly of Hierarchical Interpenetrated Polymer Networks. *ACS Appl. Mater. Interfaces* **8,** 13615–13623 (2016).

33.   Russell, M. H., Berti, W. R., Szostek, B. & Buck, R. C. Investigation of the biodegradation potential of a fluoroacrylate polymer product in aerobic soils. *Environ. Sci. Technol.* **42,** 800–807 (2008).

34.   Radaelli, G. *et al.* Highly Effective Antiadhesive Coatings from pH-Modified Water-Dispersed Perfluorinated Acrylic Copolymers: The Case of Vulcanizing Rubber. *Adv. Mater. Interfaces* **3,** 1600069 (2016).

35.   Bayer, I. S., Davis, A. J. & Biswas, A. Robust superhydrophobic surfaces from small diffusion flame treatment of hydrophobic polymers. *RSC Adv.* **4,** 264–268 (2014).

36. Davis, A., Mele, E., Heredia-Guerrero, J. A., Bayer, I. S. & Athanassiou, A. Omniphobic nanocomposite fiber mats with peel-away self similarity. *J. Mater. Chem. A* **3,** 23821–23828 (2015).

37. Zahid, M., Heredia-Guerrero, J. A., Athanassiou, A. & Bayer, I. S. Robust water repellent treatment for woven cotton fabrics with eco-friendly polymers. *Chem. Eng. J.* **319,** 321–332 (2017).

38. Sastri, V. R. *Plastics in Medicals Devices: Properties, Requirements and Aplications*. (2013).

39. Zhang, Y., Ge, D. & Yang, S. Spray-coating of superhydrophobic aluminum alloys with enhanced mechanical robustness. *J. Colloid Interface Sci.* **423,** 101–107 (2014).

40. Chen, K., Zhou, S. & Wu, L. Facile Fabrication of Self-repairing Superhydrophobic Coatings. *Chem. Commun.* **50,** (2014).

41. Liu, Y. *et al.* One-step modification of fabrics with bioinspired polydopamine@octadecylamine nanocapsules for robust and healable self-cleaning performance. *Small* **11,** 426–431 (2015).

42. Zhang, S. *et al.* Deformation and toughening mechanism for high impact polystyrene (HIPS) by pressure-induced-flow processing. *RSC Adv.* **3,** 6879 (2013).

43. Wu, S. A generalized criterion for rubber toughening: The critical matrix ligament thickness. *J. Appl. Polym. Sci.* **35,** 549–561 (1988).

44. Milionis, A., Loth, E. & Bayer, I. S. Recent advances in the mechanical durability of superhydrophobic materials. *Adv. Colloid Interface Sci.* **229,** 57–79 (2016).

45. Nikfarjam, N., Taheri Qazvini, N. & Deng, Y. Cross-linked starch nanoparticles stabilized Pickering emulsion polymerization of styrene in w/o/w system. *Colloid Polym. Sci.* **292,** 599–612 (2014).

46. Yang, J. *et al.* Synthesis and foaming of water expandable polystyrene-activated carbon (WEPSAC). *Polymer (Guildf).* **50,** 3169–3173 (2009).

47. Han, X., Zeng, C., Lee, L. J., Koelling, K. W. & Tomasko, D. L. Extrusion of polystyrene nanocomposite foams with supercritical CO2. *Polym. Eng. Sci.* **43,** 1261–1275 (2003).

48. Wool, R. P., Yuan, B. -L & McGarel, O. J. Welding of polymer interfaces. *Polym. Eng. Sci.* **29,** 1340–1367 (1989).

49. Schnell, R., Stamm, M. & Creton, C. Direct Correlation between Interfacial Width and Adhesion in Glassy Polymers. *Macromolecules* **31,** 2284–2292 (1998).

50. Ge, T., Grest, G. S. & Robbins, M. O. Tensile fracture of welded polymer interfaces: Miscibility, entanglements, and crazing. *Macromolecules* **47,** 6982–6989 (2014).

51. Amado, F. D. R., Gondran, E., Ferreira, J. Z., Rodrigues, M. A. S. & Ferreira, C. A. Synthesis and characterisation of high impact polystyrene/polyaniline composite membranes for electrodialysis. *J. Memb. Sci.* **234,** 139–145 (2004).

52. Yuan, B. & Wool, R. Strength development at incompatible semicrystalline polymer interfaces. *Polym. Eng. Sci.* **30,** 1454–1464 (1990).

53. McEvoy, R. L. & Krause, S. Interfacial interactions bertween polyethylene and polypropylene and some ethylene-containing copolymers. *Macromolecules* **29,** 4258–4266 (1996).

54. Burris, D. L., Boesl, B., Bourne, G. R. & Sawyer, W. G. Polymeric nanocomposites for tribological applications. *Macromol. Mater. Eng.* **292,** 387–402 (2007).

55. Rankin, K. & Mabury, S. A. Influence of fluorination on the characterization of fluorotelomer-based acrylate polymers by matrix-assisted laser desorption/ionization time-of-flight mass spectrometry. *Anal. Chim. Acta* **808,** 115–123 (2014).

56. Zhao, N. *et al.* Superhydrophobic surface from vapor-induced phase separation of copolymer micellar solution. *Macromolecules* **38,** 8996–8999 (2005).

57. Steward, P. A., Hearn, J. & Wilkinson, M. C. An overview of polymer latex film formation and properties. 195–267 (2000).

58. Bhutto, A. A., Vesely, D. & Gabrys, B. J. Miscibility and interactions in polystyrene and sodium sulfonated polystyrene with poly(vinyl methyl ether) PVME blends. Part II. FTIR. *Polymer (Guildf).* **44,** 6627–6631 (2003).

59. Rieger, J. The glass transition temperature of polystyrene. *J. Therm. Anal.* **46,** 965–972 (1996).

60.   Gupta, S., Zhang, Q., Emrick, T., Balazs, A. C. & Russell, T. P. Entropy-driven segregation of nanoparticles to cracks in multilayered composite polymer structures. *Nat. Mater.* **5,** 229–233 (2006).

61.   Milionis, A., Dang, K., Prato, M., Loth, E. & Bayer, I. S. Liquid repellent nanocomposites obtained from one-step water-based spray. *J. Mater. Chem. A* **3,** 12880–12889 (2015).

62.   Bayer, I. On the Durability and Wear Resistance of Transparent Superhydrophobic Coatings. *Coatings* **7,** 12 (2017).

63.   Zhi Rong, M. *et al.* Microstructure and tribological behavior of polymeric nanocomposites. *Ind. Lubr. Tribol.* **53,** 72–77 (2001).

64.   Sidorenko, A., Ahn, H. S., Kim, D. I., Yang, H. & Tsukruk, V. V. Wear stability of polymer nanocomposite coatings with trilayer architecture. *Wear* **252,** 946–955 (2002).

65.   Shi, G., Zhang, M. Q., Rong, M. Z., Wetzel, B. & Friedrich, K. Sliding wear behavior of epoxy containing nano-Al2O3 particles with different pretreatments. *Wear* **256,** 1072–1081 (2004).

66.   Friedrich, K., Zhang, Z. & Schlarb, A. K. Effects of various fillers on the sliding wear of polymer composites. *Compos. Sci. Technol.* **65,** 2329–2343 (2005).

67.   Hung, L. L. . & Chen, C. C. . Recent progress of molecular organic electroluminescent materials and devices. *Mater. Sci. Eng. R Reports* **39,** 143–222 (2002).

68.   Rykaczewski, K. *et al.* How nanorough is rough enough to make a surface superhydrophobic during water condensation? *Soft Matter* **8,** 8786 (2012).

69.   Donnet, C. & Erdemir, A. Historical developments and new trends in tribological and solid lubricant coatings. *Surf. Coatings Technol.* **180–181,** 76–84 (2004).

70.   Zhang, G. *et al.* On dry sliding friction and wear behaviour of PEEK and PEEK/SiC-composite coatings. *Wear* **260,** 594–600 (2006).

71.   Arita, M., Yasuda, Y., Kishi, K. & Ohmae, N. Investigations of tribological characteristics of solid lubricants exposed to atomic oxygen. *Tribol. Trans.* **35,** 374–380 (1992).

72.   Nosonovsky, M. & Bhushan, B. Green tribology: principles, research areas and challenges.

Philos. Trans. R. Soc. A Math. Phys. Eng. Sci. **368,** 4677–4694 (2010).

73.   Briscoe, B. J. & Sinha, S. K. Tribological applications of polymers and their composites: Past, present and future prospects. 1–14 (2008). doi:10.1016/S1572-3364(08)55001-4

74.   Villanueva, J. *et al.* Corrosion, Tribology, and Tribocorrosion Research in Biomedical Implants: Progressive Trend in the Published Literature. *J. Bio- Tribo-Corrosion* **3,** 1 (2017).

75.   Ii, S. Friction induced damage: preliminary numerical analysis of stresses within painted automotive plastics induced by large curvature counterfaces. **204,** (1997).

76.   Jung, Y. C. & Bhushan, B. Contact angle, adhesion and friction properties of micro-and nanopatterned polymers for superhydrophobicity. *Nanotechnology* **17,** 4970–4980 (2006).

77.   Nozawa, J. I., Komoto, T., Kawai, T. & Kumehara, H. Tribological properties of polymer-sheet-adhered metal hybrid gear. *Wear* **266,** 893–897 (2009).

78.   Siracusa, V., Rocculi, P., Romani, S. & Rosa, M. D. Biodegradable polymers for food packaging: a review. *Trends Food Sci. Technol.* **19,** 634–643 (2008).

79.   Sonsino, C. M. & Moosbrugger, E. Fatigue design of highly loaded short-glass-fibre reinforced polyamide parts in engine compartments. *Int. J. Fatigue* **30,** 1279–1288 (2008).

80.   Demirci, M. T. & D??zc??ko??lu, H. Wear behaviors of Polytetrafluoroethylene and glass fiber reinforced Polyamide 66 journal bearings. *Mater. Des.* **57,** 560–567 (2014).

81.   Jae, H. L., Lee, S.-G., Choi, K.-Y. & Liu, J. Crystallization and Melting Behaviour of Nylon 66 Poly(Ether Imide) Blends.Pdf. *Polymer journal* **30,** 531–537 (1998).

82.   Apichartpattanasiri, S., Hay, J. N. & Kukureka, S. N. A study of the tribological behaviour of polyamide 66 with varying injection-moulding parameters. *Wear* **251,** 1557–1566 (2001).

83.   Wan, K.-T., Prima, a., Ye, L. & Mai, Y.-W. Adhesion of nylon-6 on surface treated aluminium substrates. *J. Mater. Sci.* **31,** 2109–2116 (1996).

84.   Meguid, S. A. & Sun, Y. On the tensile and shear strength of nano-reinforced composite interfaces. *Mater. Des.* **25,** 289–296 (2004).

85.   Dorigato, A. & Pegoretti, A. The role of alumina nanoparticles in epoxy adhesives. *J.*

Nanoparticle Res. **13,** 2429–2441 (2011).

86. Aderikha, V. N. & Shapovalov, V. A. Effect of filler surface properties on structure, mechanical and tribological behavior of PTFE-carbon black composites. *Wear* **268,** 1455–1464 (2010).

87. Xue, Y., Wu, W., Jacobs, O. & Schädel, B. Tribological behaviour of UHMWPE/HDPE blends reinforced with multi-wall carbon nanotubes. *Polym. Test.* **25,** 221–229 (2006).

88. Sawyer, W. G., Freudenberg, K. D., Bhimaraj, P. & Schadler, L. S. A study on the friction and wear behavior of PTFE filled with alumina nanoparticles. *Wear* **254,** 573–580 (2003).

89. Khare, H. S. & Burris, D. L. The effects of environmental water and oxygen on the temperature-dependent friction of sputtered molybdenum disulfide. *Tribol. Lett.* **52,** 485–493 (2013).

90. Lancaster, J. K. A review of the influence of environmental humidity and water on friction, lubrication and wear. *Tribol. Int.* **23,** 371–389 (1990).

91. Kumar, N., Dash, S., Tyagi, A. K. & Raj, B. Super low to high friction of turbostratic graphite under various atmospheric test conditions. *Tribol. Int.* **44,** 1969–1978 (2011).

92. Cataldi, P., Ceseracciu, L., Marras, S., Athanassiou, A. & Bayer, I. S. Electrical conductivity enhancement in thermoplastic polyurethane-graphene nanoplatelet composites by stretch-release cycles. *Appl. Phys. Lett.* **110,** 3–8 (2017).

93. Eswaraiah, V., Sankaranarayanan, V. & Ramaprabhu, S. Graphene-based engine oil nanofluids for tribological applications. *ACS Appl. Mater. Interfaces* **3,** 4221–4227 (2011).

94. Wei, X. *et al.* Plasticity and ductility in graphene oxide through a mechanochemically induced damage tolerance mechanism. *Nat. Commun.* **6,** 8029 (2015).

95. Zhao, X., Zhang, Q., Chen, D. & Lu, P. Enhanced mechanical properties of graphene-based polyvinyl alcohol composites. *Macromolecules* **43,** 2357–2363 (2010).

96. Lahiri, D. *et al.* Graphene nanoplatelet-induced strengthening of ultrahigh molecular weight polyethylene and biocompatibility in vitro. *ACS Appl. Mater. Interfaces* **4,** 2234–2241 (2012).

97. Xu, Z. & Gao, C. In situ polymerization approach to graphene-reinforced nylon-6 composites. *Macromolecules* **43,** 6716–6723 (2010).

98.   Cataldi, P. *et al.* Effect of graphene nano-platelet morphology on the elastic modulus of soft and hard biopolymers. *Carbon N. Y.* **109,** 331–339 (2016).

99.   He, Y., Chen, W. F., Yu, W. B., Ouyang, G. & Yang, G. W. Anomalous interface adhesion of graphene membranes. *Sci. Rep.* **3,** 2660 (2013).

100.   Koenig, S. P., Boddeti, N. G., Dunn, M. L. & Bunch, J. S. Ultrastrong adhesion of graphene membranes. *Nat. Nanotechnol.* **6,** 543–546 (2011).

101.   Berman, D., Erdemir, A. & Sumant, A. V. Graphene: A new emerging lubricant. *Mater. Today* **17,** 31–42 (2014).

102.   Wei, N., Peng, X. & Xu, Z. Understanding water permeation in graphene oxide membranes. *ACS Appl. Mater. Interfaces* **6,** 5877–5883 (2014).

103.   Kim, K. S. *et al.* Chemical vapor deposition-grown graphene: The thinnest solid lubricant. *ACS Nano* **5,** 5107–5114 (2011).

104.   Huang, Y. *et al.* Wear evolution of monolayer graphene at the macroscale. *Carbon N. Y.* **115,** 600–607 (2017).

105.   Zeng, X., Peng, Y. & Lang, H. A novel approach to decrease friction of graphene. *Carbon N. Y.* **118,** 233–240 (2017).

106.   Ren, G. *et al.* Influence of functional graphene as filler on the tribological behaviors of Nomex fabric/phenolic composite. *Compos. Part A Appl. Sci. Manuf.* **49,** 157–164 (2013).

107.   Lahiri, D. *et al.* Nanotribological behavior of graphene nanoplatelet reinforced ultra high molecular weight polyethylene composites. *Tribol. Int.* **70,** 165–169 (2014).

108.   Kandanur, S. S. *et al.* Suppression of wear in graphene polymer composites. *Carbon N. Y.* **50,** 3178–3183 (2012).

109.   Berman, D., Erdemir, A. & Sumant, A. V. Few layer graphene to reduce wear and friction on sliding steel surfaces. *Carbon N. Y.* **54,** 454–459 (2013).

110.   Poletto, P., Duarte, J., Thürmer, M. B., Santos, V. dos & Zeni, M. Characterization of Polyamide 66 membranes prepared by phase inversion using formic acid and hydrochloric acid such as

solvents. *Mater. Res.* **14,** 547–551 (2011).

111. Tanaka, N. & Fukushima, T. Melting and recrystallization in modified porous nylon-6 membranes. *Thermochim. Acta* **396,** 79–85 (2003).

112. Papadopoulou, E. L. *et al.* Nylon 6,6/graphene nanoplatelet composite films obtained from a new solvent. *RSC Adv.* **6,** 6823–6831 (2016).

113. Cataldi, P. *et al.* Foldable Conductive Cellulose Fiber Networks Modified by Graphene Nanoplatelet-Bio-Based Composites. *Adv. Electron. Mater.* **1,** 1–8 (2015).

114. Murthy, N. S., Curran, S. A., Aharoni, S. M. & Minor, H. Premelting Crystalline Relaxations and Phase Transitions in Nylon 6 and 6,6. *Macromolecules* **24,** 3215–3220 (1991).

115. Lawn, B. R. Indentation of Ceramics with Spheres: A Century after Hertz. *J. Am. Ceram. Soc.* **81,** 1977–1994 (2005).

116. Dasari, A., Yu, Z. Z., Mai, Y. W., Hu, G. H. & Varlet, J. Clay exfoliation and organic modification on wear of nylon 6 nanocomposites processed by different routes. *Compos. Sci. Technol.* **65,** 2314–2328 (2005).

117. Ye, J., Khare, H. S. & Burris, D. L. Transfer film evolution and its role in promoting ultra-low wear of a PTFE nanocomposite. *Wear* **297,** 1095–1102 (2013).

118. Khedkar, J., Negulescu, I. & Meletis, E. I. Sliding wear behavior of PTFE composites. *Wear* **252,** 361–369 (2002).

119. Xiang, D. & Gu, C. A study on the friction and wear behavior of PTFE filled with ultra-fine kaolin particulates. *Mater. Lett.* **60,** 689–692 (2006).

120. Harris, K. L. *et al.* PTFE Tribology and the Role of Mechanochemistry in the Development of Protective Surface Films. *Macromolecules* **48,** 3739–3745 (2015).

121. Jiang, T. & Zhu, Y. Measuring graphene adhesion using atomic force microscopy with a microsphere tip. *Nanoscale* **7,** 10760–10766 (2015).

122. Cai, M., Guo, R., Zhou, F. & Liu, W. Lubricating a bright future: Lubrication contribution to energy saving and low carbon emission. *Sci. China Technol. Sci.* **56,** 2888–2913 (2013).

123. Miyoshi, K. Solid Lubricants and Coatings for Extreme Environments: State-of-the-Art Survey. 1–23 (2007). doi:20070010580

124. Park, I. J., Lee, S. -B & Choi, C. K. Surface properties for poly(perfluoroalkylethyl methacrylate)/poly(n-alkyl methacrylate)s mixtures. *J. Appl. Polym. Sci.* **54,** 1449–1454 (1994).

125. Mclain, S. J., Sauer, B. B. & Firment, L. E. Surface Properties and Metathesis Synthesis of Block Copolymers Including Perfluoroalkyl-Ended Polyethylenes. *Macromolecules* **9297,** 8211–8219 (1996).

126. Hu, P. *et al.* Rigid-flexible coupling high ionic conductivity polymer electrolyte for an enhanced performance of LiMn2O4/graphite battery at elevated temperature. *ACS Appl. Mater. Interfaces* **7,** 4720–4727 (2015).

127. Yao, W., Li, Y. & Huang, X. Fluorinated poly(meth)acrylate: Synthesis and properties. *Polym. (United Kingdom)* **55,** 6197–6211 (2014).

128. Davis, A., Yeong, Y. H., Steele, A., Bayer, I. S. & Loth, E. Superhydrophobic nanocomposite surface topography and ice adhesion. *ACS Appl. Mater. Interfaces* **6,** 9272–9279 (2014).

129. Schutzius, T. M., Bayer, I. S., Tiwari, M. K. & Megaridis, C. M. Novel fluoropolymer blends for the fabrication of sprayable multifunctional superhydrophobic nanostructured composites. *Ind. Eng. Chem. Res.* **50,** 11117–11123 (2011).

130. Volokitin, A. I. & Persson, B. N. J. Van Der Waals' Friction. (1989).

131. Ratoia, M., Bovington, C. & Spikes, H. In situ study of metal oleate friction modifier additives. *Tribol. Lett.* **14,** 33–40 (2003).

132. Murase, A. & Ohmori, T. ToF-SIMS analysis of model compounds of friction modifier adsorbed onto friction surfaces of ferrous materials. *Surf. Interface Anal.* **31,** 191–199 (2001).

133. Melody, D. P. Advances in Room Temperature Curing Adhesives and Sealants-A Review. *Br. Polym. J.* **21,** 175–179 (1989).

134. Vezin, W. R. & Florence, A. T. In vitro heterogeneous degradation of poly(n-alkyl α-cyanoacrylates). *J. Biomed. Mater. Res.* **14,** 93–106 (1980).

135. Tripodo, G., Wischke, C. & Lendlein, A. Highly flexible poly(ethyl-2-cyanoacrylate) based materials obtained by incorporation of oligo(ethylene glycol)diglycidylether. *Macromol. Symp.* **309–310,** 49–58 (2011).

136. Xu, L. *et al.* A cross-linking strategy provides a new generation of biodegradable and biocompatible cyanoacrylate medical adhesives. *J. Mater. Chem. B* **4,** 4147–4155 (2016).

137. Emulsion Polymerization of Ethylene . 11 . Effect of Recipe on. **10,** 1966 (1966).

138. Attanasio, A., Bayer, I. S., Ruffilli, R., Ayadi, F. & Athanassiou, A. Surprising high hydrophobicity of polymer networks from hydrophilic components. *ACS Appl. Mater. Interfaces* **5,** 5717–5726 (2013).

139. Tiwari, M. K., Bayer, I. S., Jursich, G. M., Schutzius, T. M. & Megaridis, C. M. Highly liquid-repellent, large-area, nanostructured poly(vinylidene fluoride)/poly(ethyl 2-cyanoacrylate) composite coatings: Particle filler effects. *ACS Appl. Mater. Interfaces* **2,** 1114–1119 (2010).

140. Yang, J., Lee, H., Hyung, W., Park, S. B. & Haam, S. Magnetic PECA nanoparticles as drug carriers for targeted delivery: Synthesis and release characteristics. *J. Microencapsul.* **23,** 203–212 (2006).

141. Kumari, A., Yadav, S. K. & Yadav, S. C. Biodegradable polymeric nanoparticles based drug delivery systems. *Colloids Surfaces B Biointerfaces* **75,** 1–18 (2010).

142. Cui, Y. *et al.* Facile and Reliable in Situ Polymerization of Poly(Ethyl Cyanoacrylate)-Based Polymer Electrolytes toward Flexible Lithium Batteries. *ACS Appl. Mater. Interfaces* **9,** 8737–8741 (2017).

143. Mele, E. *et al.* Zwitterionic Nanofibers of Super-Glue for Transparent and Biocompatible Multi-Purpose Coatings. *Sci. Rep.* **5,** 14019 (2015).

144. Han, M. G. & Kim, S. Controlled degradation of poly(ethyl cyanoacrylate-co-methyl methacrylate) (PECA-co-PMMA) copolymers. *Polymer (Guildf).* **50,** 1270–1280 (2009).

145. Franc, E. & Pepper, D. C. Solubilities, Viscosities and Unperturbed Dimensions of Poly(ethyl cyanoacrylate)s and Poly(buthyl cyanoacrylate)s. *Makromol. Chem., Rapid Commun* **442,** 439–442 (1981).

146. E. F. Donnelly, D. S. Johnston, D. C. P. Ionic and Zwitterionic Polymerization of n-Alkyl 2-Cyanoacrylate. *Polym. Lett. Ed.* **15,** 399–405 (1977).

147. Prat, D., Hayler, J. & Wells, A. A survey of solvent selection guides. *Green Chem.* **16,** 4546–4551 (2014).

148. Lawrenson, S., North, M., Peigneguy, F. & Routledge, A. Greener solvents for solid-phase synthesis. *Green Chem.* **19,** 952–962 (2017).

149. Tran, T. N. *et al.* Transparent and flexible amorphous cellulose-acrylic hybrids. *Chem. Eng. J.* **287,** 196–204 (2016).

150. Zhang, X., Tang, X. & Bowen, K. Photoelectron spectroscopic study of the ethyl cyanoacrylate anion. *Chem. Phys. Lett.* **582,** 21–23 (2013).

151. Han, M. G., Kim, S. & Liu, S. X. Synthesis and degradation behavior of poly(ethyl cyanoacrylate). *Polym. Degrad. Stab.* **93,** 1243–1251 (2008).

152. Shanmukh, S. & Dluhy, R. A. Kv correlation analysis. A quantitative two-dimensional IR correlation method for analysis of rate processes with exponential functions. *J. Phys. Chem. A* **108,** 5625–5634 (2004).

153. Edwards, H. G. M. & Day, J. S. Fourier transform Raman spectroscopic studies of the curing of cyanoacrylate glue. *J. Raman Spectrosc.* **35,** 555–560 (2004).

154. Mankidy, P. J., Rajagopalan, R. & Foley, H. C. Influence of initiators on the growth of poly(ethyl 2-cyanoacrylate) nanofibers. *Polymer (Guildf).* **49,** 2235–2242 (2008).

155. Tomlinson, S. K., Ghita, O. R., Hooper, R. M. & Evans, K. E. The use of near-infrared spectroscopy for the cure monitoring of an ethyl cyanoacrylate adhesive. *Vib. Spectrosc.* **40,** 133–141 (2006).

156. Ayadi, F. *et al.* Mechanical reinforcement and water repellency induced to cellulose sheets by a polymer treatment. *Cellulose* **20,** 1501–1509 (2013).

157. Kim, S. & Peterson, S. C. Development of degradable polymer composites from starch and poly(ethyl cyanoacrylate). *Polym. Compos.* **33,** 904–911 (2012).

158. Bull, S. J. Failure modes in scratch adhesion testing. *Surf. Coatings Technol.* **50,** 25–32 (1991).

159. Barletta, M., Gisario, A., Puopolo, M. & Vesco, S. Scratch, wear and corrosion resistant organic inorganic hybrid materials for metals protection and barrier. *Mater. Des.* **69,** 130–140 (2015).

160. Lee, A., Moon, M. W., Lim, H., Kim, W. D. & Kim, H. Y. Water harvest via dewing. *Langmuir* **28,** 10183–10191 (2012).

161. Sharma, C. S., Combe, J., Giger, M., Emmerich, T. & Poulikakos, D. Growth Rates and Spontaneous Navigation of Condensate Droplets Through Randomly Structured Textures. *ACS Nano* **11,** 1673–1682 (2017).

162. Davis, A. *et al.* Water Collection by Sticky Microislands on Superomniphobic Electrospun Surfaces. *Adv. Mater. Interfaces* **3,** 1–7 (2016).

163. Goyal, M. K., Roy, I., Amin, A., Banerjee, U. C. & Bansal, A. K. Stabilization of Lysozyme by Benzyl Alcohol : Surface Tension and Thermodynamic Parameters. **99,** 4149–4161 (2010).

164. Eral, H. B., 't Mannetje, D. J. C. M. & Oh, J. M. Contact angle hysteresis: a review of fundamentals and applications. *Colloid Polym. Sci.* **291,** 247–260 (2013).

165. Cox, R. G. The dynamics of the spreading of liquids on a solid surface. Part 2. Surfactants. *J. Fluid Mech.* **168,** 195 (1986).

166. Masood, M. T. *et al.* Graphene and polytetrafluoroethylene synergistically improve the tribological properties and adhesion of nylon 66 coatings. *Carbon N. Y.* **123,** 26–33 (2017).

167. Li, P. F., Zhou, H. & Cheng, X. H. Nano/micro tribological behaviors of a self-assembled graphene oxide nanolayer on Ti/titanium alloy substrates. *Appl. Surf. Sci.* **285,** 937–944 (2013).

168. Wu, P. *et al.* Self-Assembled Graphene Film as Low Friction Solid Lubricant in Macroscale Contact. *ACS Appl. Mater. Interfaces* **9,** 21554–21562 (2017).

169. Burns, B. Polycyanoacrylates. *Encycl. Polym. Sci. Technol.* 1–27 (2016). doi:10.1002/0471440264.pst256.pub2